University of Southampton

SPIN POLARISED DYNAMICS IN QUANTUM WELLS

By

ELAINE BLACKWOOD

A thesis submitted for the degree of
Doctor of Philosophy
at the Department of Physics, the University of Southampton
January 1993

UNIVERSITY OF SOUTHAMPTON

ABSTRACT

FACULTY OF SCIENCE

PHYSICS

Doctor of Philosophy

SPIN POLARISATION DYNAMICS IN QUANTUM WELLS

by Elaine Blackwood

The ability to preferentially spin-polarise a photoexcited carrier population in a quantum well by optical pumping methods has enabled us to study the fine structure and some of the parameters governing the spin relaxation dynamics of excitons, heavy-holes and electrons in a number of type I GaAs/Al$_x$Ga$_{1-x}$As and type I In$_x$Ga$_{1-x}$As/GaAs single and multiple quantum wells.

The electron, hole and excitonic effective Lande g-factors have been measured as a function of quantum well thickness in GaAs/Al$_{0.36}$Ga$_{0.64}$As and In$_{0.11}$Ga$_{0.89}$As/GaAs. For the GaAs/AlGaAs wells, we observed a change in sign of the exciton g-factor and using *k.p* perturbation theory to model the form of the electron g-factor, we obtained the hole g-factor as a function of well width. Both the electron and hole g-factors also exhibited a change in sign. In the case of the InGaAs/GaAs wells, the exciton g-factor was small and of positive magnitude for all the wells we studied. Describing the form of the electron g-factor by a strain modified *k.p* perturbation theory and using the measured exciton g-values, the hole g-factor was calculated to take small, but slightly more positive values than the exciton g-factor.

The electron-hole exchange interactions have been measured in GaAs/Al$_{0.36}$Ga$_{0.64}$As and GaAs/AlAs samples as a function of well width. In both cases the exchange splitting between the optically active and inactive levels was consistent with theory, falling rapidly with decreasing confinement towards the measured value for bulk GaAs. A finite exchange splitting of the optically active levels at zero field demonstrates the symmetry of the quantum well is less than D_{2d}, possibly due to growth induced imperfections.

We have measured the spin relaxation times of electrons, holes and excitons in GaAs/Al$_{0.3}$Ga$_{0.7}$As quantum wells. We observed a much shorter relaxation time for the excitons, 100ps, compared to the free electron and hole relaxation times which were both of the order of 1ns. We have attributed the fast exciton spin relaxation to the strong exchange between the electron and hole forcing the more rapidly relaxing particle to govern the spin relaxation dynamics. Our results suggest that the hole is the more rapidly relaxing particle when confined in an exciton. We have attributed this rapid spin relaxation of the holes to the mixing of the light and heavy-hole bands for wavevectors away from $k=0$ in a quantum wells. We have also observed a strong temperature dependence of the hole relaxation time which is consistent with a wavevector dependence of the hole relaxation time. Finally we have direct measurements of the wavevector dependence of hole relaxation time and the reduction in this due to the mixing of the valence band states in a quantum well away from $k=0$.

Table of Contents

Chapter 1

Introduction

Chapter 2

Experimental Apparatus and Sample Details

Chapter 3

Exciton, Heavy-Hole and Electron g-factors in Type I $GaAs/Al_xGa_{1-x}As$, $In_xGa_{1-x}As/GaAs$ Quantum Wells

Chapter 4

Exchange Interactions in Type I GaAs/$Al_{0.36}Ga_{0.64}As$, GaAs/AlAs and $In_{0.11}Ga_{0.89}As$/GaAs Quantum Wells

page

Chapter 5

Atomic Exciton Spin Relaxation

Chapter 6

Wavevector Dependence of the Hole Spin-Lattice Relaxation Time

page

Chapter 7

Appendix

ACKNOWLEDGMENTS

I would firstly wish to express my sincere thanks to my supervisor Dr.Richard Harley for his excellent supervision and guidance throughout my three years.

My thanks must also go to Dr.Michael.J.Snelling with whom I had the pleasure of working with on portions of the work detailed in chapters 3,4 and 5 and whose preliminary work on the subject of optical orientation in type I systems was invaluable. Conor McDonagh and Richard Worsley, my collaborators at various periods throughout my experimentation, also deserve my thanks.

I am also grateful to Dr.S.R.Andrews of GEC Research, Dr.C.T.B.Foxon of Philips and Prof.L.Eaves of the University of Nottingham for supplying us with samples, to Dr.P.Dawson of UMIST and again to Dr.S.R.Andrews who supplied us with invaluable data and theoretical calculations.

The assistance of all the technical staff at the Department of Physics, especially to Colin Miles (Departmental superintendent and chief technician) and Vince Davey (Store manager) was gratefully appreciated at all times.

I acknowledge the financial support of both the Science and Engineering research council and R.S.R.E, Malvern.

Finally, I cannot thank my family and friends enough for the support and encouragement they showed throughout my years in education, but most especially, I thank my father.

In loving memory of my Father.

1 Introduction

1.1 Preview

Our understanding of electron transport in solids is based on semiclassical Newtonian mechanics in which particles moving in an external field are occasionally scattered by phonons and impurities. This thesis studies some of the consequences of devices with dimensions smaller than 100 nanometres in which motion of the carriers is confined in one or more directions and so Newtonian mechanics no-longer applies. The behaviour of such low-dimensional structures (LDS) shows pronounced "Quantum effects", such as size quantisation and tunnelling.

The first device to be manufactured based on these phenomenon was the tunnel diode in the late 1950s by Leo Esaki. This relied on electron tunnelling through the bandgap of a p-n junction.

The development of molecular-beam epitaxy[1-4] in the late 1960s at AT&T Bell Laboratories paved the way for the growth of structures consisting of atomic layers of different semiconductor materials with thicknesses as narrow as 20Å, grown consecutively, one on top of the other, and with atomically sharp interfaces between each. From these advances came the development of the "vertical" quantum device in which current flow was perpendicular to the layers.

In 1974 two basic but important experiments were performed. The first was by Esaki and Chang who observed oscillatory behaviour of the perpendicular differential conductance due to quantum tunnelling through two potential barriers[5] and the second was by Dingle whose optical measurements[6] showed directly the energy level quantization in thin layers that had to date only been theoretically predicted. These observations were the breakthrough which produced accelerated interest in these quantum devices.

With the progress in both controlled crystal growth and the understanding of the mechanisms governing these systems, we have advanced from the simple p-n junction tunnel diode to a wide variety of structures and devices, all designed as a result of research on quantum effects such as Quantum Hall effect, carrier tunnelling, carrier confinement and Stark effects in both single quantum wells (QWs), coupled QWs and superlattices. The existing devices can be classed into four main groups, but with overlap of many of the structures into more than just one of these groups. Table 1 lists the members of these four main groups.

Two Dimensional Systems
SDHT-TEGFET-HEMT-MODFET
Quantum Wells
Quantum Hall Devices

Charge Transfer Systems
SDHT-TEGFET-HEMT-MODFET
Real Space Transfer Devices

One Dimensional Systems
Tunneling Structures
Superlattices
Quantum Well Wires

Band-Gap Engineered Structures
all of the above plus non-quantized-motion structures
Double-Heterostructure Lasers
Heterostructure Bipolar Transistors
(graded base or not)
Staircase Solid State Photomultiplier

Table 1 The four main categories of semiconductor heterostructure devices (after Weisbuch[15]). The class "band-gap engineered structures" is a general term for those structures that have had their physical properties modified by a tailoring of the band structure.

Together with device development there has been extensive study of both optical and transport properties of LDS from a fundamental point of view. To a considerable extent such studies have ignored phenomena associated with the carrier spin. As an example, ignoring the spin of the electron and hole, the 1s state of an exciton is frequently regarded as a single level whereas in reality, it consists of four spin levels.

The aim of this thesis is to extend the research on spin-polarised dynamics in GaAs/AlAs, GaAs/AlGaAs and InGaAs/GaAs low-dimensional structures. The forthcoming chapters will detail:

(a) The well width dependence of the electron, hole and excitonic Lande g-factors in a number of type I QW systems,

(b) The strength of the exchange interaction in type I excitons and the effect of the magnitude of the exchange mechanism on the spin-lattice relaxation time of the exciton,

(c) The carrier governing the spin-lattice relaxation time of type I excitons in the strong exchange limit and finally,

(d) Experimental evidence for the wave vector dependence of free hole relaxation time in quantum wells.

The bulk of the experiments are performed at superfluid liquid helium temperatures thus removing some of the complicating factors that can be present when experimenting at room temperature ie. phonon scattering, electron and hole gases. Limitations of the experimental apparatus partially forced us to work at 1.8K eg the magnet dewar which only delivers 10T at 1.8K. Theoretical treatment is though greatly simplified at low temperatures. For our purposes, the behaviour at higher temperatures is analyzed as a function of the change of behaviour from that exhibited at low temperature. The actual temperature dependence of quantum characteristics deserves extensive study in its own right.

The remainder of this chapter outlines the structure, growth and energy level configuration these LDS and finally some of the fundamental properties of the quantum well structure.

1.2 Types of Heterostructures

The building block of all the devices detailed in table 1 is the heterojunction. This is a single, low defect interface between two different materials. These hetero-interfaces exhibit an abrupt discontinuity in the local band structure. In doped material there can be gradual band bending in the neighbourhood of this discontinuity due to charge transfer that ensures the continuity of the Fermi level throughout the structure. This band bending then provides the confinement of the low-dimensional carriers.

A quantum well is formed when two undoped heterojunctions are grown back to back with a thin layer of one semiconductor sandwiched between two layers of another. The different band gaps and band alignment can then form a potential well in the sandwiched layer. A superlattice is simply a succession of these quantum wells linked together but with the criterion that the barriers linking these wells are sufficiently narrow that a significant level of tunnelling through these barriers can take place. The necessary thicknesses is of the order of a few tens of Angstroms. The formation of the conduction and valence bands is governed by the crystal lattice potential but quantisation of the energy levels within the conduction and valence band takes place as a result of the period of the superlattice potential, hence forming a series minibands within the conduction and valence bands. These miniband levels have successfully been described using the Kronig-Penny model[7].

According to the character of the discontinuity at the hetero-interface, the heterojunctions can be classed into the four different kinds shown in figure 1.1: Type I, Type II-staggered, Type II-misaligned and Type III. The band offsets are shown in the first column, the band bending and carrier confinement in the middle, and the corresponding superlattice structure on the right. The type I class applies to all the samples studied in this thesis. The band gap difference for the type I structure is given by $\Delta E_g = \Delta E_c + \Delta E_v$ where ΔE_c is the conduction band offset and ΔE_v is the valence band offset. For type II structures the energy gap is given by $\Delta E_g = | \Delta E_c - \Delta E_v |$ and the electrons and holes are confined separately in the different semiconductors. This structure applies to InAs/GaSb, $(InAs)_{1-x}(GaAs)_x$-$(GaSb)_{1-y}(GaAs)_y$[8] and InP-$Al_{0.48}In_{0.52}As$[9].

The GaAs/AlAs wells we study in chapter 4 can form both type I and type II structures (see figure 1.2). The cause of this is that although GaAs is a direct gap semiconductor with lowest conduction band at the Γ-point, pure AlAs is an indirect band gap semiconductor with its lowest conduction band at the X-point. For GaAs thicknesses less than 35Å the electrons are confined in the AlAs layer and the holes in the GaAs layer as at this point the $n=1$ electron sub-band lies above the AlAs-X valley. In the case of the $In_{0.11}Ga_{0.89}As$/GaAs wells studied in chapter 3 the first heavy-hole exciton transition is always type I but research has shown that the valence band configuration in these structures is dependent on the indium mole fraction. For indium compositions around 15% the valence band configuration is a mixed type with the first electron and heavy-hole levels confined within the lower band gap InGaAs (type I transition) but with the light-hole confined within the GaAs (type II transition). For lower indium compositions both systems may become type I. This has been observed specifically for an indium fraction of 0.05 by Mendendez et al[10].

The type II structures can be split into two sub-classes: type II-"misaligned " and type II-"staggered" as shown in figure 1.1B and C respectively. The final class is type III shown in D. This is formed when one constituent is semimetallic.

These band edge discontinuities at the hetero-interface govern the properties of quantum wells and superlattices and in turn, the relevant parameters for device design.

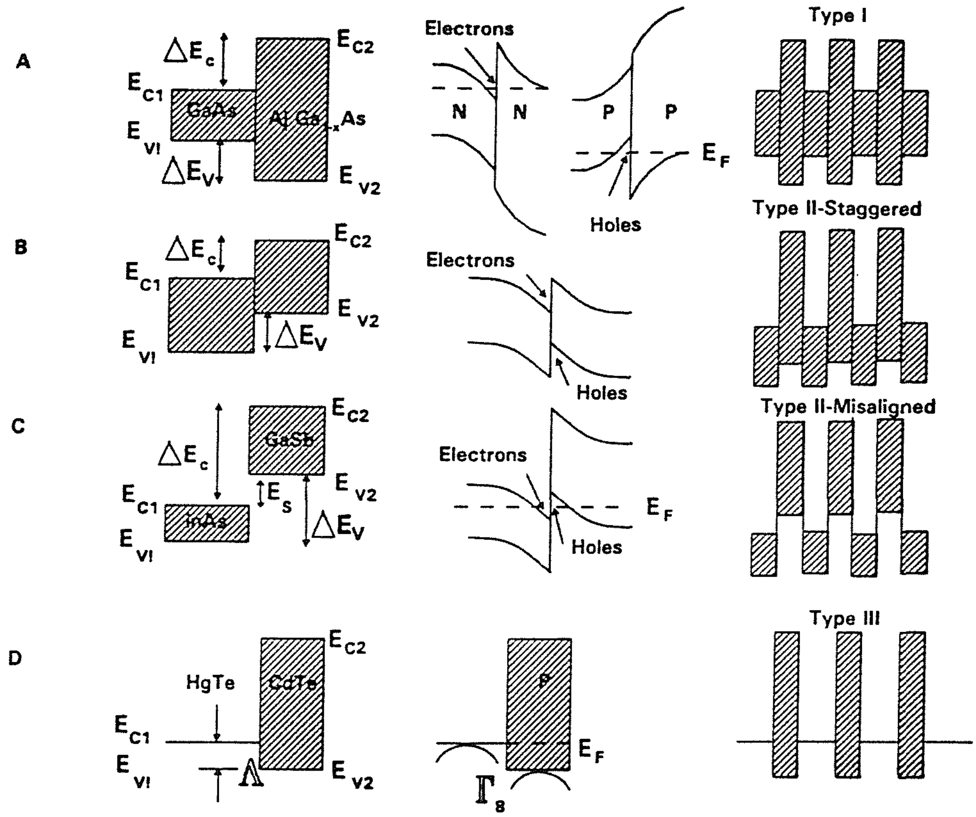

Figure 1.1 The four main kinds of heterojunction. The column on the left shows the band offsets, that in the middle the band bending and resultant carrier confinement in the undoped material and on the right, the corresponding superlattice for the heterojunction. The shaded regions indicate the band gaps.

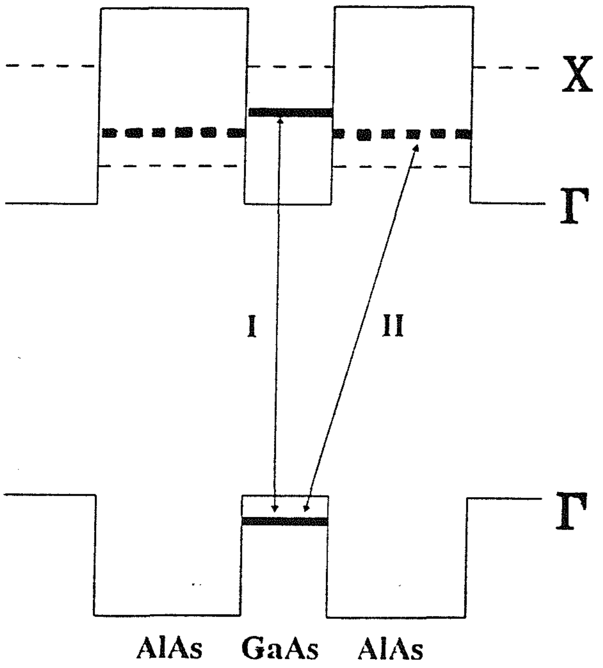

Figure 1.2 Band structure for GaAs/AlAs quantum wells. The solid lines indicate the subbands. The type I and type II transitions are indicated by the arrows.

1.3 Lattice Mismatch in Heterostructures

The growth of heterostructures consisting of different semiconductor materials is limited by the fact that the difference in lattice parameter between the heterostructure constituents must be small, often of the order of 0.1% for layer thicknesses >1000Å, in order to minimize the strain induced misfit dislocations associated with lattice mismatch. Misfit dislocations are created at the layer interface when the layer thickness exceeds a certain threshold value called the critical thickness. This critical thickness is determined by the lattice parameter mismatch.

A certain amount of elastic strain can be accommodated by a material without generating dislocations or defects. As long as the energy of the elastic strain is lower than the energy of dislocation formation the structure will be stable. The energy of the elastic strain increases with layer thickness up to a critical value frequently of the order of a few hundred Ångstroms above which misfit dislocations appear. This strain accommodation allows an increase of the lattice mismatch between the semiconductor constituents to as much as a few percent. Figure 1.3 shows a plot of the energy gaps and lattice constants for a number of zinc-blende structures and also some of the existing ternary alloys.

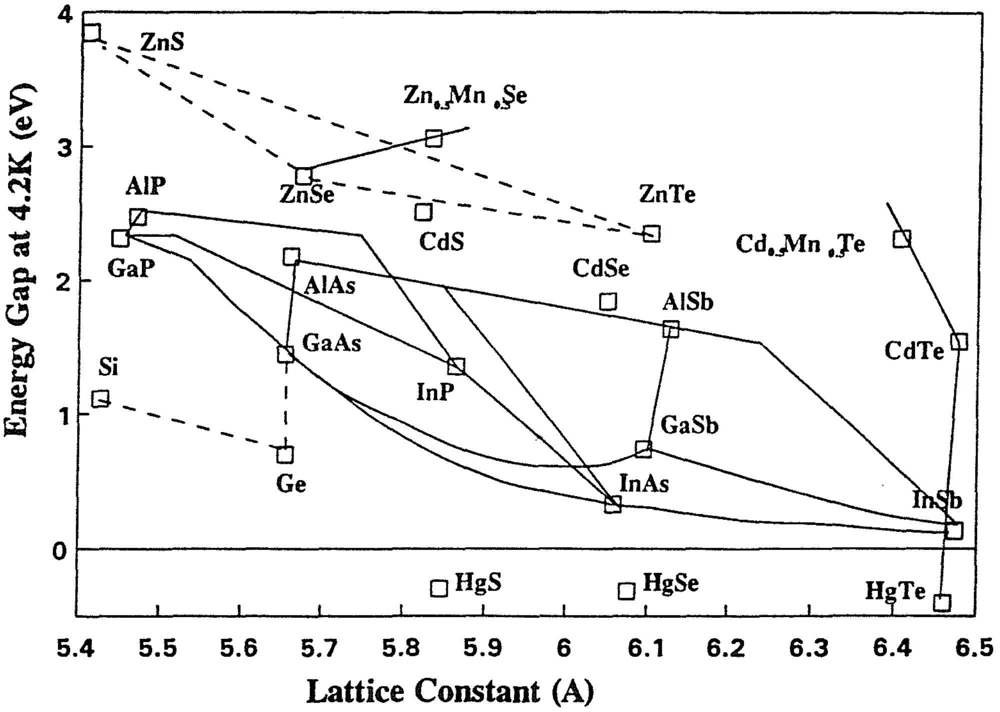

Figure 1.3 A plot of the energy gaps at 4.2K versus the lattice constant for zinc-blende semiconductors (Si and Ge are also shown). The solid joining lines represent ternary alloys that have been grown.

For the GaAs/AlGaAs structures we have studied the relative lattice mismatch between the host material of the heterolayers is small (=0.12%) and so strain modification to the band structure is negligible. The InGaAs/GaAs samples we study in chapter 3 though are a moderately strained system (1-2%). Strain accommodation by a bulk semiconductor lattice results in a lowering of the symmetry of the crystal from T_d to D_{2d}, which in turn leads to a removal of the degeneracy between the light- and heavy-hole bands in addition to that resulting from the quantum well potential. The effect of strain in these InGaAs/GaAs quantum wells is to further modify the band structure by pushing the heavy-hole band to even higher energies compared to that of the light-hole. The band structure in this case is determined by the effects of both the strain and the quantum confinement.

1.4 Electronic Properties of Semiconductor Heterostructures:

1.4.1 The Conduction Band

Using the simple model of an infinitely deep quantum well to describe a layer of material sandwiched between two layers of another material, then the energy levels of the conduction band of this well can be calculated in the approximation of the envelope function[11,12,13] using a Kane model[14]. If we assign z as the growth direction of the structure, $k_\perp$ as the transverse wave vector of the electron and $u_{ck}(r)$ as the Bloch wave function of the electron in the conduction band then

$$\psi = e^{ik_\perp \cdot r} u_{ck}(r) \chi_n(z) \qquad 1.1$$

describes the form of the electron wave function[11,12]. $\chi_n(z)$ is the envelope wavefunction satisfying the Schrodinger equation 1.2 for a particle with electron effective mass $m^*(z)$ with confinement energy ϵ_n with respect to the conduction band. The bottom of the conduction band is taken as the zero of energy.

$$\left(-\frac{\hbar^2}{2m^*(z)}\frac{\partial^2}{\partial z^2}\right)\chi_n(z) = \epsilon_n \chi_n \qquad 1.2$$

The ϵ_n are given by[15]

$$\epsilon_n = n^2\left(\frac{\pi^2\hbar^2}{2m^* L_z^2}\right) \qquad 1.3$$

where n is the quantum number 1,2,3,4..., $\hbar$ is Planck's constant divided by 2π and L_z

the quantum well width. The corresponding electron envelope in this infinite well are given by

$$\chi_n = A\sin\frac{n\pi z}{L_z} \qquad 1.4$$

Figure 1.4 shows the first three energy levels and wavefunctions for this infinitely deep quantum well. For a finite quantum well there is a reduction in the number of bound energy levels and penetration of the wave functions into the barriers. It has been shown that no matter the barrier height, there is always one bound energy level in a finite well.

In GaAs, the conduction band is two fold degenerate at the Brilloiun Zone centre and be can be described by spin angular momentum $S=1/2$ and $m_s=\pm 1/2$. The symmetry of the crystal results in a small spin splitting of the conduction band away from $k=0$. Electrons with the same wave vector k but with opposite spin orientations have different energies. Hence splitting of the conduction band is equivalent for the electron spin to the presence in the crystal of an effective internal magnetic field whose magnitude and orientation are dependent on the magnitude and orientation of k. This effective field gives rise to the most important spin-relaxation mechanism for conduction electrons: as the electron is scattered by defects it "sees" a fluctuating magnetic field which induces transitions between the spin states. The same mechanism operates in a quantum well and typically gives spin relaxation times of the order 10^{-9} sec.

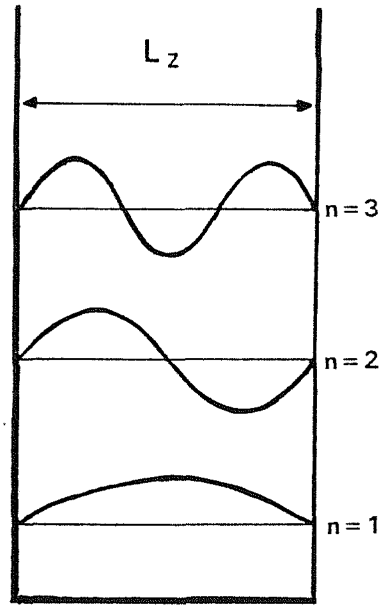

$$E_n = \frac{\hbar^2}{2m}\left(\frac{n\pi}{L_Z}\right)^2 \quad n=1,2,3...$$

$$\psi_n = A\sin\frac{n\pi Z}{L_Z}$$

Figure 1.4 The energy levels and wave functions of the confined states in an infinitely deep well. The wave function is zero in the barrier material for the infinite well.

1.4.2 The Valence Band

The Kane model[14] describes the bulk hole bands in a semiconductor material by basis functions with angular momentum J=3/2. This gives a picture of hole bands as four-fold degenerate at *k*=0. Near *k*=0, the dispersion of the heavy-hole $J_z=\pm 3/2$ and light-hole $J_z=\pm 1/2$ levels along the growth axis z, can be described by the Luttinger Hamiltonian. Quantizing the angular momentum along the z axis then this solves to give the valence band kinetic energy near *k*=0 for these hole levels as

$$E = \frac{\hbar^2 k^2_z}{2m_0}(\gamma_1 - 2\gamma_2), \qquad \text{for } J_z=\pm 3/2$$

$$= \frac{\hbar k^2_z}{2m_0}(\gamma_1 + 2\gamma_2), \qquad \text{for } J_z=\pm 1/2 \qquad 1.5$$

γ_1, γ_2 are the Luttinger parameters and $m_0/(\gamma_1 - 2\gamma_2)$, $m_0/(\gamma_1 + 2\gamma_2)$ are the heavy- and light-hole masses respectively.

A simplified treatment of the dispersion of the valence bands in a quantum well perpendicular to the z axis treats the quantum well potential as the first perturbation to the *k*=0 unperturbed states. This lifts the degeneracy between the hole bands present at *k*=0 in the bulk state due to the different effective masses and the fact the momentum is now quantized parallel to the growth axis. The Luttinger interaction is then treated as a new perturbation on these quantum well levels. The dispersion of the hole bands in a quantum well perpendicular to z is then given by

$$E = \frac{\hbar k^2_\perp}{2m_0}(\gamma_1 + \gamma_2), \qquad \text{for } J_z=\pm 3/2$$

$$E = \frac{\hbar k^2_\perp}{2m_0}(\gamma_1 - \gamma_2), \qquad \text{for } J_z=\pm 1/2 \qquad 1.6$$

Figure 1.5C shows the dispersion of the hole bands for this simple model together with the change from $J_z=\pm 3/2$ possessing a heavy-hole mass to that of a light-hole mass and vice versa for the $J_z=\pm 1/2$ level. In the approximation, this mass reversal leads to a crossing of the two hole bands, however the inclusion of higher order *k.p* terms in the valence-band Luttinger Hamiltonian leads to an increase in the heavy-hole mass and a reduction in the light-hole mass so that an anticrosssing[16] between these bands takes place (figure 1.5D).

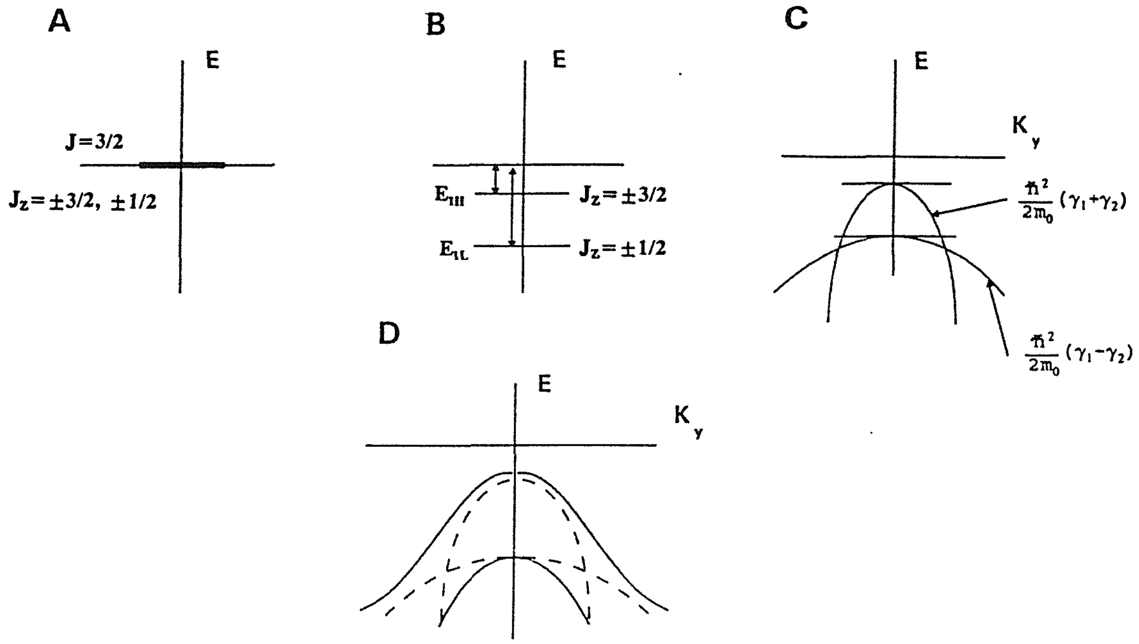

Figure 1.5 Hole dispersion curve for the simplified successive perturbation calculation detailed in the text. 1.5A shows the degeneracy of the light and heavy-hole bands that exist in bulk, B shows the lifting of this four-fold degeneracy by the quantum well potential at $k=0$, C the dispersion in the y direction due to the *k.p* interaction and D shows the modification of this dispersion when higher order *k.p* terms are taken into account.

1.4.3 The Two-Dimensional Density of States

In 3-D the parabolic nature of the conduction band leads to a continuous density of states defined by

$$\rho_{3D} = \frac{m^*\sqrt{2m^*E}}{\pi^2\hbar^3} \qquad 1.7$$

Once more m^* is the effective mass, E is the energy of the particle and $\hbar$ is Planck's constant divided by 2π. This is shown in figure 1.6 as the dashed line. Due to the quantization of electron motion along the z direction in a quantum well, within a single sub-band the electron possesses only two degrees of freedom along the x and y direction. This leads to a constant density of states per unit area of

$$\rho_{2D} = \frac{m^*}{\pi\hbar^2} \qquad 1.8$$

The total density of states per unit area for a quantum well is then

$$\rho_{QW} = \frac{m^*n}{\pi\hbar^2} \tag{1.9}$$

for $E_n<E<E_{n+1}$. It shows a step like appearance, exhibiting a discontinuity at each E_n (figure 1.6).

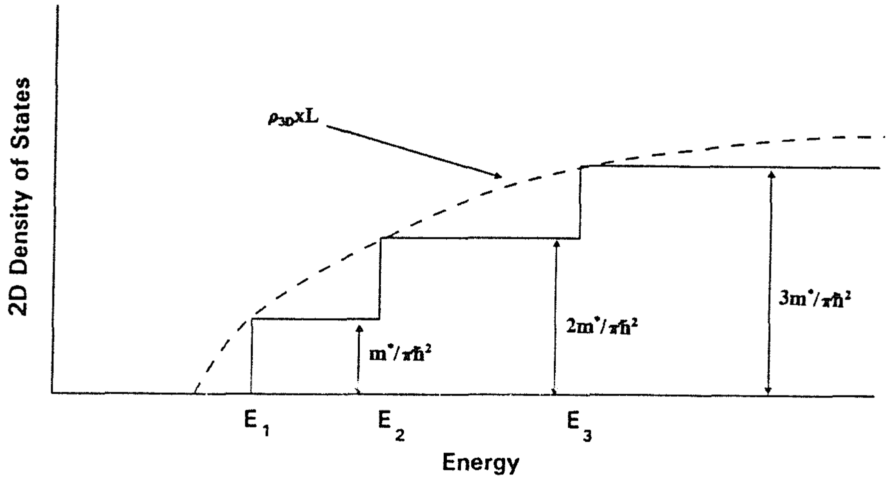

Figure 1.6 Comparison of the 2D and 3D density of states (after Weisbuch)[15]

1.5 Excitons

In undoped high quality quantum wells the main interband photoluminescence peak has been attributed to the transition of 2D bound electron and hole particles called excitons. These particles are formed due to the Coulomb attraction between the electron and hole which leads to the formation of this neutral bound electron-hole pair. An exciton can be treated as like a hydrogen atom with Bohr radius

$$a_B = \frac{4\pi\epsilon_0\epsilon_R\hbar^2}{\mu e^2} \tag{1.10}$$

where ϵ_R is the dielectric constant, e is the electronic charge and μ is the exciton reduced mass which is related to the electron effective mass m^*_e and the hole effective mass m^*_h

$$\frac{1}{\mu} = \frac{1}{m^*_e} + \frac{1}{m^*_h} \tag{1.11}$$

In a bulk semiconductor, the energy of a bound state p of this exciton is reduced in energy compared to that of the unbound electron and hole by an amount

$$E_{3D} = -\frac{\mu e^4}{2(4\pi\epsilon\hbar p)^2} \tag{1.12}$$

For the case of a 2D exciton in an infinitely deep quantum well the energy levels are related to the 3D bulk excitonic energy levels by

$$\frac{E_{2D}}{E_{3D}} = \frac{p^2}{(p-1/2)^2} \qquad 1.13$$

A strictly two dimensional exciton is expected to have a binding energy in the 1s state ($p=1$) four times greater than that of an exciton in three dimensions.

Calculations of the binding energy in a finite potential well for these 2D excitons by Bastard et al[17] using variational methods have shown that there is always Coulombic binding even in very wide wells and although there is a reduction in the binding energy from the infinite well case there is still considerable enhancement over the 3D bulk excitonic binding energy. Figure 1.7 shows the approximately four fold increase in the excitonic binding energy compared to that of the 3D exciton. This increase in binding energy gives the GaAs quantum well the rather unique quality that even at room temperature its optical properties are dominated by exciton effects, a situation normally associated with semiconductors with very large gaps.

The presence of excitons also plays a significant role in the density of states. This is revealed in the absorption spectrum of the exciton. In both 3D and 2D we observe an increase in the absorption coefficient in the continuum states compared to that for excitonless effects which can be described by the Sommerfeld factor. This change in absorption is as a result of the electron-hole correlation in the unbound states. Figure 1.7 shows this enhancement in the continuum states for both the 2D and the 3D case.

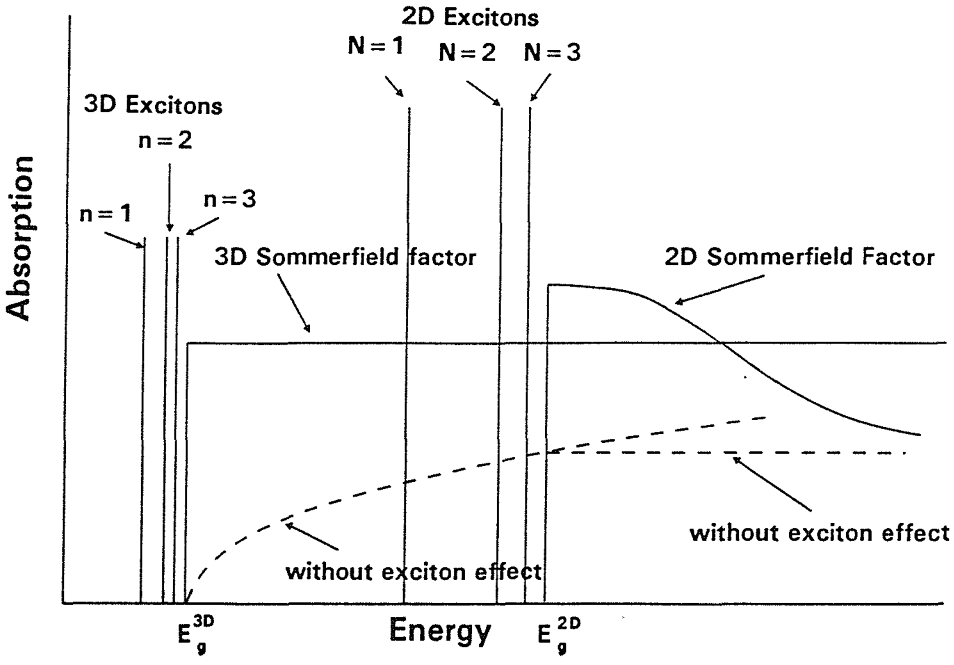

Figure 1.7 A comparison of the absorption components of the 2D and 3D excitons.

There is an approximate four-fold increase in the energy of the 2D excitons and the absorption in the continuum states is increased by the presence of excitons.

The bulk of the work in this thesis is on the excitonic fine structure and excitonic properties in differing semiconductor materials. Chapter 3 involves direct measurements of the excitonic Lande g-factor in type I GaAs/AlGaAs and InGaAs/GaAs quantum wells from the low field exchange splitting of the excitonic levels. Chapter 4 then measures the exchange interaction between the optically active and optically inactive levels of the excitonic structure in a number of type I structures and then chapter 5 studies the excitonic spin relaxation processes in modulation doped type I GaAs/AlGaAs wells.

1.6 Doping

In undoped MBE grown GaAs background carrier concentrations are normally as small as 10^{14}cm^{-3}. One of the major developments in quantum devices came when Dingle et al[18] produced a modulation-doped GaAs/AlGaAs superlattice that exhibited extremely high electron mobilities. This was achieved by doping only the larger band gap AlGaAs with silicon (n-dopant) and modifying the aluminium fluxes in the MBE so that when the carriers diffused through the layers they eventually became trapped in the lower band gap GaAs semiconductor as shown in figure 1.8. This was a great achievement as the separation of carriers from their donor or acceptor impurities greatly increases the carrier mobility as impurity scattering is reduced and so the distance which the carriers could propagate without dephasing is greatly increased.

The mechanism by which charge transfer takes place has been explained above but with this charge transfer so the band structure of the heterojunction/quantum wells are modified. The charge transfer achieves thermal equilibrium when there is continuity of the Fermi energy across the interfaces. This results principally from band bending but accumulation of carriers also causes band-gap renormalisation, a many-body effect which is evident as lowering of the conduction band and a raising of the valence band which results in a small reduction in the band gap.

The introduction of a large population of one type of carrier results in electrostatic "screening" of the opposite type of photo-excited carrier and so reduces the binding energy of a 3D exciton. This screening plays a greatly reduced role in the modification of the 2D exciton characteristics for which instead "phase space filling" is the dominant factor. This phase space filling is due to the thermalisation of the dopant carriers to the lowest energy level within the band and so, from the Pauli exclusion principle, these states are excluded from exciton formation. For significant carrier concentrations these effects cause the atomic exciton to unbind and the minority carrier constituent of the exciton to correlate with the majority carriers of the Fermi sea to form a Mahan exciton[19]. The Mahan exciton can be regarded as a bound state to the Fermi level. Increasing the carrier concentration further and the photoluminescence properties are now no longer governed by exciton effects but instead by the minority photoexcited carriers present in the well.

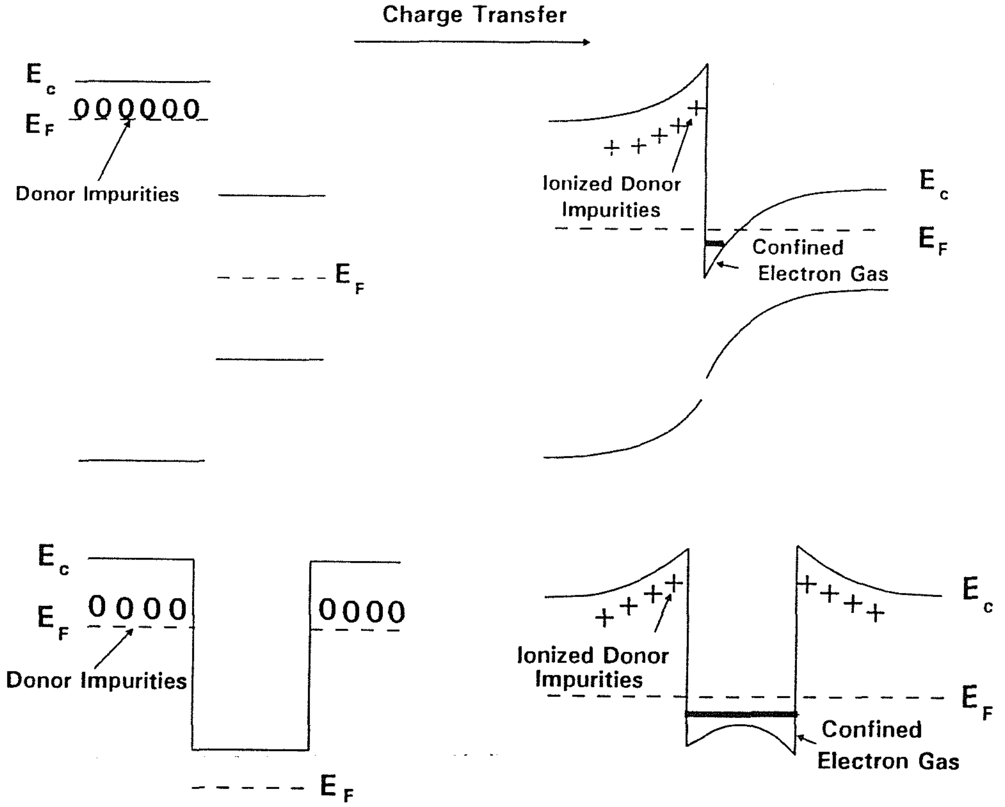

Figure 1.8 A schematic showing the band structure modification in the equilibrium state due to modulation doping. The top part of this figure shows modulation in a heterojunction, the bottom, modification in a quantum well.

1.7 Optical Pumping in Quantum Wells

One very important and extremely useful property of the quantum well is that due to the lifting of the degeneracy between the light and heavy-hole valence bands by the quantum confinement, the emission of the light-hole band is moved to higher energies with respect to that from the heavy-hole. This allows selective pumping and detection.

Absorption of circularly polarised photons creates electron hole pairs with predetermined spin orientation due to the selection rules for the transitions in bulk and quantum well shown in figure 1.9. Defining the polarisation as the difference between the number of spin up $n\Uparrow$ and spin down $n\Downarrow$ carriers over the total number photoexcited electrons or holes, $n\Uparrow + n\Downarrow$.

$$P_{e/h} = \frac{n_{e/h}\uparrow - n_{e/h}\downarrow}{n_{e/h}\uparrow + n_{e/h}\downarrow} \tag{1.14}$$

This diagram shows the significant possibility of obtaining 100% polarisation in quantum wells due to the removal of the valence band degeneracy. The lifting of this degeneracy also removes the mixing of the light and heavy-hole states which exists in 3D and results in very rapid spin relaxation of the hole in bulk. In a quantum well we observe a greatly increased spin relaxation time for the hole at $k=0$ compared to that in bulk although the contribution from the mixing of the valences bands away from $k=0$ in the quantum well does result in a reduction in the spin relaxation time compared to that measured at $k=0$. Hence, spin memory of the holes as well as the electrons is possible in a quantum well.

The circular polarisation of recombination light P_{rec}

$$P_{rec} = \frac{I^+ - I^-}{I^+ + I^-} \tag{1.15}$$

is determined by the spin relaxation during the lifetime of the carriers. In bulk, the holes relax very fast as a result of the mixing of the light and heavy-hole valence bands due to their degeneracy. Therefore the polarisation of the recombination light is determined by the electron spin relaxation. Due to the removal of the degeneracy in quantum wells though, the holes may relax slowly therefore the polarisation can be determined by the spin relaxation of both the holes and the electrons. If we define a spin-polarisation of the combined electron and hole system as $<S>$ then in general under CW optical pumping

$$\langle s \rangle = \langle s \rangle_0 \frac{1}{1+\frac{\tau_r}{\tau_s}} \tag{1.16}$$

where $<S>_0$ is the initial spin-polarisation allowed by the selection rules. $<S>$ is directly related to the polarisation of recombination light, $P=<S>$.

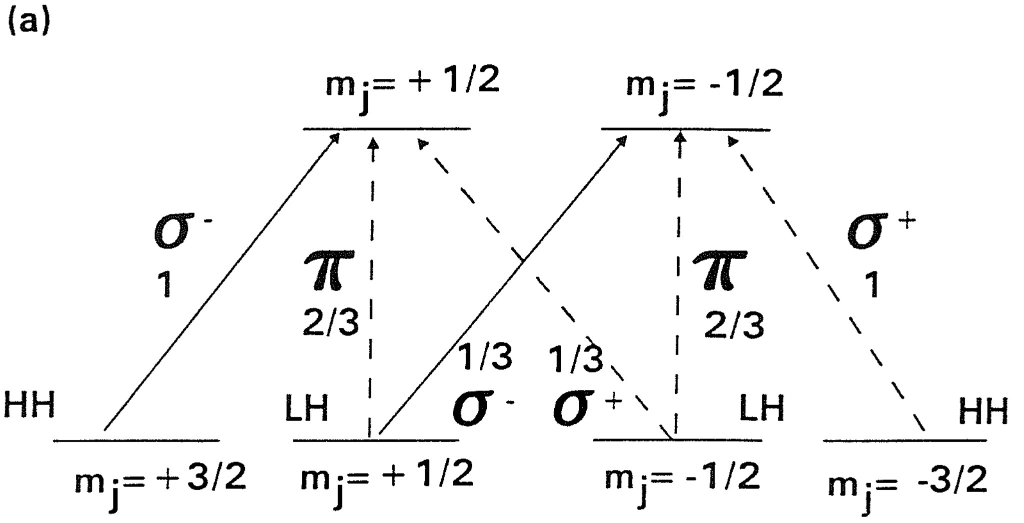

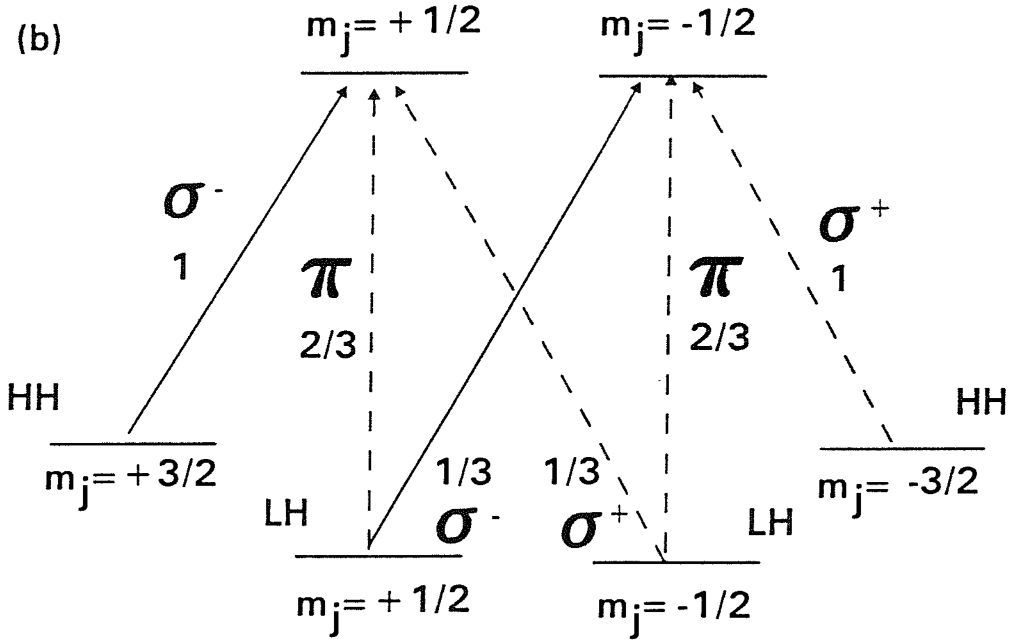

Figure 1.8 The selection rules and transition probabilities for band edge optical excitation in (a) Bulk GaAs, (b) GaAs/$Al_xGa_{1-x}As$ quantum wells.

1.8 References

1 Molecular Beam Epitaxy	A.Y.Cho, J.R.Arthur	Prog.Solid.State.Chem. 10(1975)157
2 Crystals: Growth, Properties and Applications	K.Ploog	Vol3. Springer-Verlag,Berlin and NY (1980)
3 Handbook of Semiconductors	L.L.Chang	Vol3. North-Holland Publ.(1980)
4 Molecular Beam Epitaxy and Heterostructures	L.L.Chang,K.Ploog	Proc.Erice 1983 Summer School. (1985)
5 New Transport Phenomenon in a Semiconductor Superlattice	L.Esaki,L.L.Chang	Phys.Rev.Lett. 33(1974)495
6 Quantum States of Confined Carriers in Very Thin $Al_xGa_{1-x}As$-GaAs-$Al_xGa_{1-x}As$	R.Dingle,W.Weigmann,C.H. Henry	Phys.Rev.Lett. 33(1974)827
7 Quantum Mechanics of Electrons in Crystal Lattices	R.de.L.Kronig,W.J.Penny	Proc.Roy.Soc.,vol.A130, pg499-513, (1930)
8 $In_{1-x}Ga_xAs/GaSb_{1-x}As_x$ Heterojunctions by Molecular Beam Epitaxy	L.Esaki	Appl.Phys.Lett. 31(1977)211
9 Staggered-lineup Heterojunctions as Sources of Tunable Below-Gap Radiation: Experimental Verification	E.J.Caine, S.Subbanna, H.Kromer,J.L.Merz,A.Y.Cho	Appl.Phys.Lett.45(1984)1123
10 Large Valence-Band Offset in Strained-Layer $In_xGa_{1-x}As/GaAs$ Quantum Wells	J.Menendez,A.Pinczuk,D.J. Werder,S.K.Sput,R.C.Miller, D.L.Sivco, A.Y.Cho	Phys.Rev B 36(1987)8165
11 Superlattice Band Structure in the Envelope-Function Approximation	G.Bastard	Phys.Rev.B. 24(1981)5693
12 Theoretical Investigations of Superlattice Band Structure in the Envelope-Function	G.Bastard	Phys.Rev.B. 25(1982)7584
13 Heterojunctions and Semiconductors Superlattices	M.Altarelli	Springer-Verlag, Berlin and NY (1985)
14 Semiconductors and Semimetals	E.O.Kane	Vol.1. Academic Press, NY (1966)
15 Semiconductors and Semimetals	C.Weisbuch	Vol.24. Academic Press, NY (1987)
16 Optical Properties in Modulation-Doped GaAs	G.D.Sanders,Y.C.Chang	Phys.Rev.B 31(1984)6892

17 Exciton Binding Energy in Quantum Wells	G.Bastard,E.E.Mendez,L.L. Chang,L.Esaki	Phys.Rev.B 26(1982)1974
18 Electron Mobilities in Modulation-Doped Semiconductor Heterojunction Superlattices	R.Dingle,H.L.Stormer,A.C. Gossard,W.Weigmann	Appl.Phys.Lett. 33(1978)665
19 Excitons in Degenerate Semiconductors	G.D.Mahan	Phys.Rev. 153(1967)882
20 Theory of spin orientation in "Optical Orientation"	M.I.D'yakonov, V.I.Perel	Modern Problems in Condensed Matter Sciences 8(1984)11 North Holland

2 Experimental Apparatus and Sample Details

2.1 Summary

In this thesis we have applied the basic techniques of optical pumping to a number of type I single and multi-quantum well structures, studying for each, a range of well widths to determine the degree of carrier spin polarisation. Below we describe the general experimental set-up used for most of the experiments, followed by detailed descriptions of the experimental apparatus, optical and electrical components together with the data acquisition process and a description of all the samples studied.

2.2 Experimental Set-up

Figure 2.1 shows the standard experimental arrangement used throughout this thesis. This arrangement produces pure right or left circularly polarised light for excitation and detection is of the degree of circular polarisation of the luminescence. Specific modification to this arrangement for a particular experiment will be dealt with in the relevant chapter.

As shown, the excitation source was either the Spectra Physics model 3900S, CW Ti:Sapphire or the Coherent CR599 dye laser pumped by a Spectra Physics Argon Ion laser. It should be noted at this point that the pumped dye laser produced essentially vertical linear polarised light but the Ti:Sapphire lased with essentially horizontally linear polarised light.

The 530nm filter situated in front of the output of the pumped laser was used to remove any stray AR^+ light. The ND filters served to reduce the light intensity, if necessary, and a component of the remaining light ($\approx 4\%$) was then reflected by a beam splitter into a power meter for normalisation of the signal intensity. The remainder was directed by steering mirrors through either a vertical linear polariser, if the dye laser was in use, or through a horizontal linear polariser in the case of the Ti:Sapphire so as to

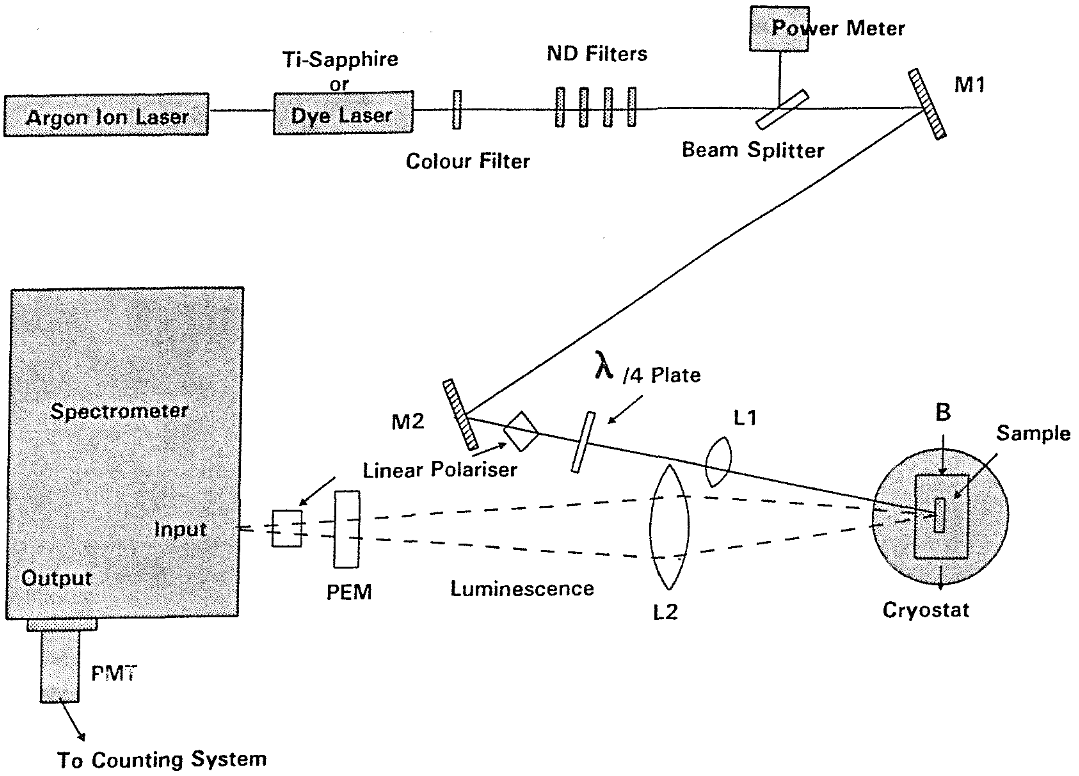

Figure 2.1 The experimental arrangement most commonly used throughout this thesis.

ensure pure linear polarisation entering the λ/4 plate and therefore pure circular polarisation incident on the sample. The beam was then focused down to approximately a 200μm diameter spot by a f=25cm biconvex lens onto the sample surface which was situated inside the cryostat and located centrally in the bore of the 10T superconducting magnet.

The luminescence from the sample was collected and focused by an f=45cm convex lens through the photo-elastic modulator (PEM) and then through a vertical linear polariser onto the input slits of the spectrometer. The combination of photo-elastic modulator and linear polariser passed alternately left and right circularly polarised light at the modulating frequency of 50kHz.

The light transmitted through the spectrometer was detected by an infra-red sensitive GaAs photomultiplier tube and the pulses from this amplified by a preamplifier before being passed to both a ratemeter based system for immediate display of the luminescent intensity and, to a digital counting system which consisted of a dual channel gated counter with the reference signal for the gates taken from the PEM. The count rate was shown on a digital display but also automatically stored in a number of formats.

2.3 Lasers

Three lasers were used throughout the work. These were the Spectra Physics 171

Argon-ion laser, a Coherent CR599 continuous wave (CW) tunable dye laser copy and the Spectra Physics model 3900S CW Ti:Sapphire laser.

2.3.1 The Argon-Ion Laser

The Ar^+ laser was driven by a 410V 3-phase power supply delivering 45A and was capable of a maximum power of roughly 10W when cooled by an outside water supply. The laser was run without wavelength selection for all the experiments so lasing was predominantly for output wavelengths of 488nm and 514nm. When pumping the dye laser maximum pump power between 4W and 5W was used as beyond this we observed output saturation. For the Ti:Sapphire 6W was found to be a suitable pump power for the wavelength range we wished to work in.

2.3.2 The Dye Laser

The dye laser cavity consisted of three mirrors that produced standing waves along the cavity length. The active medium was an organic dye (Pyridine 2 or DCM) dissolved in ethanediol (ethylene glycol) to give concentrations of between 10^{-4} to 10^{-3} molar. The circulating dye was cooled by an external water supply to maintain viscosity and the stability of the dye solution and to optimise the lasing efficiency and lifetime of the dye.

Tuning was achieved using a birefringent filter. This consisted of three parallel crystalline quartz plates set at Brewster's angle to the dye laser beam. These acted as full wave plates with alteration of the angle between their combined fast and slow axes and the pump beam polarisation producing a different minimum loss wavelength to lase on. This enabled selection of lasing wavelengths over the full range of both dye gain curves and so, we were able to pump selectively in the range 620nm to 800nm (the range of DCM is 620nm to 740nm and that of Pyridine 2 680nm to 800nm). We were also able to extend the long wavelength range out to approximately 820nm by replacing the pyridine output coupler with that used with Styryl 9 dye. This was achieved only at the expense of the mid-range power and the minimum lasing wavelength which was now decreased to approximately 700nm. Peak powers in the region of 300mW were obtained when pumping at the gain centre with full power of 5W from the Argon ion.

2.3.3 The Ti:Sapphire Laser

As the name suggests, the active medium here is a Ti^{3+} -doped crystal. The Ti^{3+} ion is responsible for the laser action when a high inversion density is achieved in the crystal. According to manufacturers specification the tuning range available from the model 3900S is from 675nm to 1100nm when pumped with 20W.

The laser consists of a four-mirror folded cavity as shown in figure 2.2. The pump light is focused to a narrow line within the rod and the oscillating laser mode is similarly focused and overlapped within the same volume. The rod is cooled continually by externally supplied chilled water circulating around its holder. This adds to the efficiency of the inversion process.

Tuning of the laser is achieved with a birefringent filter similar to that of the dye laser. The broad tuning range of the Ti:Sapphire overlaps two orders of the filter but the mirror set only allows one order to oscillate at a time. For initial set-up, the filter is installed and adjusted for the 700nm to 850nm range. To operate in the range 850nm to 1000nm, the filter must be rotated in its holder and the optics set changed from the 675nm to 750nm set to a 950nm to 1100nm set.

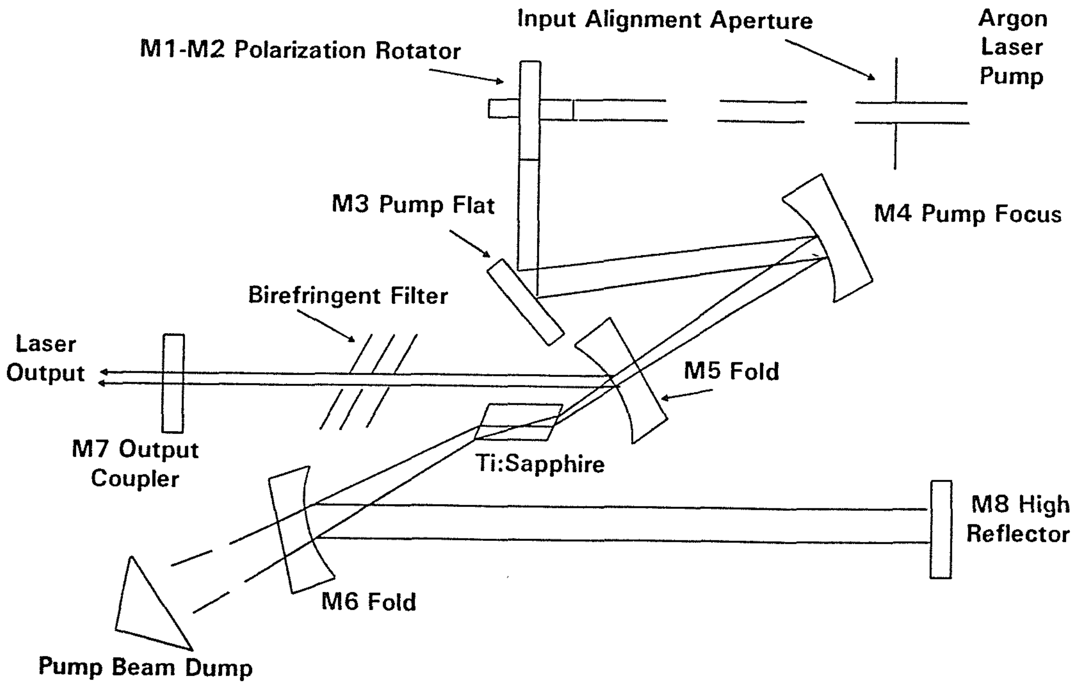

Figure 2.2 The Cavity of the Ti:Sapphire

We found that pumping with 6W of argon laser light and using the optics set designed for the 675 to 750nm range we could achieve output powers of 300mw quite easily over a tuning range of 675nm to 780nm (approximately). Laser power dropped quite significantly beyond 780nm and below 620nm, with lasing ceasing just beyond 800nm and just below 610nm.

2.4 Cryostats

Two cryostats were used for the experiments; a single transfer dewar made at the Clarendon Laboratory Oxford containing a superconducting magnet from Cryogenic Consultants Ltd and an Oxford Instruments variable temperature continuous flow cryostat.

2.4.1 Single Transfer Cryostat

This Clarendon built cryostat was used in the majority of the experiments described in this thesis. This cryostat was able to hold about 8 litres of liquid helium pumped down to superfluid helium temperature of 1.8K for around 12 hours and liquid helium at 4.2K for roughly 24 hours. Figure 2.3 shows the basic structure of this cryostat. It consists of a vacuum jacket surrounding an outer can that can hold roughly 10 litres of liquid nitrogen which, in turn, encloses an inner helium chamber. The bottom of the nitrogen can is attached to a radiation shield surrounding the remainder of the helium space. The outer cryostat wall, the radiation shield and the helium can each have one fused quartz window that enables the exciting light to be directed through the vacuum space and liquid helium onto the sample.

The helium space contains an insert made from four parallel tubes that run the length of the nitrogen space and are individually joined to four disc-like copper baffles, each cut slightly smaller than the diameter of the helium can, that act as radiation shields. Attached at various points on the insert are radioresistors that are used to indicate the level of liquid helium in the dewar. Samples mounted on a copper holder attached to the end of a hollow stainless steel rod are inserted through a vacuum tight seal in this insert lid and directed down the length of the helium container until they are level with the windows at the centre of the magnet. Copper wire wound as lose springs around this rod act as both a guide for inserting the sample rod centrally and also help prevent any lateral vibration of the sample.

The insert also holds the 10T superconducting magnet. This is situated so that the sample can be placed centrally in its bore when the magnet is oriented with its bore either

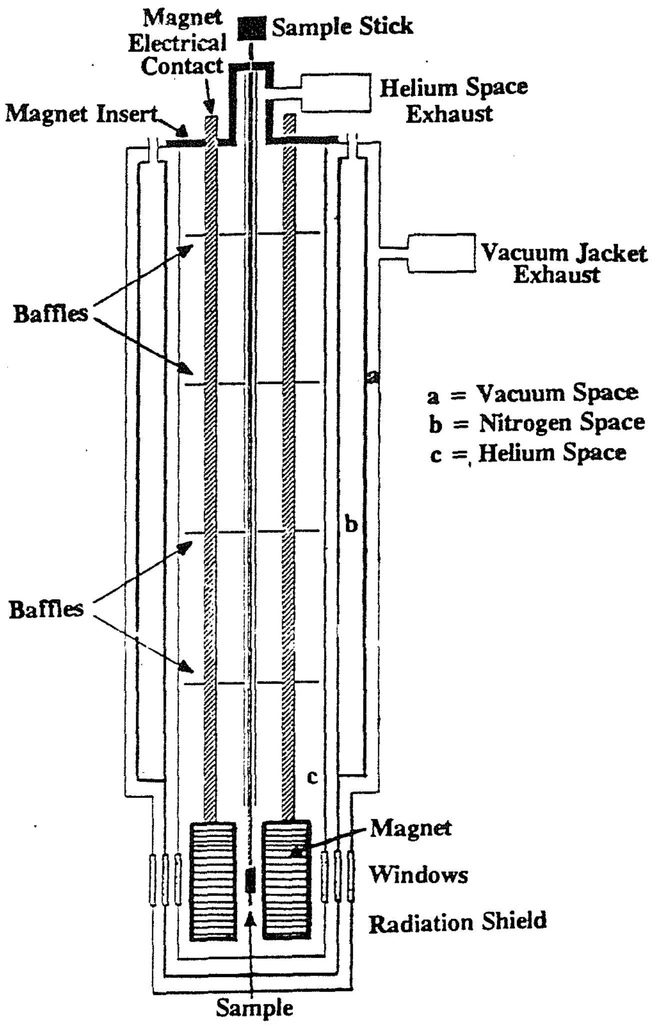

Figure 2.3 The Clarendon built single transfer cryostat.

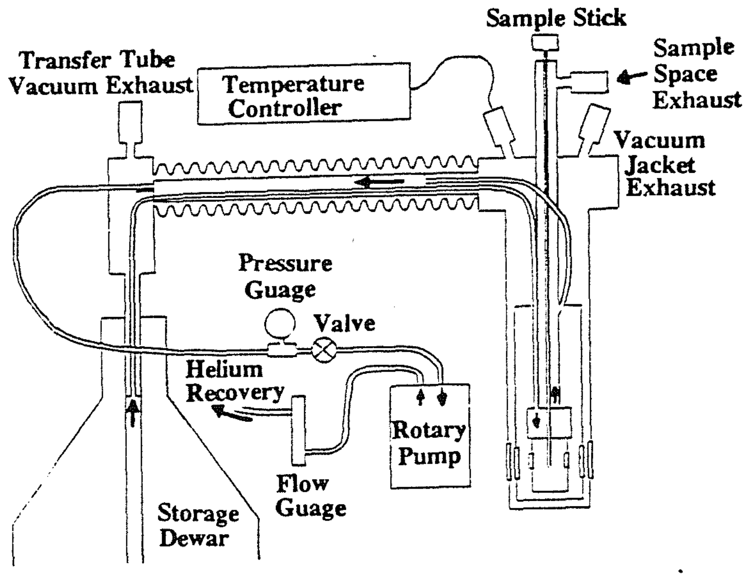

Figure 2.4 The Oxford Instruments Continuous Flow cryostat.

parallel or perpendicular to the axis of the window. Current to the magnet is carried in two of the support tubes.

In operation the system needed approximately 2 hours and 15l of liquid helium to cool down to liquid helium temperature. It was necessary to operate at 1.8K to ensure that the liquid helium was free from bubbles.

2.4.2 The Continuous Flow Cryostat

This Oxford Instruments cryostat was used for measurements as a function of temperature at zero magnetic field. It needed 1.5 litres of liquid helium and half an hour to make the transition from room temperature to 4.2K and from here 0.5 litres an hour to maintain this temperature. The sample was located in a stream of flowing cold helium gas, rather than in liquid, and its temperature was controlled using a combination of flow rate and heat, supplied to the sample rod by a temperature controller.

The main difficulty in use of the single transfer cryostat was that it was prone to localised heating effects on the sample if the exciting laser light intensity was too high. This caused some instability in the sample temperature but was a more significant problem when experimenting at the lower end of the temperature scale.

Figure 2.4 shows the structure of the cryostat together with the flow mechanism. The cryostat consists of an outer vacuum space in which a radiation shield surrounds the helium container. Helium liquid was sucked up through the transfer tube via the regulating needle valve, into the cryostat to just above the level of the windows. To improve efficiency the exhaust helium gas from the helium space was passed back along an annular outer space of the transfer tube through a pressure gauge and flow control valve onto a rotary pump and finally through a flow meter.

2.5 The Magnet

The magnet used was supplied by Cryogenic Consultants Ltd. It was a split solenoid of bore 30mm that was capable of producing 10T across its horizontal axes, the transverse access ports had a 6mm diameter. It required 75A to drive it to this maximum value which was supplied by an Oxford University built power supply. The current supplied was controlled by a variable sweep rate current controller again built at Oxford University.

2.6 Spectrometer

The spectrometer used throughout was a Czerny Turner single plane grating, half metre focal length, Spex model 1870 (figure 2.5). The output wavelength could be changed by rotating the diffraction grating manually, or by using a stepper motor. The input and output slits were set normally between 20-100μ which appeared to give the best compromise between resolution and transmitted light intensity (see figure 2.6). The input slit was normally masked by a circular aperture of diameter 1mm as were the output slits on the inside of the spectrometer to eliminate effects of any stray internal reflections. The resolution, in this particular model, was further improved by the covering of all gratings and mirrors by factory built masks, although this did reduce transmitted light intensity. For the experiments in chapter 4 detecting level crossing signals, we wished to monitor as close to the whole luminescence line shape as possible, so for this purpose the masks on the input and output slits were removed and the slits were set to 2mm. Resolution here was sacrificed but was deemed necessary as intensity was our first priority.

Calibration of this spectrometer was carried out against the neon spectrum. It showed a systematic offset in the region of 7Å together with a periodic error of approx. ±1Å. Temperature induced changes from day to day were also about ±1Å. The performance of the spectrometer was obviously poor but because the spectral features studied were generally wide it was adequate.

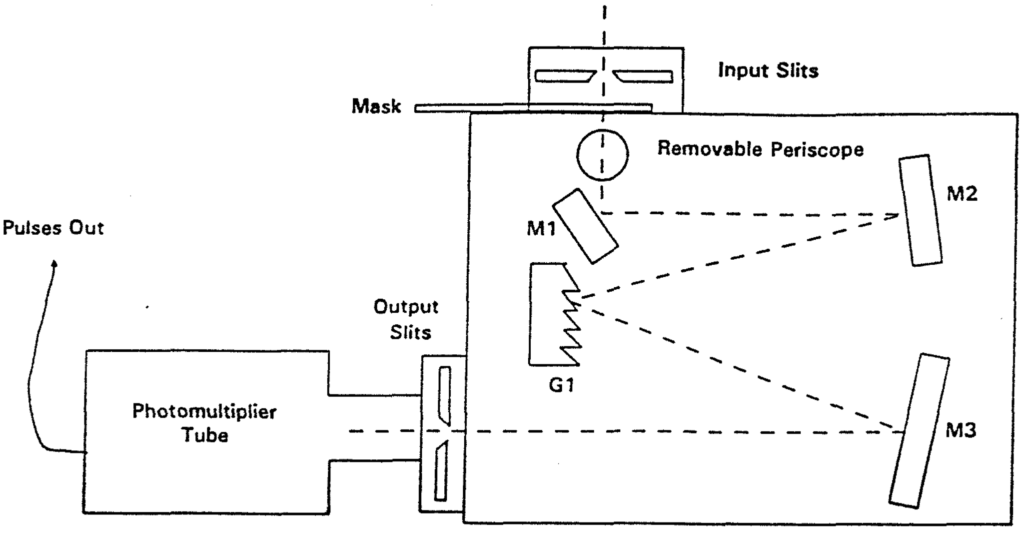

Figure 2.5 Czerny Turner Spex model 1870 1/2m spectrometer.

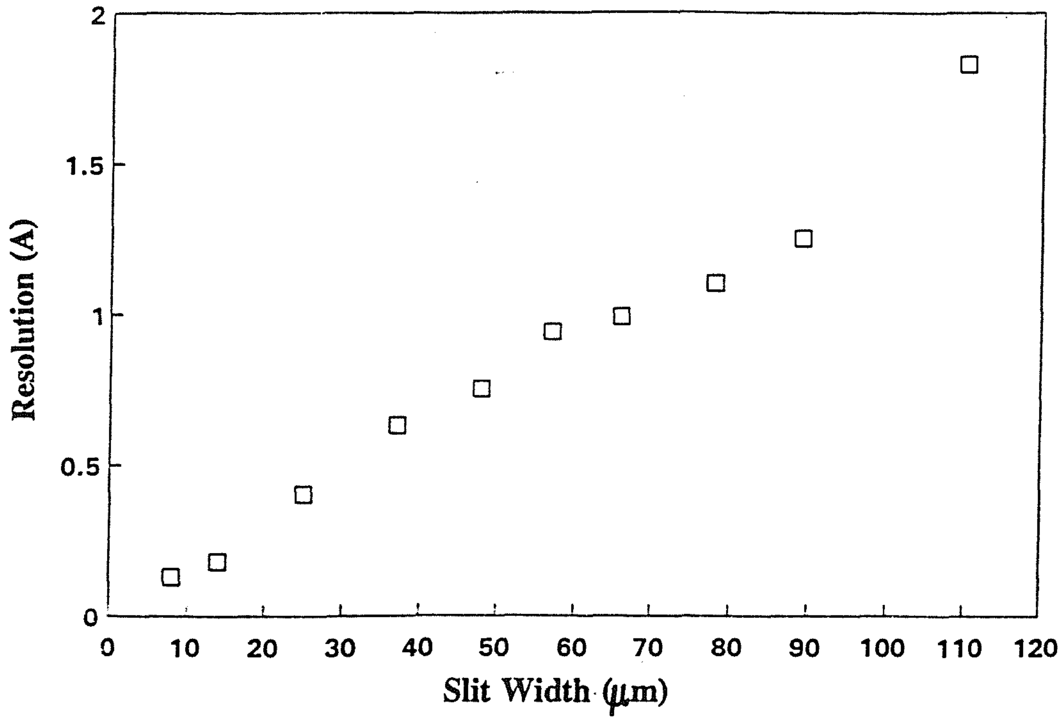

Figure 2.6 Resolution of the spectrometer as a function of slit width.

To aid in the alignment of the spectrometer with the sample, a small prism periscope was situated immediately after the input slits giving a view of the focused beam incident on the sample. After alignment this was lifted up out of the way of the incoming light.

A Hamamatsu R943-02 photomultiplier tube with GaAs photocathode was permanently attached to the output slits. This, when cooled to around -25°C by a water chilled Peltier cooler gave a dark count of less than 20cps and had a roughly constant quantum efficiency over the spectral range 160nm-930nm.

2.7 Polarisers

The linear polarisers used were made from the plastic dichroic polarising sheet HN7. This material was optimised for transmission of light in the range 720nm to 820nm, wherein it transmitted roughly 80% of linearly polarised light parallel to its axis. Within this range, it transmitted less than 1% of the light polarised orthogonal to the polariser axis for wavelengths less than 800nm, but this increased to a transmittion of up to 5% when light incident on the polariser increased to 820nm. The quarter wave plates were made from optically active WRO2 plastic sheets which were optimised for 800nm. Within the wavelength range of our experiment the percentage loss in polarisation occurring on transmission through these polarisers was negligible.

2.8 Photo-elastic Modulator (PEM)

The model used was a Hinds International PEM-80. Its purpose was to vary the polarisation of the light by strain-induced birefringence. The PEM consisted of a rectangular slab of fused quartz set in longitudinal mode vibration at its natural frequency (55kHz) by a matched piezoelectric transducer. The oscillatory deformation of the fused quartz gives a correspondingly oscillatory birefringence with axes parallel and perpendicular to the transducer axes. It therefore acts as an oscillatory wave plate with a maximum phase difference between components set by the amplitude of oscillation. This was adjusted such that a circularly polarised wave that entered the modulator was linearly polarised after transmission at the extrema of the oscillation and at intermediate points of the cycle the transmitted polarisation was elliptical.

The theoretical transmission of σ^+ polarised light through a combination of PEM and plane polariser is shown in figure 2.7. It has the shape of

$$\frac{1}{2}[1+\sin\frac{2\pi L\Delta n(t)}{\lambda}]$$

where $\Delta n(t) = \Delta n_0 \sin\omega t$ is the time dependence of the birefringence of the modulator plate, L is its thickness and λ the optical wavelength. This gives an intensity variation at the modulator frequency (55kHz) which has maxima flattened compared to a $\sin^2(\omega t)$ dependence. For σ^- incident light the transmitted intensity is in antiphase with the σ^+ curve shown in figure 2.7.

The drive to the PEM provided a reference signal which was used to trigger a dual channel gated photon counter. The gates for the two channels A and B were set to open at the phases indicated in figure 2.7 with the dead time (with gates closed) as shown. We can see from this that although the oscillations of the phase delay is not a square wave, for quite small dead times we can measure a difference of intensity in the two gates close to the value expected for square wave modulation. A value of 65% dead time was chosen as a reasonable compromise.

In practice the set-up was calibrated by observing the intensity modulation for pure σ^+ input at a particular dead time setting. The degree of polarisation of an unknown beam was then calculated as a ratio of the measured value to this calibrated value.

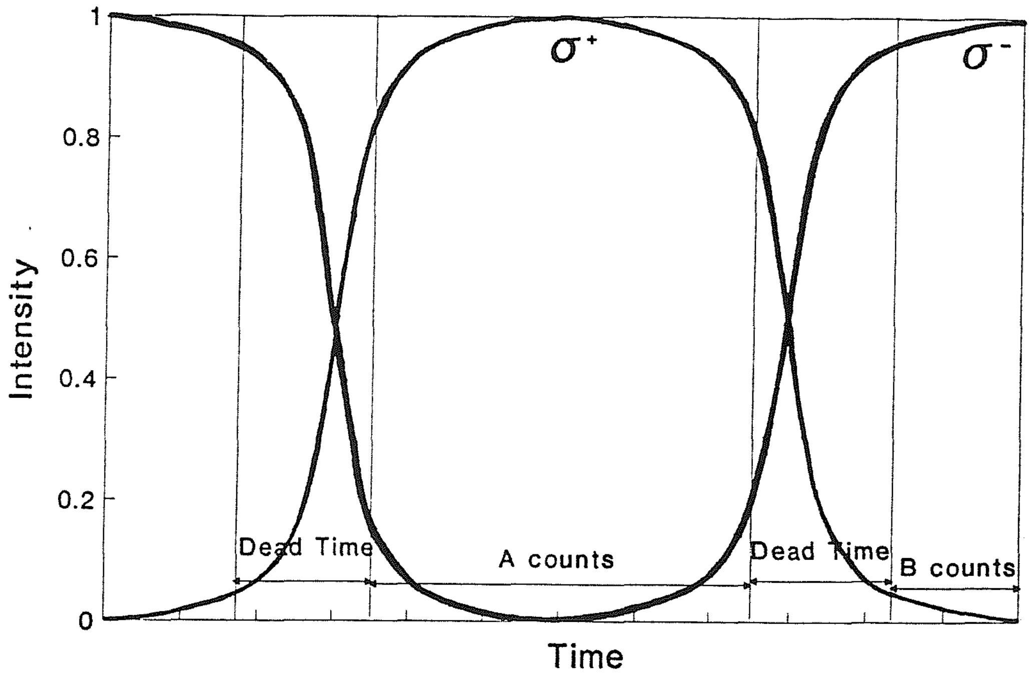

Figure 2.7 Theoretical transmission of σ^+ polarised light as a function of time from the external trigger

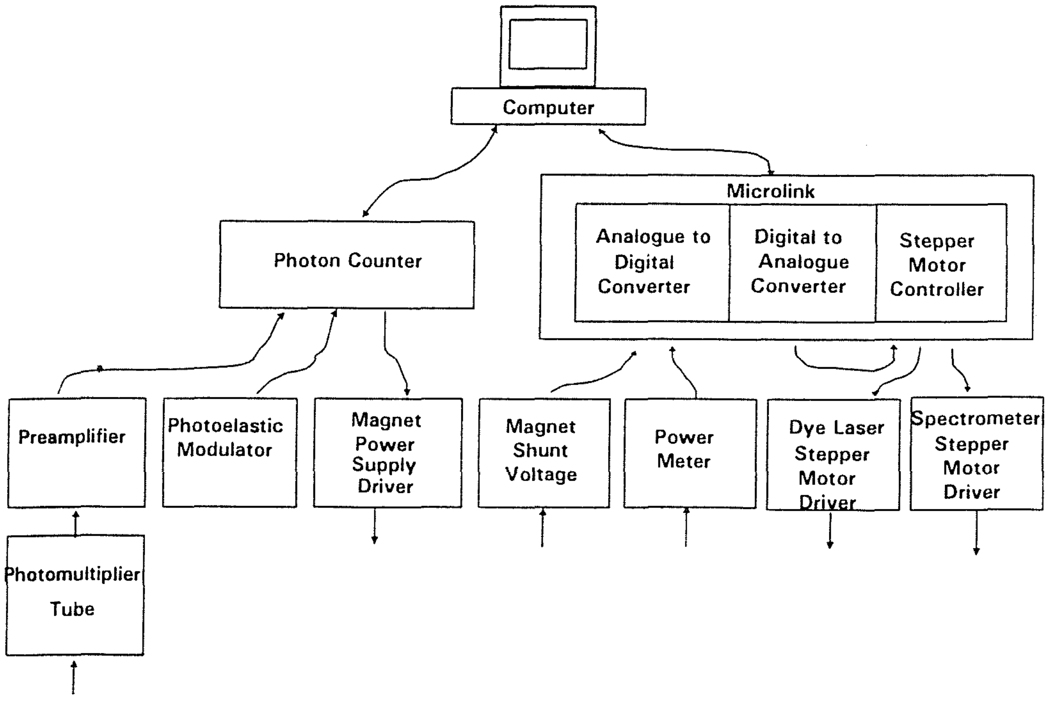

Figure 2.8 Flow diagram of the control and acquisition of data.

2.9 Data Acquisition

The data gathering was performed by an IBM PC AT computer running Asyst 1.56. This was linked to a Stanford Research RC400 two channel gated photon counter and a Microlink multiplexing frame by an IEEE/GPIB board (see figure 2.8). Near total automation of the experiment was achieved through a programmable stepper motor controller card driven by analogue signals sent from the Microlink frame. This drove both the dye laser and Ti:Sapphire stepper motor drivers and also the spectrometer stepper motor. These could be driven at a variety of step sizes but also had the added advantage that the mechanical backlash was consistently removed.

The magnetic field was also driven by the computer from the digital to analogue converter in the photon counter. The rate at which the field was changed was set independently by a sweep rate control in the magnet power supply. Once a field strength was reached the field could be monitored via the voltage signal from a shunt resistor within the magnet power supply that was converted into a digital read-out by one of the Microlink analogue to digital convertors. The calculated current-field calibration of the solenoid was assumed. The laser power was similarly monitored using an A-D microlink input. For each setting these digital signals were monitored for approximately a quarter of a second at 110Hz and the values then averaged.

The process for data acquisition was as follows: Pulses from the photomultiplier tube were amplified by an SR440 preamplifier. The output from this passed in alternating half cycles of the PEM to the photon counter which incorporated pulse height discriminators. The maximum count rate that could be recorded by the system without significant distortion due to pulse overlap was approx. 200,000s^{-1}. Count rates of several million could be tolerated by the system without damage to the photomultiplier tube.

The number of counts recorder by the photon counter in alternate half cycles were automatically stored along with the integrated power from the laser on disc at the end of a run. This enabled easy data analysis and also increased significantly the volume of data that could be handled. Together with automatically storing the data on disk after a scan, the Asyst package converted the incoming data to polarisation values, normalised the data with respect to the laser power and displayed graphs showing the laser power and counts recorded in each channel of the photon counter in their raw state. Once the starting conditions of the experimental apparatus were relayed to the computer, total automation of the experimental apparatus was possible along with the ability to take entirely automated repetitive scans with the only manual intervention required when optical alignment is necessary.

There was one main flaw in the experimental arrangement which was associated with the design of the Stanford photon counter. The pulses to the two channels were discriminated by different discriminator circuits. These discriminators were unavoidably not identical, so identical settings for the discriminators did not lead to exactly the same count rate in each channel for input of identical pulse trains. The error in this was as much as 5%, so for accurate absolute polarisation measurements, the discriminator levels were set to slightly different values to balance the sensitivity of the channels. The day to day reproducibility of absolute polarisation measurements was of the order of ±0.5%.

2.10 Samples

Our samples were supplied by Philips Research Laboratories (Dr. C.T.B. Foxon), by GEC Research (Dr S.R.Andrews) and from Nottingham University (Prof. L.Eaves). The majority of the samples studied were nominally undoped and of very high quality. These consisted of a number of type I GaAs/$Al_{0.36}Ga_{0.64}As$, GaAs/AlAs and $In_{0.11}Ga_{0.89}As$/GaAs quantum wells, work on which, contributed to the bulk of the material in this thesis. The remaining samples, fell into two separate categories. One of the samples was an undoped GaAs/$Al_{0.3}Ga_{0.7}As$ structure grown on an n-type substrate and had its carrier concentration controlled by an external bias enabling carriers of different types and differing concentrations to be injected into the wells. The others were n-type modulation doped GaAs/$Al_{0.33}Ga_{0.67}As$ single QWs.

Below we describe in full detail all the samples studied.

2.10.1 The G-samples

All the G-samples were grown at Philips Research Laboratories, Redhill by molecular beam epitaxy using a Varian Gen II machine. Two series of GaAs/$Al_xGa_{1-x}As$ structures were investigated grown with different Aluminium concentrations, x=0.36 and x=1:-

GaAs/$Al_{0.36}Ga_{0.64}As$

G50	G57	G51	G55	G52
25.7Å	56Å	73.4Å	112.5Å	149Å

GaAs/AlAs

G167	G171	G127
49.6Å	65.1Å	82.9Å

All the samples were undoped multiquantum well structures[1], the active region consisting of 60 GaAs wells, of nominally identical widths, separated by 136Å thick $Al_{0.36}Ga_{0.64}As$ or AlAs barriers which were then sandwiched between 1040Å thick $Al_{0.36}Ga_{0.64}As$ layers or AlAs. This region was separated from the semi-insulating <100> GaAs substrate by an undoped 2500Å GaAs buffer layer. The background doping was $2x10^{14}$ cm^{-3} p-type.

2.10.2 DB-samples: $In_{0.11}Ga_{0.89}As/GaAs$

DB849	DB847	DB918
40Å	80Å	30,60,100,200Å

These were grown by molecular beam epitaxy at GEC Hirst Research Centre, Wembley. There were three samples in total with well widths that shown in the table above. Two were single quantum well structures (DB849 a 40Å well and DB847 a 80Å well) the other consisted of four individual single quantum wells (DB918 made up of single 30, 60, 100 and 200Å wells). In DB918 the four single undoped wells were separated by a 300Å GaAs barrier. The active region was grown onto a 300Å GaAs barrier on the side of the 200Å well with this barrier separated from the n-type GaAs substrate by a 0.5μ GaAs buffer layer. The outer well (the 30Å well) was capped by another 300Å GaAs layer. The other DB samples were simply an InGaAs well sandwiched between 0.5μ GaAs layers, all grown on a semi-insulating GaAs substrate.

It was noted that a study for sample specification by the growers showed no sign of the 200Å QW photoluminescence in DB918 and indeed we were only able to detect and make measurements in the 30Å well.

2.10.3 DB35(M1)

DB35(M1) was an electrically biased sample and was grown by a team at GEC Hirst Research Centre again using MBE. This sample was similar to DB918 in that it consisted of four single quantum wells, all undoped, each separated, in this case, by a 340Å $Al_{0.3}Ga_{0.7}As$ barrier. The substrate was also n-type. The well widths were nominally 50Å, 100Å, 200Å and 800Å. Our studies concentrated on the narrowest well which was shown to have the width 57.5Å. The active region was grown onto an 800Å $Al_{0.3}Ga_{0.7}As$ barrier on the side of the 800Å well with this barrier separated from the n-type substrate by again a 0.5μ GaAs buffer layer. As above, the outer well (in this case the 57.5Å well) was capped by a further 340Å $Al_{0.3}Ga_{0.7}As$ barrier, but now also has a 1000Å layer of 90% transparent $InSnO_2$ on top of this. The doping in the substrate was in this case $10^{18}cm^{-3}$ and in the active region there was an unintentional doping of $\approx 3x10^{14}cm^{-3}$ p-type.

The $InSnO_2$ acted as both an antireflection coating (thus increasing luminescence intensities) and as the electrical contact, the interface of the indium tin oxide layer forming a Schottky barrier with the $Al_{0.3}Ga_{0.7}As$ at one end. With indium solder alloyed onto the substrate this made an ohmic contact and so the sample could then act like a rectifier enabling a reverse bias to be applied without a significant current flow. For forward bias, up to $2x10^{11}cm^{-2}$ electrons were injected into the wells and for reverse bias up to $1x10^{11}$ heavy-holes. The injection appeared to be a quasi-resonant process giving appreciable carrier concentrations only for restricted ranges of bias.

2.10.4 The modulation doped NU samples

NU590	NU535	NU211
51Å	68Å	102Å

The samples were single side modulation doped single $GaAs/Al_{0.33}Ga_{0.67}As$ QWs, grown at Nottingham University by MBE. In these wells the carrier concentration could be varied to a small extent by illumination. The well widths of the three samples are shown above. The samples consisted of a semi-insulating substrate on top of which was grown a 2μ thick undoped GaAs layer and then a layer of undoped $Al_{0.33}Ga_{0.67}As$ 102Å wide. Next was grown 7 periods of 34Å wide undoped GaAs wells separated by 102Å undoped $Al_{0.33}Ga_{0.67}As$ barriers. This superlattice acted as a further buffer layer separating the 102Å (or 68Å or 51Å) GaAs well from the substrate and seemed to be essential for good photoluminescence. A barrier of undoped $Al_{0.33}Ga_{0.67}As$ 305Å thick separated the well from the doped $10^{18}cm^{-3}$ n-doped $Al_{0.33}Ga_{0.67}As$ region which was then capped with 254Å of undoped GaAs which was grown thick enough to allow good electrical contact to be made if needed, but thin enough to ensure no parallel conduction in the AlGaAs layer took place.

More information and further characteristics of these samples can be found in references 2 and 3.

2.11 References

1 Measurements of "Material" Parameters in Multi-Quantum Well Structures	J.W.Orton, P.F.Fewester, J.P.Gowers, P.Dawson, K.J.Moore, P.J.Dobson, C.J.Curling, C.T.Foxon, K.Woodbridge, G.Duggan, H.I.Ralph	Semicond.Sci.Technol. 2(1987)597
2 Observation of the Fractional Quantum Hall Effect in GaAs-(Ga,Al)As Quantum Well Structures	C.J.G.M.Langerak, C.V.Brown, P.C.Main, L.Eaves, C.R.H.White, T.J.Foster, M.Henini, P.A.A.Teunissen, J.A.A.J.Perenboom	Pre-print
3 Electroluminescence Investigations of Electron and Hole Resonant Tunneling in *p-i-n* Double-Barrier Structures	C.R.H.White, H.B.Evans, L.Eaves, P.M.Martin, M.Henini, G.Hill, M.A.Pate	Phys.Rev.B 45(1992)

3 Exciton, Heavy-Hole and Electron g-factors in Type I GaAs/Al$_x$Ga$_{1-x}$As, In$_x$Ga$_{1-x}$As/GaAs Quantum Wells.

3.1 Summary

The Zeeman splitting of the luminescence line in a series of type I GaAs/Al$_x$Ga$_{1-x}$As undoped multiquantum wells, in two In$_x$Ga$_{1-x}$As/GaAs multiquantum wells and in a single undoped In$_x$Ga$_{1-x}$As/GaAs well was measured as a function of applied magnetic field and well width. The low field Zeeman splitting was used to calculate the excitonic g-factor for both these systems. For the GaAs/Al$_x$Ga$_{1-x}$As system, this was coupled with our previously published values for the electron g-factor[1,2,3] to obtain a full picture of the variation in magnitude and sign of the exciton, electron and hole g-factor. For the In$_x$Ga$_{1-x}$As/GaAs quantum well theoretical predictions of electron g-factors were made firstly using 3-band *k.p* perturbation theory[4,5] then secondly an analytical theory based on both *k.p* theory and solid state elastic theory[6]. The modification to *k.p* theory in the latter case was designed specifically to account for the effect which the strain induced lattice deformation present in the In$_x$Ga$_{1-x}$As/GaAs system has on the band parameters. These prediction were then combined with the measured exciton g-factors to give a prediction of the heavy-hole g-factor characteristics in these type I In$_x$Ga$_{1-x}$As/GaAs systems.

For both the GaAs/Al$_x$Ga$_{1-x}$As and the In$_x$Ga$_{1-x}$As/GaAs systems as the field strength was increased, we observed that the overall trend of the Zeeman splitting deviated increasingly from the linear trend exhibited at low field. In some cases this lead to a sign reversal of the difference between the two heavy-hole spin components. This high field nonlinearity was attributed to field induced mixing of the heavy and light-hole states from higher quantum well subbands[7]. In some samples the apparent Zeeman splitting showed oscillatory behaviour as a function of field. This has been found to be caused by level anticrossings amongst the heavy-hole exciton states resulting from zero-field exchange splittings. The oscillatory behaviour reduces the reliability of determination of the g-factor

for these samples. However in chapter 4 we describe measurements of level-crossing signals in polarised luminescence which gives the exchange interaction.

3.2 General Background

Knowledge of the magnetic g-factors is of great importance when it comes to understanding the subband structure in quantum wells since it depends on the band structure in a very similar manner to the effective mass. It also governs the "spin splittings" in a magnetic field of the electron, hole and exciton states and so is relevant for many phenomena such as the quantum Hall effects, magneto-optical polarisation measurements (chapter 4) and electron-nuclear spin coupling[8].

Previous work has concentrated on magnetic g-factors in bulk semiconductors and in the narrow indirect gap type II GaAs/AlGaAs quantum well systems measured using magnetic resonance methods. However the short excitonic recombination time (approx. 10^{-9}-10^{-10} seconds)[9,10] is the limiting factor preventing the application of spin-resonance techniques to excitons in type I QW samples. Measurements of the excitonic g-factor have successfully been made in individual type I structures using quantum beat techniques[11], hole burning[12] and measurements of the Zeeman splitting of the luminescence line[7]. The former two techniques, although quite precise and to a large extent unaffected by inhomogeneous broadening have not been applied to a sufficient range of samples to give useful information. The difficulty, in obtaining the excitonic g-factor from the Zeeman splitting of the luminescence line is that in type I wells this splitting is very small compared to the inhomogeneous line broadening and so great care must be taken to enable conventional spectroscopic methods to be successful. The present measurements using this method are the first attempt at a systematic study of g-values over the complete range of well widths.

The type II structures on the other hand, lend themselves well to a variety of detection methods, most prominently optically detected magnetic resonance, ODMR, where a change in the intensity or polarisation of the luminescence at resonance is monitored. It is the long lifetime of the excited state (typically a few tenths of a microsecond) resulting from the spatial separation of the confined electron and hole that makes ODMR possible in these structures.

ODMR has lent itself successfully to obtain the electron Lande g-factor[13-15] and heavy-hole g-factor[13,16,17] as a function of well width up to 30Å in three different type II quantum wells. The exchange interactions, again in type II wells[13,14,17,18], have been measured using this technique and also using quantum beat (QB) emission[18] from which the zero field exchange interaction in type II QWs has been measured.

Over a wide range of quantum well widths, we have measured the excitonic g-factor from the magnetic field dependence of the Zeeman splitting in type I GaAs/AlGaAs QWs. From a comparison of the other evidence available for electrons, heavy holes and exciton g-factors from other techniques, together with our measurements of the excitonic g-factor, a full picture of the form of the three g-factors in these type I systems has been established.

Our results for the strained layers we believe are the first experimental investigation by any technique of the hole and excitonic g-factors in such systems. As detailed in chapter 1, these strained layer structures (SLS) not only experience a reduction in crystal symmetry due to quantum confinement, but also internal strain in the system manifests itself by a lattice deformation producing a secondary perturbation on the Hamiltonian of the system. This creates a mixing of the valence band states[19] and appears to produce a relatively large strain-induced change in the effective excitonic g-factor.

The SLS structure we have studied here is $In_{0.11}Ga_{0.89}As/GaAs$. This is one of the more interesting forms of SLS in that its structure is dependent on Indium composition. It has been shown, that for Indium composition around 15% the band configuration is of a mixed type, with the electron-heavy hole transition of type I and light hole of type II. For smaller Indium fractions though, both systems become of type I.

We have measured the excitonic g-factor for three different type I SLS quantum wells. From the analytical theory based upon solid state elastic theory and *k.p* band theory[6] we were able to calculate the well width dependence of the electron g-factor and hence determine the sign and trend of the hole g-factor as a function of well width.

3.3 Theoretical Background

Quantisation of carrier motion within a quantum well takes place under the application of an external magnetic field.This results in quantisation of the energy spectrum for motion normal to the field of both electrons and holes into a series of cyclotron orbits known as Landau levels. The energy of these quantised levels is dependent on whether the field is applied parallel to the plane of the well or to the growth axis (B_{xy} or B_z respectively) since motion parallel to the growth axis is already quantised due to quantum confinement. However there is a two fold Zeeman splitting of each Landau level due to spin which is to a first approximation, independent of field orientation. The two levels are separated in energy by

$$\Delta = g^{*}\mu_B B \qquad 3.1$$

where g^* is the appropriate g-factor, μ_B is the Bohr Magneton and B is strength of the magnetic field.

We have studied here not the individual electron and hole splitting but that of the coupled electron and hole or exciton. The two-fold Zeeman splitting in each Landau level then results in a four-fold splitting in the excitonic state in a quantum well.

To describe the Zeeman splitting of the exciton we must consider the Hamiltonians for electrons and holes and their coupling under the influence of a magnetic field. Van Kesteren et al[13] have formulated the Hamiltonian for an exciton in a type II GaAs/AlAs QW but since the form of the Hamiltonian is governed by axial symmetry, we can use their notation to describe the type I QW excitons also. As a first approximation van Kesteren considered the Hamiltonian for bulk excitons consisting of a ground state made up of an electron with spin $S_e={}^1/_2$ associated with a hole with $J_h={}^3/_2$ giving eight basis states. For bulk excitons, T_d is the relevant symmetry group and the Hamiltonian must be invariant under a co-ordinate transformation of this group.

The exciton Hamiltonian can be written

$$H_{ex} = H_e + H_h + H_{eh} \qquad 3.2$$

where H_e is the Zeeman Hamiltonian for the electron, H_h is the equivalent for holes and H_{eh} is the electron-hole spin-spin coupling. These are given by:

$$H_e = \mu_B g_e^{*} \sum_{i=x,y,z} S_{e,i} B_i \qquad 3.3$$

$$H_h = -2\mu_B \sum_{i=x,y,z} \left(\kappa J_{h,i} + q J_{h,i}^{3}\right) B_i \qquad 3.4$$

$$H_{eh} = -\sum_{i=x,y,z} \left(a J_{h,i} S_{e,i} + b J_{h,i}^{3} S_{e,i}\right) \qquad 3.5$$

In all of these expressions g_e^* is the conduction band Zeeman splitting constant and κ and q are the Luttinger Zeeman splitting constants for the valence band, a and b are the spin-spin coupling constants and S_e and J_h are the electron and hole spin operators.

Substituting equations 3.3-3.5 in 3.2 gives

$$H_{ex} = \mu_B \sum_{i=x,y,z} (g_e^* S_{e,i} - 2\kappa J_{h,i} - 2qJ_{h,i}^3)B_i - \sum_{i=x,y,z} (aJ_{h,i}S_{e,i} + bJ_{h,i}^3 S_{e,i}) \qquad 3.6$$

As detailed previously in chapter 1, in a quantum well, the ideal symmetry is D_{2d} in which the upper valence band is split into a light-hole band $J_{h,z}=\pm{}^1/_2$ and a heavy-hole band $J_{h,z}=\pm{}^3/_2$. Since the fine structure splittings described by H_{ex} are far smaller than the difference in subband energy for the light and heavy-holes, they can be treated separately. Also at low temperatures the hole occupies the heavy hole band, $J_{h,z}=\pm{}^3/_2$ and this reduces the relevant basis of states to four. The heavy hole submatrices now have the property that $\hat{J}_{h,x}=\hat{J}_{h,y}=0$ and $\hat{J}_{h,z}={}^4/_9\hat{J}_{h,z}{}^3$, and for D_{2d} symmetry $(S_{e,x},S_{e,y})$, $(\hat{J}_{h,x}{}^3,\hat{J}_{h,y}{}^3)$, (B_x,B_y) all belong to the Γ_5 representation and $S_{e,z}$, $\hat{J}_{h,z}{}^3$, B_z all to the Γ_2 representation. H_{ex} can then be written as

$$H_{ex} = \sum_{i=x,y} [\mu_B(g_{e,i}{}^* S_{e,i} - 2q_i J_{h,i}{}^3)B_i - b_i J_{h,i}{}^3 S_{e,i}]$$

$$+ \mu_B[g_{e,z}{}^* S_{e,z} - (\frac{8}{9}\kappa_Z + 2q_Z)J_{h,z}{}^3]B_z - (\frac{4}{9}a_z + b_z)S_{e,z}J_{h,z}^3 \qquad 3.7$$

with $g_{e,x}{}^*=g_{e,y}{}^*$, $q_x=q_y$, and $b_x=b_y$. Since we are dealing only with the heavy-hole band we can assign an effective heavy-hole spin of $\delta_{h,z}=\pm{}^1/_2$ for the corresponding $J_{h,z}=\pm{}^3/_2$ hole states. So 3.7 can be written in the form

$$H_{ex} = \sum_{i=x,y,z} [\mu_b(g_{e,i}{}^* S_{e,i} - g_{h,i}{}^* \delta_{h,i})B_i - c_i S_{e,i}\delta_{h,i}] \qquad 3.8$$

with

$$g_{h,x}{}^*=3q_x, \quad g_{h,y}{}^*=-3q_y, \quad g_{h,z}{}^*=6\kappa_z+13.5q_z,$$

$$c_x=1.5b_x, \quad c_y=-1.5b_y, \quad c_z=3a_z+6.75b_z,$$

operating in the basis of states $|m_\delta,m_s\rangle$:

$$\Psi_1 = |-\frac{1}{2},+\frac{1}{2}\rangle \quad \Psi_2 = |+\frac{1}{2},-\frac{1}{2}\rangle \quad \Psi_3 = |-\frac{1}{2},-\frac{1}{2}\rangle \quad \Psi_4 = |+\frac{1}{2},+\frac{1}{2}\rangle \qquad 3.9$$

For D_{2d} symmetry $g_{h,x}{}^*=-g_{h,y}{}^*$ and $c_x=-c_y$ giving the levels shown in the insert to

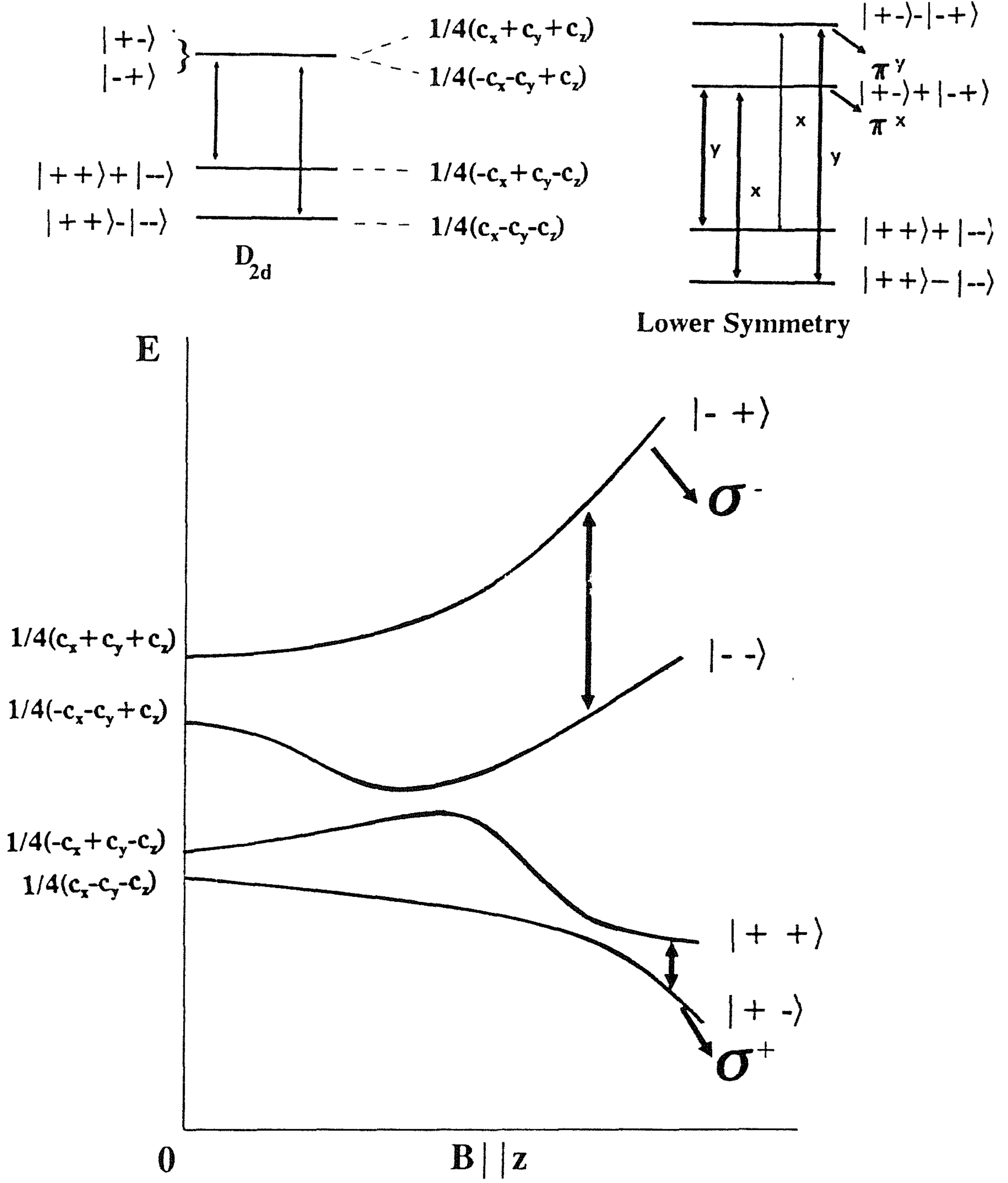

Figure 3.1 Energy level diagram for the heavy-hole excitons. The arrows indicate both the effective population changes and the two allowed microwave transitions. These transitions correspond to spin flips and connect a nonemitting level with an emitting one. The energy levels are given by

$$\pm\left[\frac{1}{4}\mu_B^2B_Z^2(g_e+g_h)^2+\frac{1}{16}(c_x+c_y)^2\right]^{\frac{1}{2}}+\frac{1}{2}c_z \qquad 3.10$$

and

$$\pm\left[\frac{1}{4}\mu_B^2B_Z^2(g_e-g_h)^2+\frac{1}{16}(c_x-c_y)^2\right]^{\frac{1}{2}}-\frac{1}{2}c_z \qquad 3.11$$

Eqn.3.10 is the magnetic field dependence of the optically allowed levels and 3.11 that of the forbidden levels. Along the top of the diagram are shown the zero field energy levels and the allowed microwave transitions for excitons in D_{2d} and in the lower symmetry C_{2v}.

figure 3.1 with the levels |+3/2,-1/2> and |-3/2,+1/2> degenerate. However van Kesteren[13] observed four zero field resonance lines in ODMR rather than three, implying that the lower symmetry group C_{2v} applied to the type II QW. In this case, the 4-fold axial symmetry along the z-axis is removed and $S_{e,x}$, $S_{e,y}$, $S_{e,z}$, $J_{h,i}$, B_i all belong to different representations. The allowed microwave transitions for both symmetry groups are shown in the insert of figure 3.1.

Figure 3.1 shows the predicted Zeeman splitting for the lower symmetry case C_{2V}. We see the degeneracy of the doublet $\Psi_{1,2}$ normally present in zero field in D_{2d} symmetry is removed. In a field applied parallel to the z axis there are splittings of the doublets $\Psi_{1,2}$ and $\Psi_{3,4}$ proportional to the sum and difference of the electron and hole g-factor. Electric dipole-allowed recombination only occurs from the spin reversed states $|\pm{}^3/_2, \mp{}^1/_2>$ with emission of σ^+ and σ^- circularly polarised photons propagating along z. $|\pm{}^3/_2, \pm{}^1/_2>$ are nonradiative states. Thus in sufficiently high field that the Zeeman splitting exceeds the exchange terms we expect a Zeeman splitting of the heavy-hole excitonic emission with g-factor

$$g_{ex} = g_e + g_h \qquad 3.12$$

The anticrossing behaviour of the levels indicated in figure 3.1 is to be expected as a result of residual small interactions not included in H_{ex} (equation 3.8). We shall see (section 3.5.2) that the anticrossing can interfere with measurements of the Zeeman splitting, particularly where the exchange splitting c_z is relatively large.

The above analysis however, concentrates only on the four heavy-hole exciton states and predicts linear Zeeman splittings for high fields. As mentioned in section 3.1 the measured splittings are non-linear in high fields. This is believed to be due to admixture of this manifold to other excitonic states by the field. The effect can be seen as giving a field-dependence to the g-values.

3.4 Experiment

The main difficulty in measuring the Zeeman splitting is that it is small compared to the inhomogeneous broadening. The two components have opposite polarisations so can be detected separately but careful analysis is needed to obtain a precise value of their energy separation.

3.4.1 Procedure

Preliminary work by M.J.Snelling[1], showed the best method for detecting the Zeeman splitting was from photoluminescence spectra rather from photoluminescence excitation spectra. In the latter case it is only possible to use data from splittings on the high energy side of the heavy-hole absorption peak because of the proximity of the luminescence detection energy to the absorption. The experimental set up described in chapter 2, diag.2.1 was slightly modified to that shown in figure 3.2.

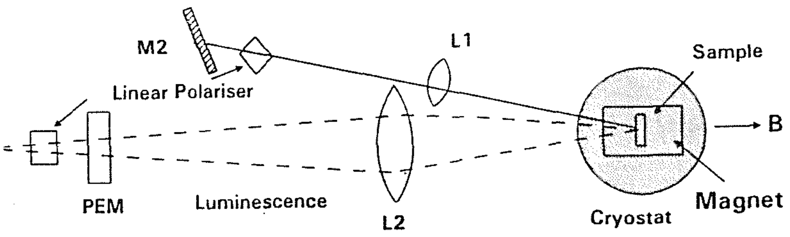

Figure 3.2 The modification to the experimental arrangement of chapter 2

The samples were the GaAs/AlGaAs G samples and the InGaAs/GaAs DB samples described previously (section 2.10.1).

The PL measurements were made using the Spectra Physics Ar^+ ion laser pumping either the Oxford University Coherent CR599 dye laser copy or the Spectra Physics 3900S Ti:Sapphire laser. The excitation energy was set well above the electron-hole continuum edge and the beam was linear rather than circular polarised before hitting the sample. This ensured excitation of equal proportions of spin-up and spin-down electron-hole pairs and subsequent thermalisation would result in near equal populations in each of the four $n=1$ excitonic states. The recombination from the Zeeman split levels was σ^+ and σ^- circularly polarised which then could be detected separately by the combination of PEM and linear polariser. The raw experimental data thus consisted of simultaneously recorded σ^+ and σ^- emission lines at various values of applied field, parallel to the growth axis, up to 8T.

As the field was increased the components generally showed a progressive splitting, much less than their width an example of a large splitting is shown in figure 3.3. In addition each showed an increase in luminescence energy with magnetic field due to the rising energy of the ground state Landau levels. At high fields the intensities of the luminescence components became unequal as a result of the different thermal populations of the Zeeman levels.

3.4.2 Analysis

The following method developed by M.J.Snelling[1] was adopted for extracting the Zeeman splitting from the raw luminescence spectra. It is a technique which effectively gives the difference of the first moments of the two components. First the components were normalised to the same peak height - an example of which is shown in figure 3.3. Secondly various high order polynomials, between order 7 and 13, were fitted by the method of least squares to one component of the Pl to determine that order which fitted best to the spectrum without introducing any spurious structure. The same order polynomial was then fitted to the data points of both components at once, with a series of different relative displacements between the two components. The mean square error of this was found to pass through a minimum as a function of displacement and the corresponding value of displacement was taken to be the Zeeman splitting (figure 3.4).

The reliability of the results was dependent on two main factors one statistical the other systematic. Firstly the statistical error, which included the accuracy associated with the best fit of the chosen polynomial, and ultimately tended to the statistical uncertainty in the first moment associated with a particular measurement: $\Gamma/\sqrt{N}$ where N is the total photon count in one component and Γ is the HWHM. This statistical error is indicated in the example of figure 3.4. Secondly, and most importantly, systematic error arose because the luminescence line shape varied with excitation energy and position on the wafer. This was assumed to be due to well width fluctuations and was especially prominent in the InGaAs/GaAs samples which showed quite significant changes from run to run. This resulted in a smooth variation of the Zeeman splitting for a given run but with variations of the order ±0.005 to ±0.01meV from run to run in the case of the GaAs/AlGaAs samples and from ±0.01meV to ±0.025meV for the InGaAs/GaAs QWs. Figures 3.5 and 3.6 give examples.

The statistical errors were reduced as far as possible by increasing the counting time, sometimes to as long as 100 seconds per point. The systematic errors were also reduced by taking several runs, the Zeeman splitting was then taken as the average.

DB918, the InGaAs/GaAs QW containing three individual wells only showed luminescence from the 30Å well.

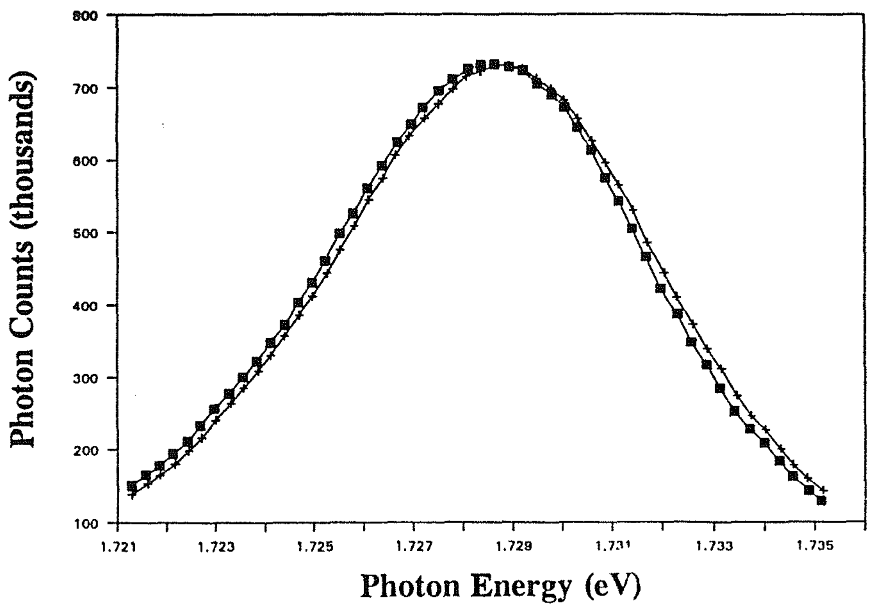

Figure 3.3 Normalised Components of the Zeeman splitting for a typical well studied. The curves are the best fit polynomial of degree 11 to each component

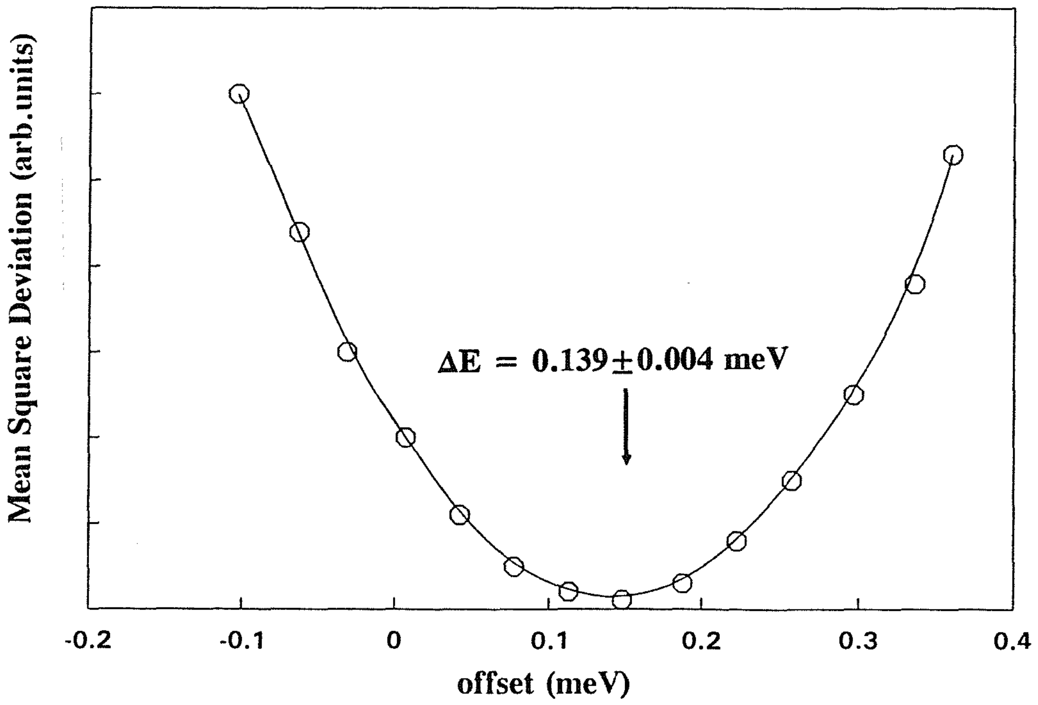

Figure 3.4 Variation with relative energy offset of the mean square deviation for the fit to both components at once for the data in fig.3.3

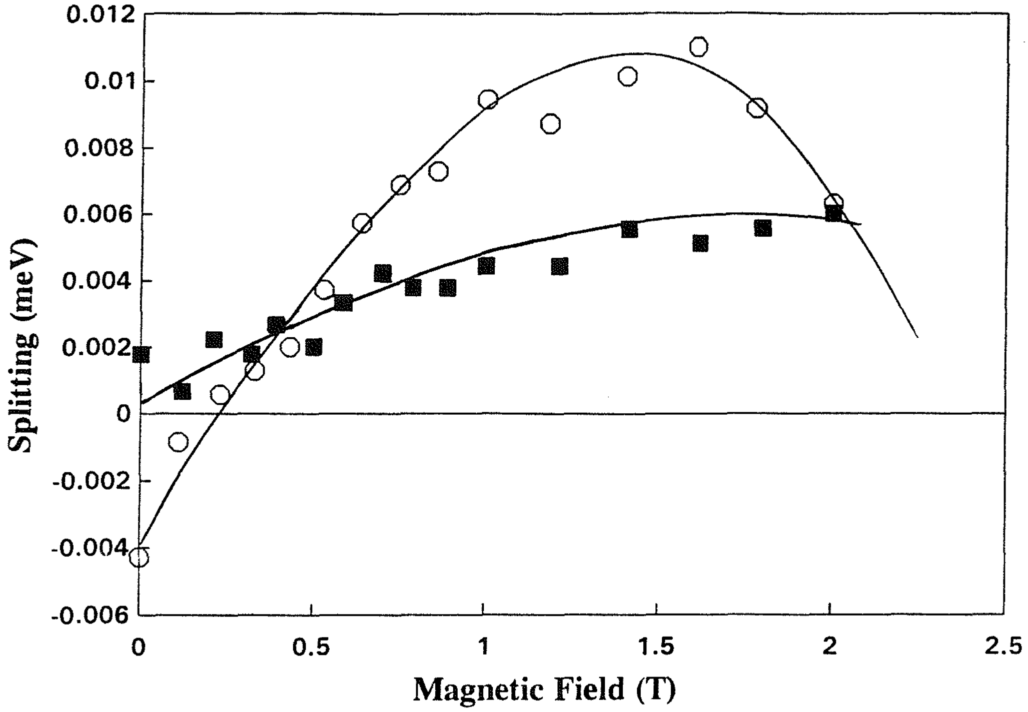

Figure 3.5 An example of the variation from successive runs of the measured Zeeman splitting. This specific example is for G55 the 112.5Å GaAs/AlGaAs sample.

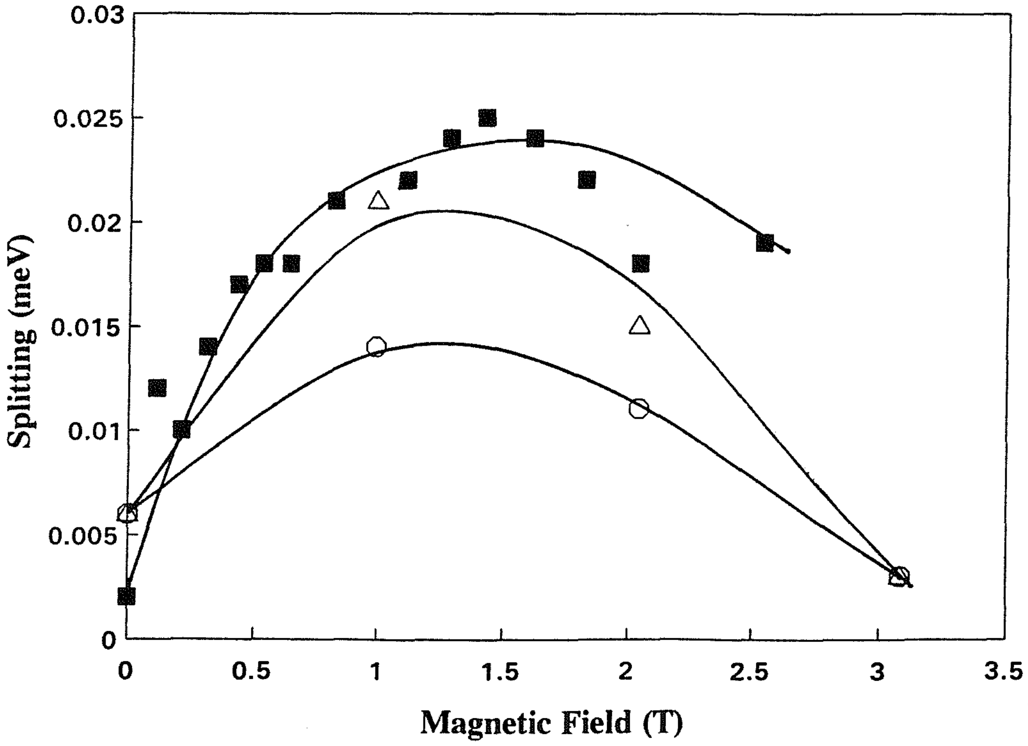

Figure 3.6 As above but this time for the DB849 the 40Å InGaAs/GaAs sample

3.5 Results and Interpretation

Figures 3.7 and 3.8 show the measured Zeeman splittings for all well widths studied in both the G samples GaAs/AlGaAs and the DB samples InGaAs/GaAs. The splittings are approximately linear, up to around 2T in the case of the G samples and to approximately 1T for the DB samples. For higher fields, the splittings then deviate from the linear variation. Our primary interest is in the g-values obtained from the low field data. However we discuss the high and low field regions in turn.

3.5.1 High field region:

The non-linearity at the high fields is particularly marked in the case of the wider GaAs/AlGaAs wells where there is a sign reversal in the splittings for L_z greater than 75Å, but is also prominent in the narrower InGaAs/GaAs wells. Ossau et al[7] have observed similar behaviour in a number of GaAs/AlGaAs MQWs with a specific example given for a 180Å well showing a small non-linear splitting for the heavy hole exciton with a sign reversal at around 3T. Ossau concluded that these non-linear splittings are a consequence of field induced mixing of the heavy and light-hole states from higher quantum well subbands, the apparent increase in non-linearity with well width is a result of the eigenstates of the quantum well coming closer together as quantum confinement is reduced. Bauer and Ando[20] and Bauer[21] calculate the properties of magneto-excitons using an effective mass approximation and Luttinger Hamiltonian derived from the bulk case. They too predict a splitting of the heavy-hole exciton which changes sign at intermediate fields.

The InGaAs/GaAs samples exhibit a trend in the splitting at high fields reminiscent of that seen in the wider well GaAs/AlGaAs samples although the change in sign occurs at larger field values. The overall splittings are larger but the initial gradients are less. A comparison of a GaAs/AlGaAs sample of well width L_z=149Å with the smallest InGaAs/GaAs well studied, L_z=30Å, shows that the splittings measured were comparable in magnitude. This is shown in figure 3.9.

The high field nonlinearity in the GaAs/AlGaAs wells appears to be mainly a consequence of the changes with L_z of the energy separation of the states coupled by the field, the field induced matrix elements being roughly independent of L_z. When we examine the high field nonlinearities in the InGaAs/GaAs wells it is clear that the situation is more complicated. Calculations from the transition energies in GaAs/AlGaAs for $x=0.3$ and $In_xGa_{1-x}As$/GaAs for $x=0.11$, using data from Ref.22, 23 and Ref.24 respectively,

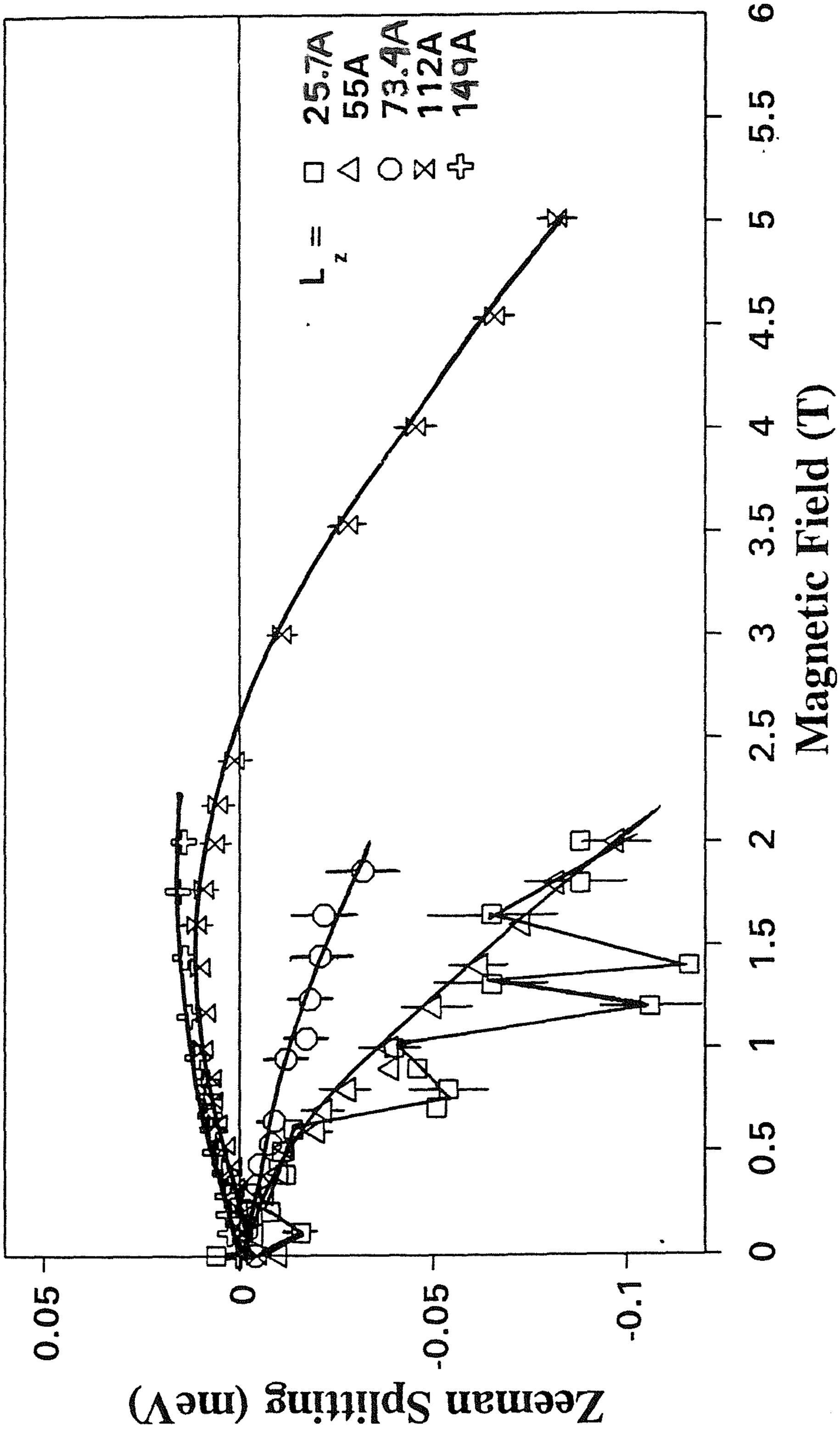

Figure 3.7 The measured Zeeman splitting for the GaAs/AlGaAs samples.

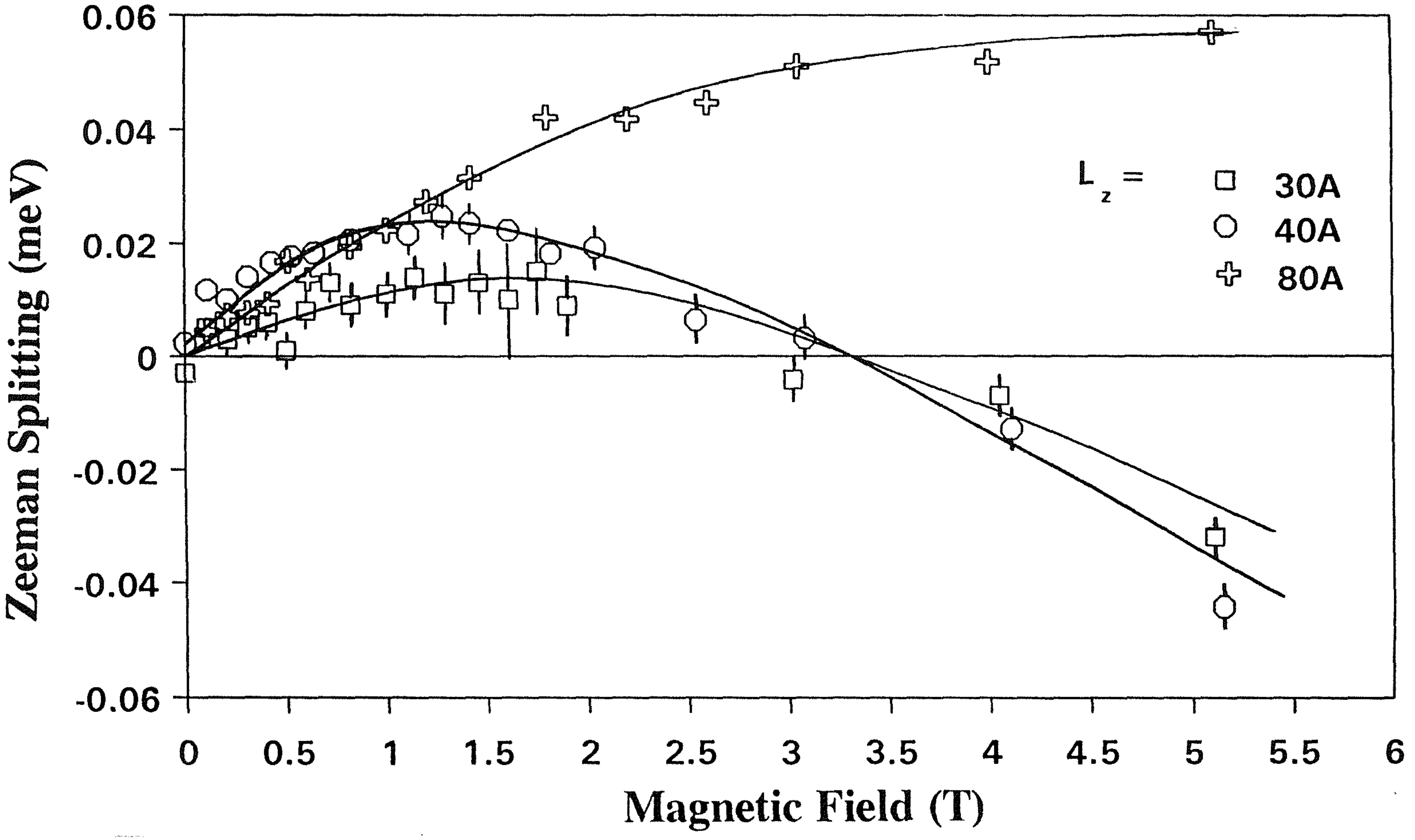

Figure 3.8 The measured Zeeman spliting for the InGaAs/GaAs samples.

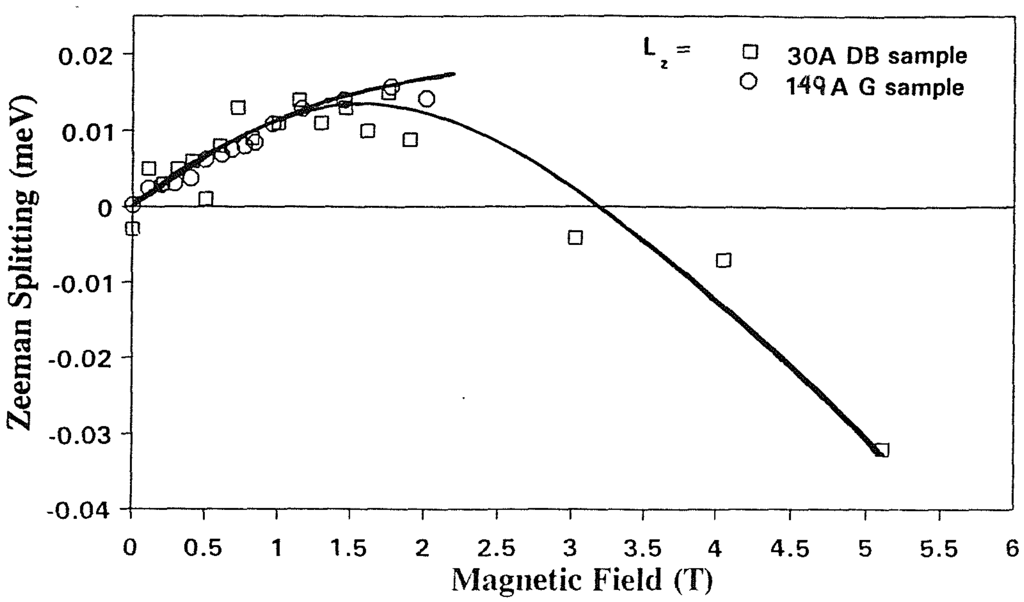

Figure 3.9 Comparison of the spin-splitting of DB918, the 30Å InGaAs/GaAs well with that of G52, the 149Å GaAs/AlGaAs well.

show that the confined states in both systems are comparable in separation but despite this the nonlinearity is more extreme in InGaAs/GaAs than in GaAs/AlGaAs systems, indicating larger field induced matrix elements. This suggests that the variation of strain with well width may have a significant effect. A complete understanding of this behaviour would require additional measurements and a more complicated theoretical analysis than that of Bauer.

3.5.2 The low field linear region:

The initial slope of the Zeeman splitting gives the values for the different samples of g_{ex}^* shown in figures 3.10 and 3.11. For the GaAs/AlGaAs samples we see the change of sign for L_z between 73.4Å and 112Å and the tendency of g_{ex}^* to a positive constant value at sufficiently wide wells. The sample with L_z=25.7Å exhibited large, reproducible oscillations in the low field Zeeman splitting (figure 3.12). These appear to be an artefact of the analysis when the line shape of one of the optically active states $\psi_{1,2}$ is perturbed as it crosses (or anticrosses) one of the optically inactive states $\psi_{3,4}$ (see figure 3.1). These level crossings have been studied in detail in chapter.4 and have revealed that a level crossing corresponds to a pronounced minimum in the magnitude of the apparent Zeeman splitting. In this case, the oscillations in the splitting prevent an accurate evaluation of the g-factor but, to

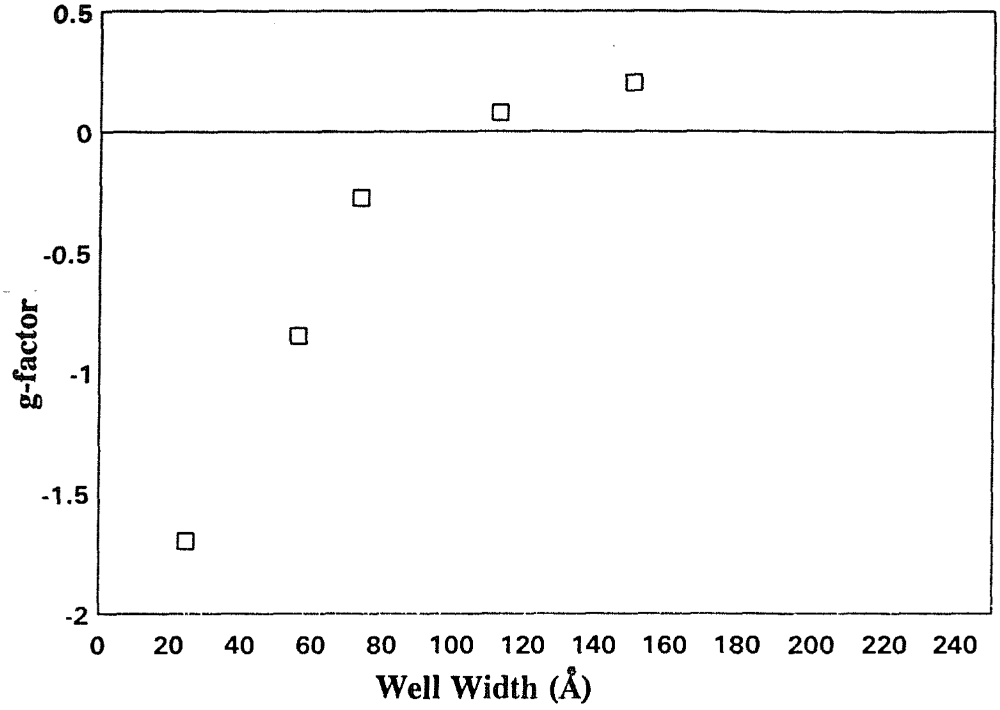

Figure 3.10 The measured effective excitonic g-factor for the GaAS/AlGaAs QW's as a function of well width.

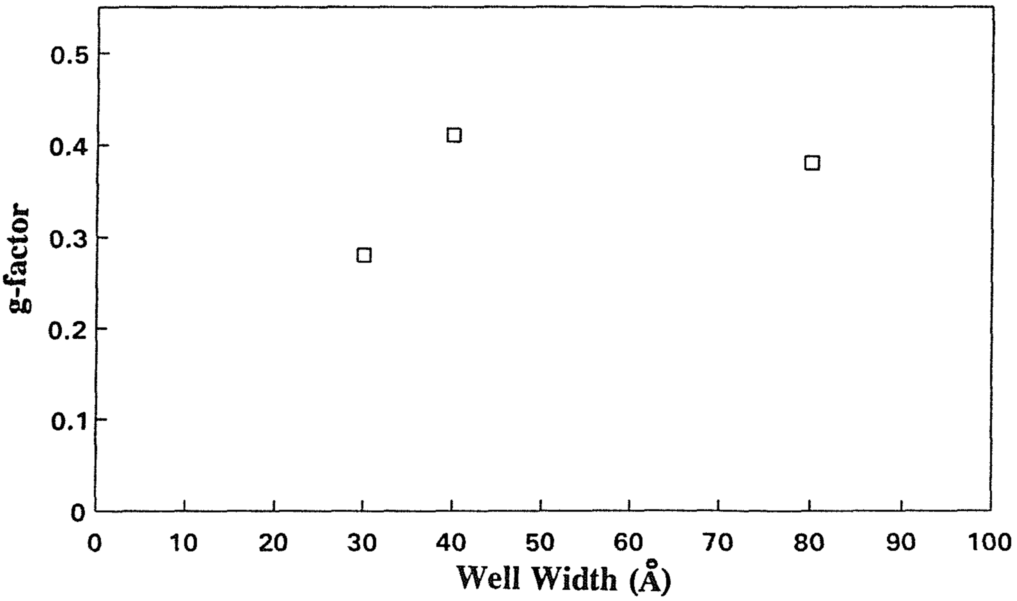

Figure 3.11 The measured effective excitonic g-factor for the InGaAs/GaAs samples as a function of well width.

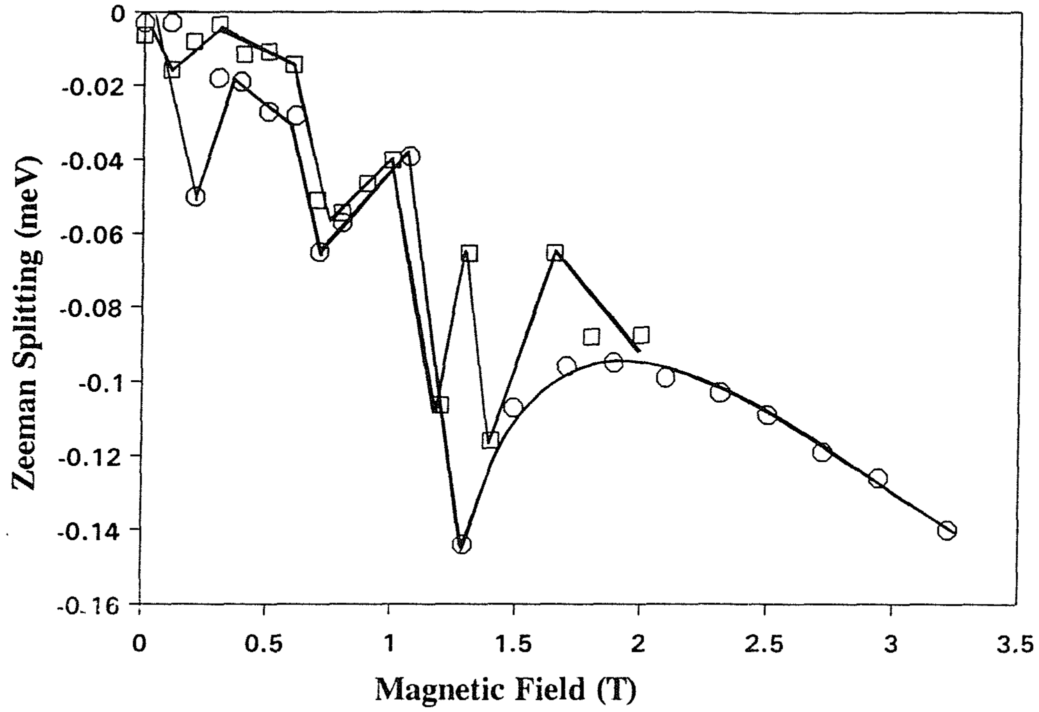

Figure 3.12 Oscillations in the measured Zeeman splitting for the 22Å GaAs/AlGaAs well.

the extent that a level crossing leads to a minimum in the apparent splitting it seems reasonable to assume that the magnitude of g_{ex}^* is at the upper limit of the broad range indicated by the spread of points in figure 3.12. The level crossing measurements (see chapter 4) indicate that for well widths other than 25.7Å in GaAs/AlGaAs there are no crossings for fields less than 2T.

3.5.3 A review of the results for GaAs/AlGaAs:

Figure 3.13 shows the excitonic g-factors we have measured in the G-samples together with a combination of previously published work for g_{ex}^*, g_e^* and g_h^*. Ossau et al[7] have measured the Zeeman splitting in GaAs/$Al_{0.3}Ga_{0.7}As$ QWs at 1T and the values of g_{ex} obtained from these splittings are included here. The solid line is a guide to the eye through all these points.

The data for g_e^* are from previous measurements in our laboratory[1,2,3] of the Hanle effect and photoluminescence decay times in degenerate p-type GaAs/$Al_{0.3}Ga_{0.7}As$ SQWs. The Hanle effect has the advantage that for wells with a degenerate hole population the depolarisation of the luminescence is controlled by the Larmor precession of the photoexcited conduction electrons and hence, by g_e^*. This method determines both the

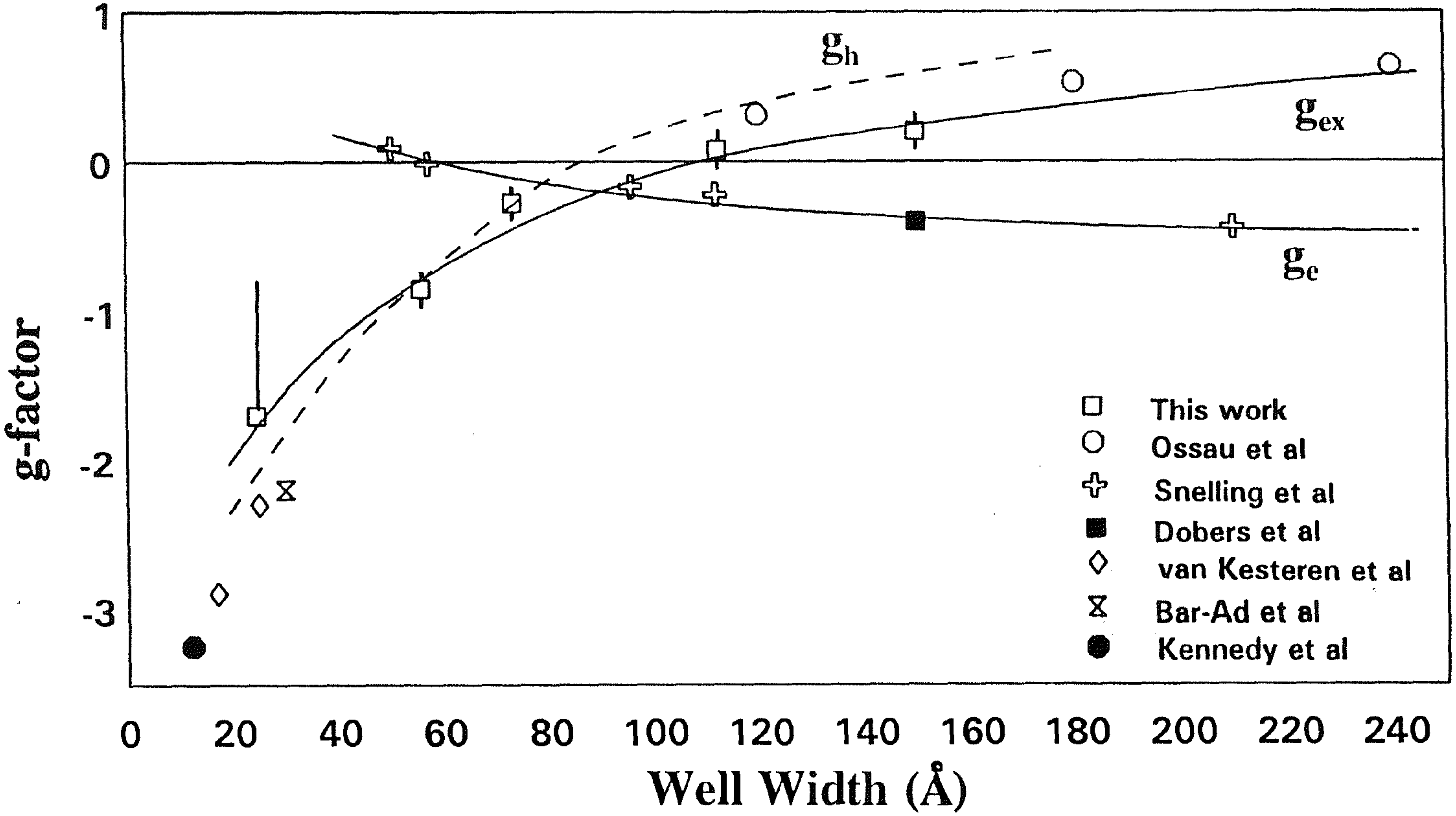

Figure 3.13 The measured experimental values of g_{ex}^* together with published values of g_e^* and g_h^* calculated from this data.

magnitude and sign of g_e^*. The electron g-factor will tend to the band edge bulk GaAs value, -0.44, for wide wells and to that for bulk AlGaAs, +0.4, for very narrow wells, the solid curve is a guide to the eye through the points and including these limits. The solid square is a measure of g_e^* from electrically detected spin resonance in a 150Å modulation doped n-type well[25]. It appears to confirm our observed trend for g_e^*.

As detailed previously (equ.3.12), the spin splitting of the exciton emission in a magnetic field parallel to the growth axis is governed by the g-factor of the optically active excitonic energy levels, which is equal to the sum of the individual effective heavy-hole and electron g-factors. By combining our measured values of g_e^* together with the those of g_{ex}^*, we obtain the heavy-hole effective g-factor (g_h^*) as a function of well width as shown by the dashed line in figure 3.13.

For comparison also shown are the data for g_h^* measured in Type II GaAs/AlGaAs QWs by van Kesteren et al[13] and Kennedy et al[16,17] by optically detected magnetic resonance methods. There is disagreement here over the sign of the measured heavy hole g-factor but our measurements seem to support the negative values found by van Kesteren. Considering the magnitude of the hole g-factors measured by both groups were larger than our measured values for the excitonic g-factors, this implied that g_h^* and g_e^* must have opposite signs and therefore g_h^* and g_{ex}^* are negative for these well widths. We would also expect the hole g-factor to be very similar in both type I and type II systems as in both cases the hole is confined in the GaAs region, any differences arising predominantly from confinement energy and band gap discontinuity differences between the two. Neither of these would be significant enough to alter the value of g_h^* to such an extent that the positive value of Kennedy could be assumed.

Additional support for our choice of sign comes from the determination of g_{ex}^* in a 30Å stepped type I GaAs/$Al_{0.1}Ga_{0.9}As$ MQW from quantum beat measurements[11]. The sign was not determined but the magnitude was greater than that of our value of g_{ex}^* for L_z=30Å. However the stepped nature of the quantum well bands has an important influence on the g-values. The most significant difference between the stepped well and the regular type I structure is likely to be in the characteristics of the electron g-factor, with the hole g-factor little affected. The reduced band offset gives a total electron confinement energy of 100meV, which corresponds approximately to that for a regular 50Å GaAs/AlGaAs well with Al= 0.3, in which $g_e^* \approx 0$. Hence, in the stepped well, g_{ex}^* is roughly equal to g_h^* which gives an estimate of $g_h^* \approx 2.2$ for L_z=30Å - a value close to our curve (bow in figure 3.13)

3.5.4 Analysis of the InGaAs/GaAs measurements:

To our knowledge, no published measurements exist of the electronic g-factor in SLS structures. Hendorfer and Schneider[6] have presented a theory of the effective g-factor of conduction electrons in such layers, which is an improvement over the simple *k.p* perturbation theory developed by Wallis[4] and re-examined by Hermann and Weisbuch[26]. In particular Hendorfer and Schneider[6] point out that the strain can introduce a pronounced anisotropy of g_e^* which is not described by *k.p* theory. For comparison we calculate g_e^* using both approaches but shall regard values calculated using the equations in Ref.6 as the more reliable.

It is generally understood that in *k.p* perturbation theory a simple 3-band approximation is sufficient for calculation of g-factors because of the cancellations in higher order terms[27]. We therefore use as a first approximation ignoring strain, the 3-band formulae of reference 5 with a modification that we use the measured value of band edge effective electronic g-factor (g_{e0}^*), rather than the band edge effective mass (m_{e0}^*), to fix the other parameters. The solution of 3.13 and 3.14 gives the relationship of g_e^* to the energy above the conduction band edge, E.

$$g_e^* = g_{e0}^* + 4K_1\frac{m_e}{m_{e0}^*}\frac{E_1}{E_g} \qquad 3.13$$

and

$$E = E_1 + K_2\frac{E_1^2}{E_g} \qquad 3.14$$

The constants K_1 and K_2 are given by:

$$K_1 = (1-x)\frac{(1-y)^2}{(2+x)^2}(2+\frac{3}{2}x+x^2) \qquad 3.15$$

$$K_2 = -\frac{(1+\frac{1}{2}x^2)}{(1+\frac{1}{2}x)}(1-y)^2 \qquad 3.16$$

with

$$x = \frac{1}{1+(\frac{\Delta_0}{E_g})} \qquad 3.17$$

$$y = \frac{1-x}{(1-x)+(2+x)(1-\frac{g_{e0}^*}{2})} \qquad 3.18$$

where Δ_0 is the Γ_5^v-Γ_7^v valence band spin orbit splitting of 0.354eV, E_g=1.367eV is the band gap energy, as shown in figure 3.14, g_0^*=-0.8 is the measured Lande g-factor[26] and m_{e0}^*/m_e=0.061 that of the effective mass ratio for bulk InGaAs[26]. These give the values K_1=0.09039 and K_2=-0.8498 and together with the electron confinement energies, E, we have measured for the $In_{0.11}Ga_{0.88}As$/GaAs samples from PLE spectra, we obtain the values of g_e^* listed in table 1 (see page 58). The effect of barrier penetration on the effective electronic g-factor have been estimated using a 5 band k.p perturbation theory[26] for the values of g_e^* in the GaAs barriers. This calculation was previously performed in GaAs/AlGaAs[1,2] and was shown to be small, and despite the enhancement which might have been expected due to lower barriers, the contribution in InGaAs/GaAs is also small.

Our second calculation including the effects of strain follows Hendorfer and Schneider's theory[6]. Assuming homogeneous strain in the epitaxial layer, the strain Hamiltonian, as developed by Bir and Pikus[28], was used to evaluate the influence of strain on the Γ_6 conduction band and the Γ_7 and Γ_8 valence bands at k=0.

$$H_\epsilon = -a_V(\epsilon_{xx} + \epsilon_{yy} + \epsilon_{zz}) - 3b(\epsilon_{zz} - \epsilon_{xx})(L_z^2 - \frac{1}{3}L^2) \qquad 3.19$$

where a_v and b are the deformation potentials of the valence bands for the hydrostatic component of the strain and the tetragonal distortion component along <001> respectively.

ϵ_{ij} are the strain tensor components defined as

$$\epsilon_{xx} = \epsilon_{yy} = \frac{(a_{bulk} - a_{epi})}{a_{epi}} \qquad 3.20\ a$$

$$\epsilon_{zz} = -2(\frac{C_{12}}{C_{11}})\epsilon_{xx} \qquad 3.20\ b$$

and for i≠j

$$\epsilon_{ij} = 0 \qquad 3.20\ c$$

a_{bulk}, a_{epi} are the lattice constants of the bulk material and the epitaxial layer and C_{ij} the elastic stiffness constant which takes values $C_{ij} = C_{11}$ for i=j and C_{12} for i≠j.

Diagonalization of H_ϵ yields three states, as expected: the doubly degenerate heavy-hole, light-hole and split off bands, represented by $|^3/_2,\pm^3/_2>$, $|^3/_2,\pm^1/_2>$ and $|^1/_2,\pm^1/_2>$

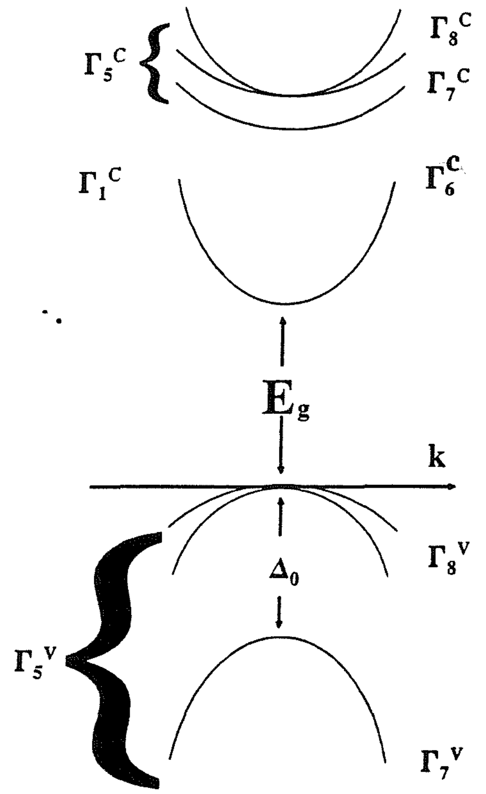

Figure 3.14 Band structure of a typical bulk cubic sample with T_d symmetry.

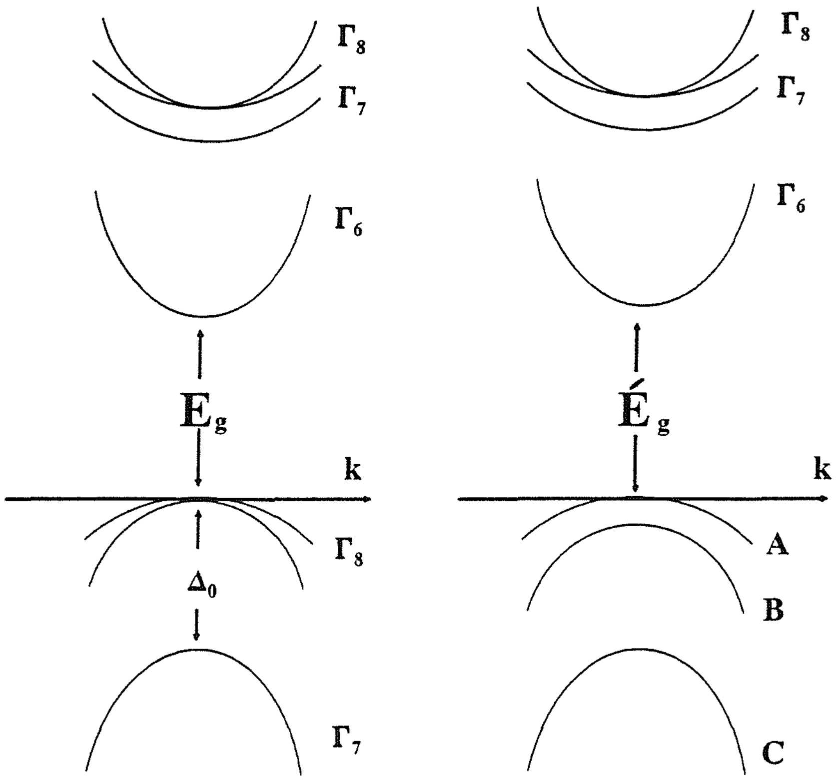

Figure 3.15 Band structure of materials with T_d symmetry (a) for the bulk case and (b) for strained layers under tensile strain.

respectively. Expressions for the energy differences between the conduction band and all three valence bands A, B and C are given approximately by

$$E_A = \acute{E}_g + \frac{1}{2}\delta\varepsilon_{001} + \varepsilon \qquad 3.21\ a$$

$$E_B = \acute{E}_g - \frac{1}{2}\delta\varepsilon_{001} - \frac{\delta\varepsilon^2_{001}}{2\Delta} + \varepsilon \qquad 3.21\ b$$

$$E_C = \acute{E}_g + \frac{1}{2}\frac{\delta\varepsilon^2_{001}}{\Delta} + \Delta + \varepsilon \qquad 3.21\ c$$

where $E'_g = 1.367$eV is the energy gap of the strained structure, $\delta\varepsilon_{001}$, to first order, is the light to heavy-hole splitting and has been measured again from the characteristic PLE spectra of the DB samples in question. ε is the confinement energy of the quantum state, and Δ is the Γ_8 to Γ_7 valence band splitting 0.354eV. Figure 3.15 outlines the situation described above, showing both the band structure for typical T_d symmetry bulk sample (3.15a) and under the effect of uniaxial tensile strain (3.15b).

Using second order *k.p* perturbation theory to expand about the conduction band extrema in terms of the electron wavefunction, leads to an expression for the conduction band:

$$E^c(k) = E_g + \sum_{\alpha\beta} D_{\alpha\beta}k_\alpha k_\beta - \mu_B\sigma B g_0 \qquad 3.22$$

with

$$D_{\alpha\beta} = \frac{\hbar^2}{2}m_0\left(\delta_{\alpha\beta} + \frac{2}{m_0}\sum_i \frac{\langle c|p_\alpha|i\rangle\ \langle i|p_\beta|c\rangle}{\varepsilon_{CB} - \varepsilon_i}\right) \qquad 3.23$$

$|c\rangle$, $(|i\rangle)$ and $\epsilon_{CB}(\epsilon_i)$ denote the wavefunction and energy of the conduction band (and of other bands i) at $k=0$, μ_B is the Bohr magneton, $\hbar$ is Planck's constant divided by 2π, p_α is the α component of the momentum operator. The last term in (3.22) is the magnetic energy of the electron spin with $g_0=2$ the value for the free electron, whereas the second describes not only the magnetic energy due to orbital contributions but also the kinetic energy of the conduction electrons. For our purposes it is necessary to separate these out and this is achieved by splitting the tensor $D_{\alpha\beta}$ into its symmetric (D^S) and antisymmetric (D^A) components. Rewriting (3.22) gives

$$E^c(k) = E_g + \sum_\alpha D^S_{\alpha\alpha}k_\alpha k_\alpha + iD^A_{\alpha\beta}eB - \mu_B g_0\sigma B \qquad 3.24$$

Regarding (3.24) as a 2 x 2 matrix then, for the evaluation of g_e^*, the last two terms in (3.24) must be diagonalized and the resulting eigenvalues equated to $\pm 1/2 g_e^* \mu_B B$. This finally leads to the solution for the z component

$$\frac{g_z^*}{g_0} - 1 = -\frac{p^2}{3}\left[\left(\frac{3}{2E_A} - \frac{1}{2E_B} - \frac{1}{E_C}\right) - \alpha_0\left(\frac{1}{E_B} - \frac{1}{E_C}\right)\right] - \frac{\acute{p}^2}{3}\left(\frac{1}{E_7-\acute{E}_g} - \frac{1}{E_8-\acute{E}_g}\right) + \acute{C} \qquad 3.25$$

and for the x,y component

$$\frac{g_x^*}{g_0} = \frac{g_y^*}{g_0} = 1 - \frac{p^2}{3}\left[\left(\frac{1}{E_B} - \frac{1}{E_C}\right)\left(1 + \frac{\alpha_0}{2}\right)\right] - \frac{\acute{p}^2}{3}\left(\frac{1}{E_7-\acute{E}_g} - \frac{1}{E_8-\acute{E}_g}\right) + \acute{C} \qquad 3.26$$

Where p^2 and p'^2 denote the matrix elements for the conduction band-valence band coupling and the coupling of the Γ_6 conduction band with the Γ_7 and Γ_8 conduction bands of E_7 and E_8. $\alpha_0 = \delta\varepsilon_{001}/\Delta$ and C' is a constant introduced for optimal fit to the data but is taken to physically represent the residual influence of all the other remaining bands and has the magnitude -0.02 in a III-V semiconductor material.

Table 1

Well width Å	g_e^* *k.p* theory ○	$g_{e(z)}^*$ Strain modified theory ⊠	$g_{e(x,y)}^*$ Strain modified theory ✚
30	-0.783	**-0.119**	**-0.87**
40	-0.776	**-0.501**	**-0.587**
80	-0.692	**-0.242**	**-0.619**

The parameters p^2, p'^2, E_7 and E_8 are needed as a function of the alloy composition ie for $x=0.11$, and this is achieved by simple linear interpolation between the corresponding bulk values given in ref.6. Table 1 shows the calculated of $g_{e(z)}^*$ and $g_{e(x,y)}^*$ using this theory and for comparison, g_e^* calculated from *k.p* theory. Due to the orientation of the magnetic field $g_{e(z)}^*$ is the relevant parameter here but the trend of $g_{e(x,y)}^*$ is still of interest in these circumstances.

Figure 3.16 illustrates all these values of g_e^* together with our measured values of

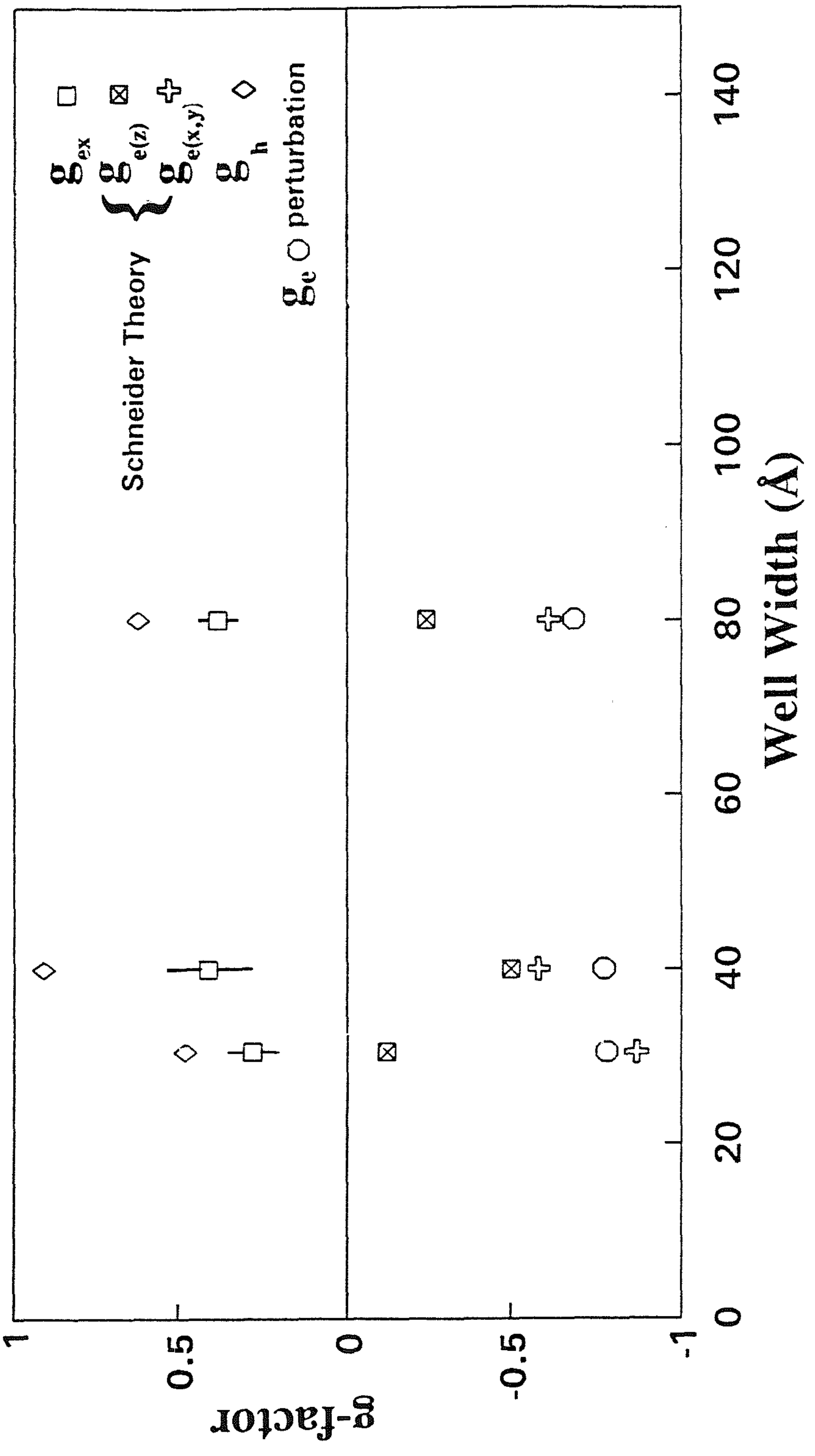

Figure 3.16 The experimental values of g_{ex}^*, g_e^* calculated from *k.p* theory and the strain modified theory[6], together with g_h^* calculated from this data

g_{ex}^* and the expected trend of g_h^* given by $g_{ex}^*-g_{e(z)}^*$.

We can see the extent to which internal strain influences the electronic parameters in the epitaxial layer by simple comparison of the g_e^* values calculated from *k.p* perturbation and those from the modified theory by Schneider et al[6]. *k.p* theory seems to break down especially in the wider well regime. Also comparison of the trends between g_{ex}^*, g_h^* and g_e^* in the DB samples and the G samples shows there is a close correlation between g_{ex}^* and g_h^* in the GaAs/AlGaAs samples but not so in the InGaAs/GaAs samples.

3.6 Conclusions

For the GaAs/$Al_xGa_{1-x}As$ quantum wells we have measured the effective excitonic g-factor and from measurements of the effective electron g-factor in these wells[1,2,3] we have calculated the effective hole g-factor in these samples. We have observed that both the excitonic and hole g-factor vary rapidly with well width and exhibit a change of sign at approximately 75Å but also agree satisfactorily with previous measurements of both quantities[7,13,14,16,17]. There is also good agreement of the measured values of g_e^*[1,2,3] with 3 band *k.p* theory recorded in references 1,2 and 3.

For the $In_xGa_{1-x}As$-GaAs quantum wells we have measured g_{ex}^* in three different quantum well widths, giving an indication of the well width dependence, and also we have calculated both $g_{e(z)}^*$ and $g_{e(x,y)}^*$. Although there are no direct measurements of g_e^* in InGaAs/GaAs wells, due to the consistency of the measured and theoretical g-values in GaAs/AlGaAs we can have some confidence in the values of g_h^* obtained for the InGaAs/GaAs wells. We thus have, for the first time, a picture of the variations with well width of the magnitude and sign of the carrier g-factors in two quantum well systems

What became most apparent from the theoretical analysis involved in this chapter was the inadequacy of any theoretical modelling of g-factors in the valence band of quantum wells. In comparison, the structure of the conduction band is reasonably well understood and its parameters can be modelled sufficiently using 3-band or higher *k.p* theory. Due to the complexity of the valence band, the well width dependence of κ and q offers an interesting challenge for future theoretical study.

3.7 References

1 Optical Orientation in Quantum Wells	M.J.Snelling	Thesis Southampton University(1991)
2 Optical Pumping and Optically Detected Nuclear Resonance	G.P.Flinn	Thesis Southampton University(1991)
3 Magnetic g-factor of Electrons in GaAs/AlGaAs Quantum Wells	M.J.Snelling, G.P.Flinn, A.S.Plaut, R.T.Harley, A.C.Tropper, R.Eccleston, C.C.Philips	Phys.Rev.B. 44(1991)11345
4 Infrared Cyclotron Resonance in InSb	E.D.Palik, G.S.Picus, S.Teitler, R.F.Wallis	Phys.Rev.122(1961)475
5 Tunnelling Cyclotron Resonance and the Renormalized Effective Mass in Semiconductor Barriers	G.Brozak, E.A.de Andrada e Silva, L.J.Sham, F.DeRosa, P.Miceli, S.A.Shwarz, J.P.Harbison, L.T.Florez, S.J.Allen.Jr.	Phys.Rev.Lett. 64(1990)471
6 g-factor and Effective Mass Anisotropies in Pseudomorphic Strained Layers	G.Hendorfer, J.Schneider	Semicond.Sci.Technol. 6(1991)595
7 Properties of Impurity States in Superlattice Semiconductors in "Magneto-optics of Excitons in GaAs/(GaAl)As"	W.Ossau, B.Jakel, E.Bangert, G.Weimann	NATO ASI Series (1988)285
8 Optically Detected Nuclear Magnetic Resonance of Nuclei within a Quantum Well	G.P.Flinn, R.T.Harley, M.J.Snelling, A.C.Tropper, T.M.Kerr	Semicond.Sci.Technol. 5(1990)533
9 Subpicosecond Spin Relaxation Dynamics of Excitons and Free Carriers in GaAs Quantum Wells	T.C.Damen, L.Vina, J.E.Cunningham, J.Shah	Phys.Rev.Lett 67(1991)3432
10 Luminescence Studies of Optically Pumped Quantum Wells in GaAs/Al_xGa_{1-x}As Multilayer Structures	R.C.Miller, D.A.Kleinman, W.A.Nordland,Jr, A.C.Gossard	Phys.Rev.B 22(1980)863
11 Absorption Quantum Beats of Magnetoexcitons in GaAs Heterostructures	S.Bar-Ad, I.Bar-Joseph	Phys.Rev.Lett. 66(1991)2491
12 Spin-Flip-Induced Hole Burning in GaAs Quantum Wells: Determination of Exciton Zeeman Splitting	H.Wang, M.Jiang, R.Merlin, D.G.Steel	Phys.Rev.Lett. 69(1992)804
13 Fine Structure of Excitons in Type-II GaAs/AlAs Quantum Wells	H.W.van Kesteren, E.C.Cosman, W.A.J.A.van der Poel, C.T.Foxon	Phys.Rev.B 42(1990)5283

14 Optically Detected Magnetic Resonance Study of a Type-II GaAs/AlAs Multiple Quantum Well	H.W.van Kesteren, E.C.Cosman, F.J.A.M.Greidanus, P.Dawson, K.J.Moore, C.T.Foxon	Phys.Rev.Lett.61(1988)12915
15 Order of the X-Conduction Band Valleys in Type II GaAs/AlAS Quantum Wells	H.W.van Kesteren, E.C.Cosman, F.J.A.M.Greidanus, P.Dawson, K.J.Moore, C.T.Foxon	Phys.Rev.B 39(1989)13426
16 Gallium Interstitials in GaAs/AlAs Quantum Wells	J.M.Trombetta, T.A.Kennedy, W.Tseng, D.Gammon	Phys.Rev.B. 43(1991)2458
17 Optically Detected Magnetic Resonance of Excitons and Shallow Donors in (GaAs)$_5$(AlAs)$_5$ Superlattices	J.M.Trombetta, T.Kennedy, G.Gammon, B.V.Shanabrok, S.M.Prokes	20th Int.Conf.Phys.Semic. Thessaloniki Greece (1990)
18 Quantum Beats in the Exciton Emission of Type II GaAs/AlAs Quantum Wells	W.A.J.Van der Poel, A.L.G.J.Severens,C.T.Foxon	Pre-print
19 Semiconductors and Semimetals vol 32: Strained Layer Superlattices: Physics	Thomas P.Pearsall	Willardson, Beer Academic Press
20 Theory of Magnetoexcitons in Quantum Wells	G.E.W. Bauer, T.Ando	Phys.Rev.B 37(1988)3130
21 Mixing of Magnetoexcitons in Quantum Wells in "High Magnetic Fields in Semiconductor Physics II"	G.E.W.Bauer	Springer Series in Solid State Sciences vol.87(1988)
22 Laser Spectroscopy of Semiconductor Quantum Wells	A.S.Plaut	Thesis Oxford University(1988)
23 Observation of Decoupled Heavy and Light Holes in Ga$_{1-x}$Al$_x$As/GaAs Quantum Wells by Magnetoreflectivity	A.S.Plaut, J.Singleton, R.J.Nicholas, R.T.Harley, S.R.Andrews, C.T.B.Foxon	Phys.Rev.B 38(1988)1323
24 Private Communication	S.R.Andrews	1991
25 g-factor Anisotropy in the Two-Dimensional Electron Gas of GaAs/AlGaAs Heterostructures	M.Dobers, K.V.Klitzing, G.Weimann	Solid State Comm. 70(1989)41
26 k.p Perturbation Theory in III-V Compounds and Alloys: a Reexamination	C.Hermann, C.Weisbuch	Phys.Rev.B. 15(1977)823

27 Optical Detection of Conduction-Electron Spin Resonance in $Ga_{1-x}Al_xAs$, GaAs, $Ga_{1-x}In_xAs$	C.Weisbuch, C.Hermann	Phys.Rev.B 15(1977)816
28 Symmetry and Strain induced Effects in Semiconductors	G.L.Bir, G.E.Pikus	New York:Wiley (1974)

4 Exchange Interactions in Type I GaAs/Al$_{0.36}$Ga$_{0.64}$As, GaAs/AlAs and In$_{0.11}$Ga$_{0.89}$As/GaAs Quantum Wells

4.1 Summary

The magnetic field dependence of the circularly polarised recombination has been studied for three different type I quantum well systems as a function of well width. Measurements have been made for two different excitation condition; first linearly polarised excitation at or near the peak of the heavy-hole exciton absorption and second excitation at energies into the electron-hole continuum. In most cases for each type of measurement the magneto-polarisation exhibited two peaks, one for each direction of magnetic field applied perpendicular to the plane of the wells. In conjunction with the exciton g-factors these magneto-polarisation peaks were used to obtain the exchange splittings among the exciton levels as a function of well width.

We have obtained values for the small zero field splitting of the optically allowed states (figure 3.1) which indicates departure from D_{2d} symmetry, and also the separation of the allowed and forbidden states, the major exchange interaction. The former splittings are probably associated with asymmetry in the growth of the samples. The major exchange splittings are compared with a theory of the exchange enhancement in quantum wells based on changes in electron-hole overlap. The agreement is excellent.

4.2 General Background

The splitting of the optically active and inactive levels of an exciton in a quantum well in zero field and the level crossing signals in the magneto-polarisation spectra of these excitons are a result of the electron-hole exchange interactions. These exchange interactions are due to the electron-hole overlap and so are expected to be sensitive to both quantum well width and barrier heights. In both bulk crystals and quantum wells, the electron-hole exchange interaction consists of both short and long-range exchange parts. The fine structure of the exciton in bulk GaAs has been extensively researched[1-5]. This chapter concerns the fine structure of the heavy-hole exciton in GaAs heterostructures associated with the short range analytical part of the exchange. The long range nonanalytical part gives rise to a splitting ΔE_{LT} between longitudinal and transverse light-hole excitons for $k=0$.

The exchange interaction in QWs can be expressed in terms of the coordinates of electron and hole $\check{r}_e$ and $\check{r}_h$ by the operator

$$H_{exc} = \Omega \underline{E} \delta(\check{r}_e - \check{r}_h) \qquad 4.1$$

where Ω is the volume of the primitive unit cell, $\underline{E}$ is an 8x8 matrix in the basis of the heavy-hole exciton state and Dirac's delta function represents a short range repulsion between electrons and holes. It is obvious from equation 4.1 that we can expect an increase in the exchange interaction in the type I systems over that measured in the type II system due to the spatial separation of the electron and hole. We would also expect an enhancement in the type I system compared to that measured in bulk materials.

To date, there is good experimental data on the exchange interaction in both bulk GaAs[1-5] and type II GaAs/AlAs quantum wells[6-10], the data in the latter case agreeing with theoretical predictions[11]. Optically detected magnetic resonance (ODMR) and Quantum beat emission (QB) have been the main experimental methods employed to study the fine structure but due to the short lifetime of the type I exciton, ODMR cannot be used successfully to study spin resonances in the type I quantum wells. As chapter 3 outlined, in an applied magnetic field, level crossing (or anticrossing) effects can be present in the circular polarisation of the photoluminescence at 1.8K. This enables the exchange energy of the exciton to be obtained if the magnetic g-factors are known.

One reason for the interest in the exchange interaction of excitons in quantum confined structures is its influence on spin-lattice relaxation. This chapter will show that the enhancement of the exchange interaction in a quantum confined exciton is a sensitive function of quantum confinement and later, in chapter 5, we will show that the spin-lattice relaxation of isolated electrons and holes is also a sensitive function of quantum confinement. Depending on the carrier confinement, the exchange interaction can fall into the strong exchange regime or the weak exchange regime. D'yakonov and Perel[12]. suggested that the spin relaxation time of the carriers is governed by which regime the exchange interaction complies with.

4.3 Level crossing signals

Figure 3.1 shows the heavy-hole exciton energy levels as a function of magnetic field applied parallel to the growth axis for the case where the symmetry is lower than D_{2d} giving a splitting of the optically allowed states in zero field. As the field strength grows, two processes take place; 1: the character of the optically allowed states changes from linearly polarised to circularly polarised and 2: they intersect the optically inactive levels. These two processes give rise to the low and high field peaks: the low field due to the initial change in polarisation brought about by the unmixing of the optically active levels under the external influence of the magnetic field, the high field peak, due to the existence of an anticrossing[6,7,13] between the optically active and optically inactive excitonic levels respectively.

4.3.1 The low field peak

Excitation at, or near the heavy-hole peak with linearly polarised light generates excitons only in the optically allowed exciton states. Existence of the low field peak indicates a splitting between the optically active states, a situation, which does not occur in D_{2d} symmetry normally assumed for quantum wells (see diag 4.1). The quantum wells do not posses 4-fold symmetry about the growth axis and have the lower symmetry order C_{2v}. A similar symmetry reduction is also observed in type II QWs[6,7,11,14]. In both type I and type II samples the (110) and ($\bar{1}$10) axes are inequivalent and the removal of the degeneracy at B=0 may be described as an extra exchange splitting.

It will be shown later (section 4.6.2) that the low field peak is due to the change in character of the exciton states from linearly polarised along (110) and ($\bar{1}$10) at zero field to circularly polarised (σ^+ and σ^-) in high fields. Section 4.6.2 shows how this leads to an expression for the exchange splitting between the optically active levels, δ, given by equation 4.2

$$\delta = \mu_B g^*_{ex} B_{lfp} \qquad 4.2$$

where B_{lfp} is the position of the low field peak, g^*_{ex} is the exciton g-factor in the well and μ_B is the Bohr magneton.

By combining the values of B_{lfp} with those of g^*_{ex} measured in chapter 3 for the GaAs/AlGaAs type I wells, we have calculated the magnitude of δ and its well width

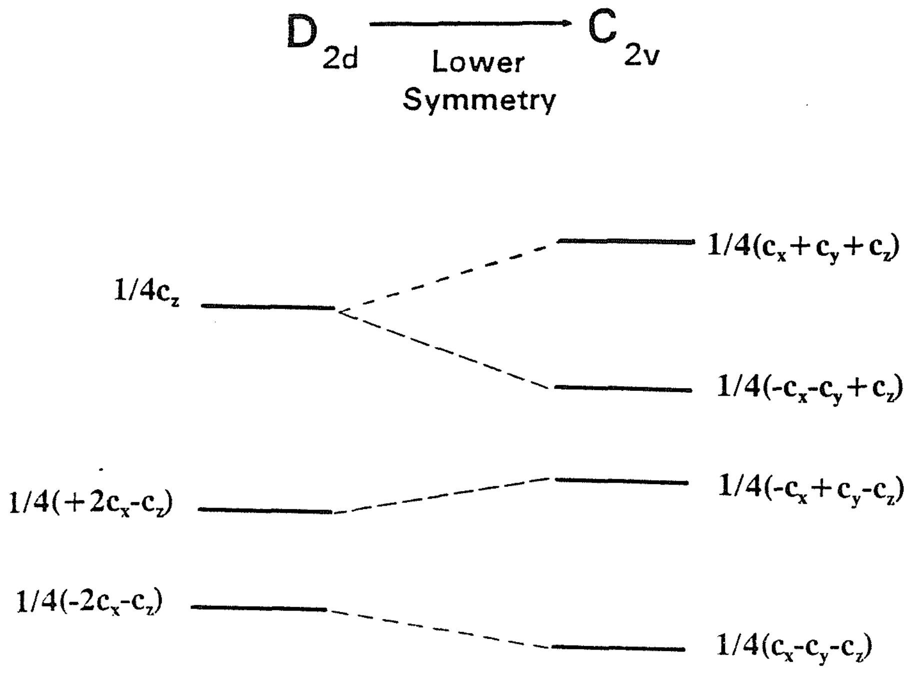

Figure 4.1 The zero field exchange splitting associated with D_{2d} and C_{2v} symmetry.

dependence in GaAs/AlGaAs. For the GaAs/AlAs QWs both low and high field peaks were observed, the magnitude of δ were calculated using the excitonic g-factors measured for GaAs/AlGaAs in chapter 4, as attempts to measure the exciton g-factor from the luminescence line spin-splitting using the method described in chapter 3 were hindered by the prominence of level crossing effects in the splitting. These were similar to that previously observed in the spin-splitting of the 24.7Å GaAs/AlGaAs QW (chapter 3, figure 3.12). These values of δ at least provided a first estimate for the magnitude of the heavy-hole spin-splitting in the GaAs/AlAs QWs.

Due to the proximity of the laser line to the recombination line, the low field peak could only be accurately resolved if narrow slits were used so the laser light could be rejected.

4.3.2 The high field peak

Excitation in the heavy-hole continuum with linearly polarised light produces equal population of all the four exciton states. The mechanism of the appearance of the high field peak is not clear, but it must involve population redistribution at the level crossings and not simply a change in character of the states. From figure 3.1 we can see that at a level anticrossing the lowest optically active level has descended in energy by $(g^*_e+g^*_h)\mu_B/2$, while the highest optically inactive level has risen in energy by $(g^*_e-g^*_h)\mu_B/2$. This leads to an expression for the exchange interaction J given by equation 4.3:

$$J = g^*_h \mu_B B_{hfp} \qquad 4.3$$

where B_{hfp} is the position of the high field peak, g^*_h is the hole g-factor and again μ_B is the Bohr magneton .

From the hole g-factors calculated in chapter 3 for the GaAs/AlGaAs QWs and using the values of g^*_h measured in type II GaAs/AlAs quantum wells[6,8] by ODMR we have calculated the exchange splitting between the spin parallel and spin reversed exciton states as a function of well width in both GaAs/AlGaAs and GaAs/AlAs QWs.

In contrast to the low field peak, the luminescence from the whole of the linewidth was detected using very wide slits. This was to remove the effects of exciton thermalisation to lower energies within the inhomogeneous linewidth as far as possible.

Although the technique successfully resolved level crossing signals from the magneto-polarisation spectra for the GaAs/AlGaAs and GaAs/AlAs quantum wells, we were unsuccessful in measuring the level crossing signals for the InGaAs/GaAs QWs.

4.4 Equipment

The samples used in this experiment were the undoped GaAs/AlGaAs and GaAs/AlAs G-samples from Phillips: G50, G57, G51, G167, G171 and G127 together with the undoped InGaAs/GaAs DB-samples from GEC: DB918, DB849 and DB847 described in chapter 2. These were cooled to 1.8K in the single transfer cryostat where a magnetic field was applied perpendicular to the plane of the quantum wells using the 10T magnet. Both the HeNe and the Spectra Physics Ar^+ laser pumping either the Oxford University Coherent CR599 dye laser copy or the Spectra Physics Ti-Sapphire were used as excitation sources. The experimental arrangement was that described in chapter 2 figure 2.1 but modified as in chapter 3, figure 3.2. The PEM followed by the linear polariser on the output gave the degree of circular polarisation of the emission.

4.5 Results

Figures 4.2-4.12 show typical magneto-polarisation spectra for both low and high field peaks for the GaAs/AlGaAs and GaAs/AlAs wells. Excitation at the heavy-hole resonant transition produced the low field peak superimposed on a linearly increasing background for both orientations of the magnetic field in all the G-samples. The increasing

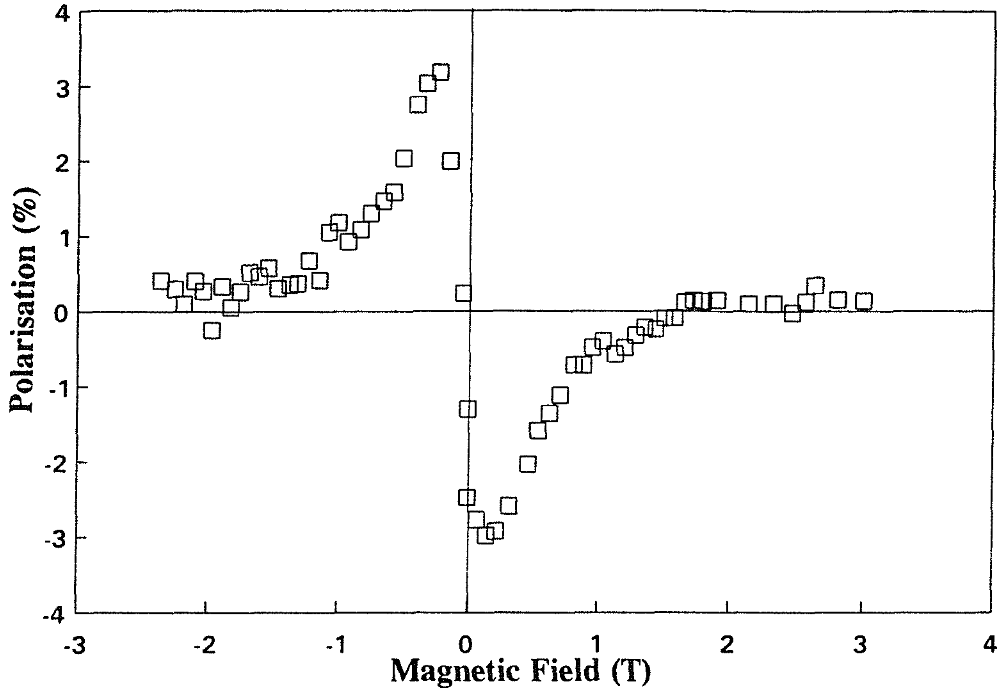

Figure 4.2 The low field magneto-polarisation peak of G50 the 24.7Å GaAs/AlGaAs sample.

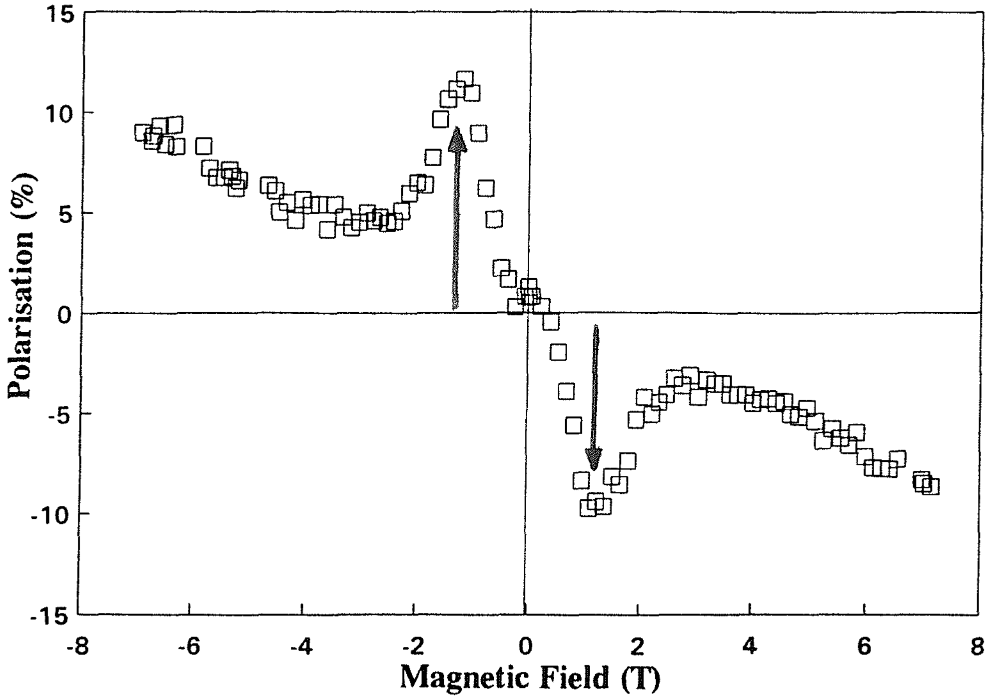

Figure 4.3 The high field magneto-polarisation peak of G50. The arrows indicate roughly the positions of the peaks.

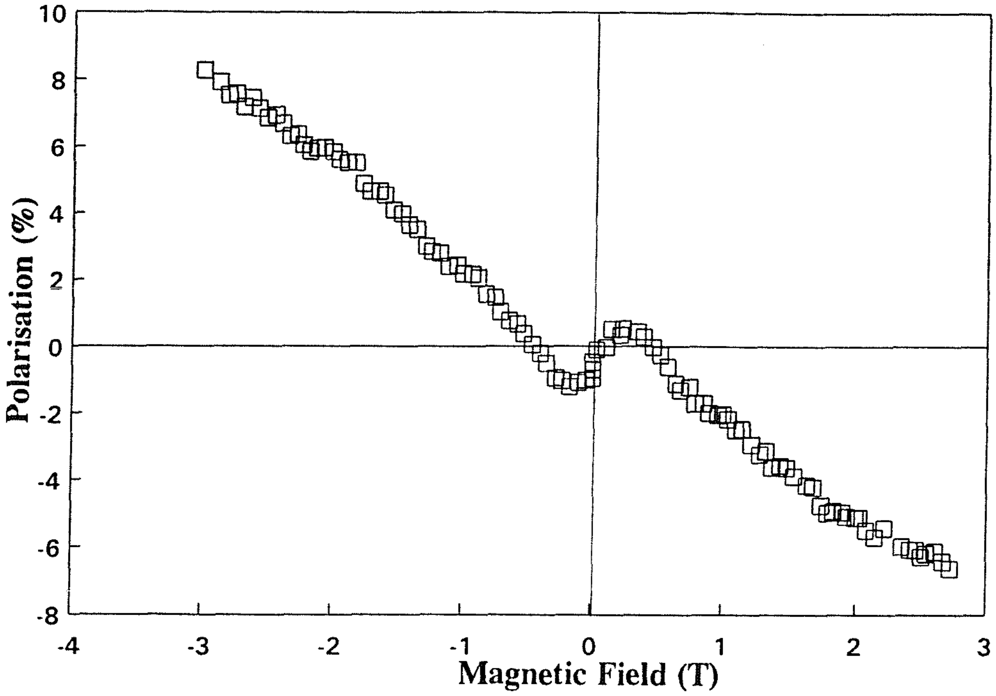

Figure 4.4 The low field magneto-polarisation peak for G57 the 56Å GaAs/AlGaAs sample.

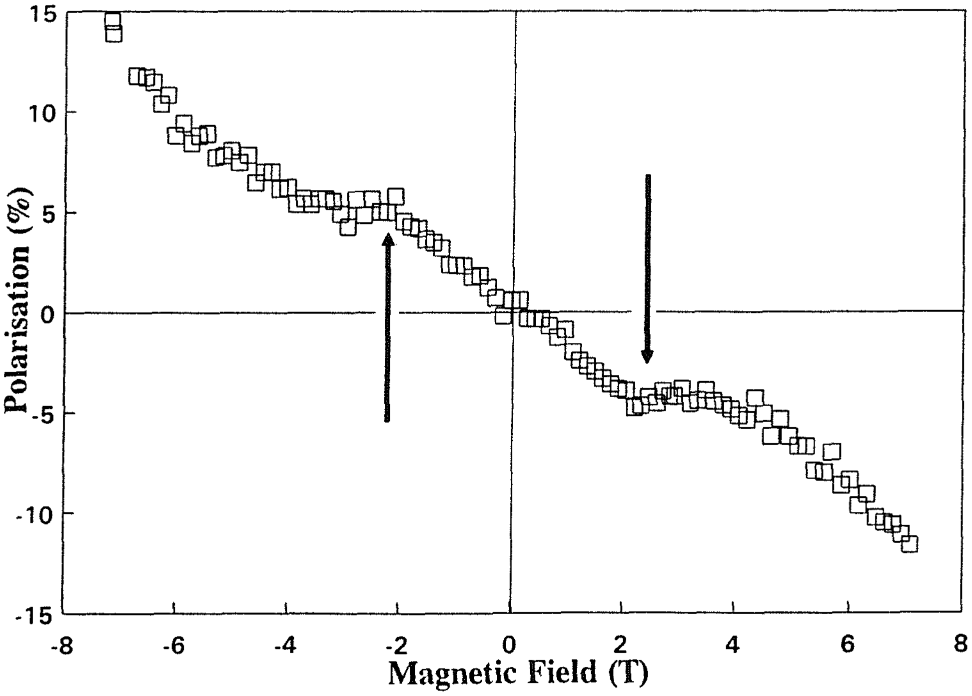

Figure 4.5 The high field magneto-polarisation peak of G57. The arrows are a rough indication of the peak positions.

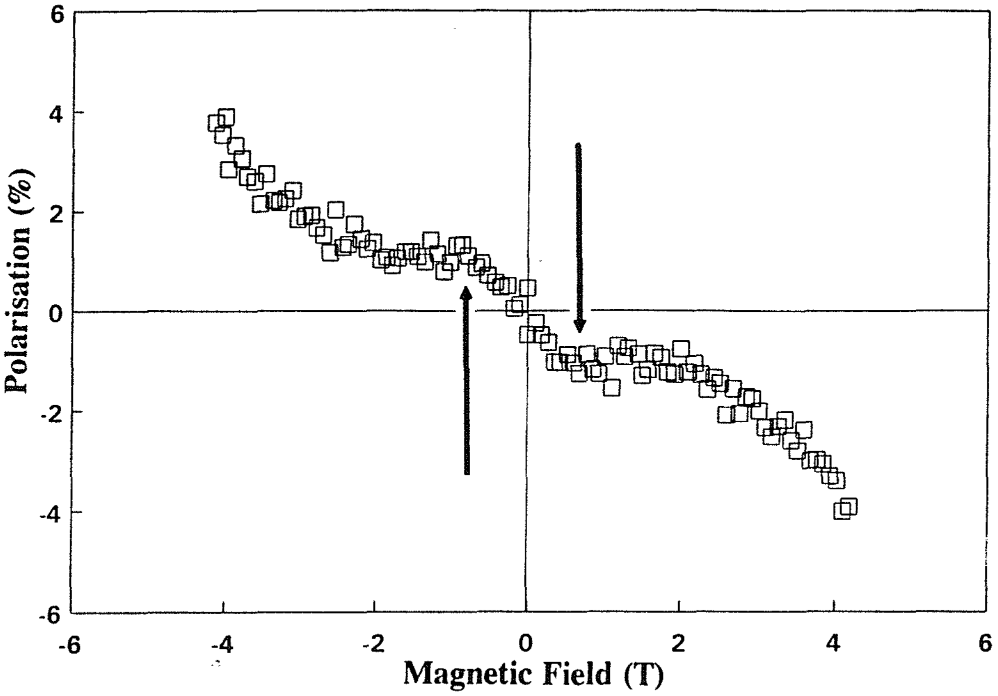

Figure 4.6 The low field magneto-polarisation peak of G51 the 73.4Å GaAs/AlGaAs sample. Once more, the arrows indicate the peak positions.

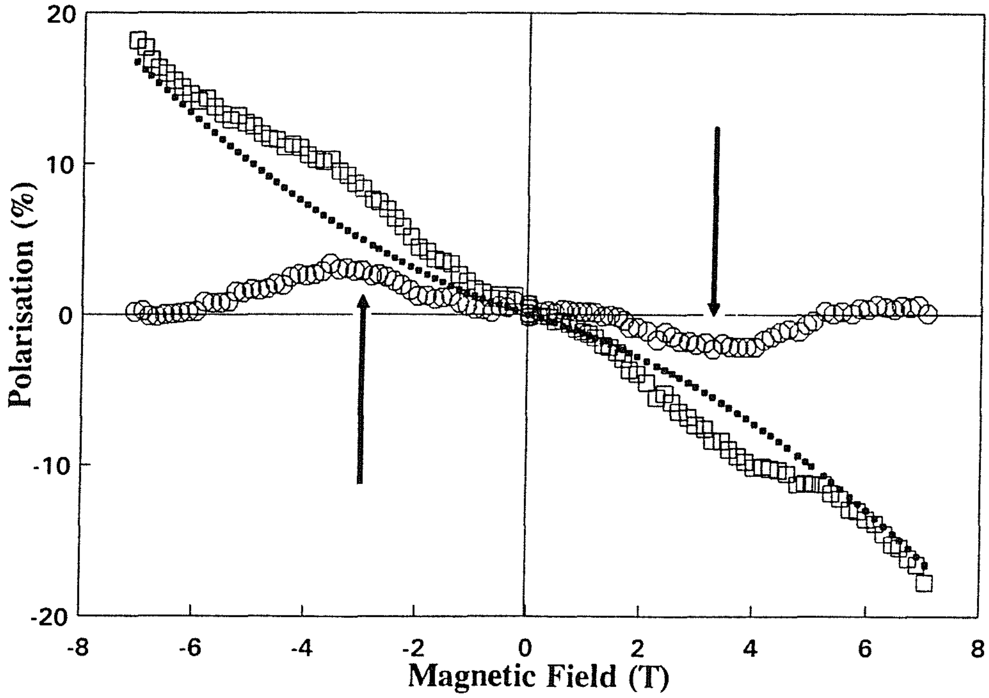

Figure 4.7 The high field peak of G51 together with the low order polynomial fit to the background polarisation in this case (small squares) and the resolved peak in the polarisation.

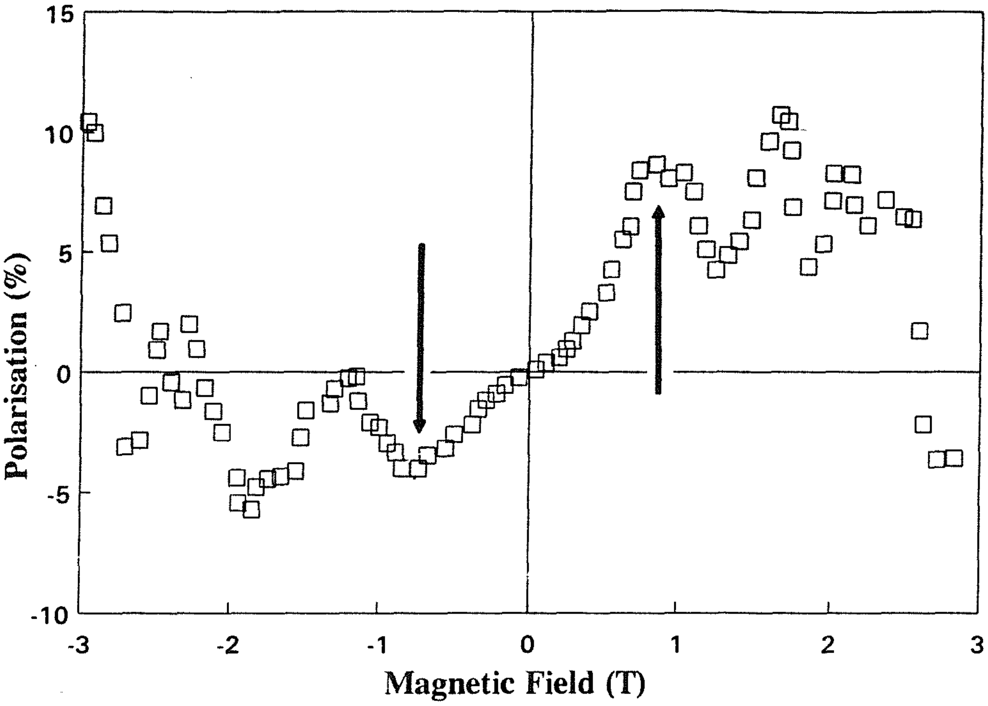

Figure 4.8 The low field peak of G167 the 49.6Å GaAs/AlAs sample.

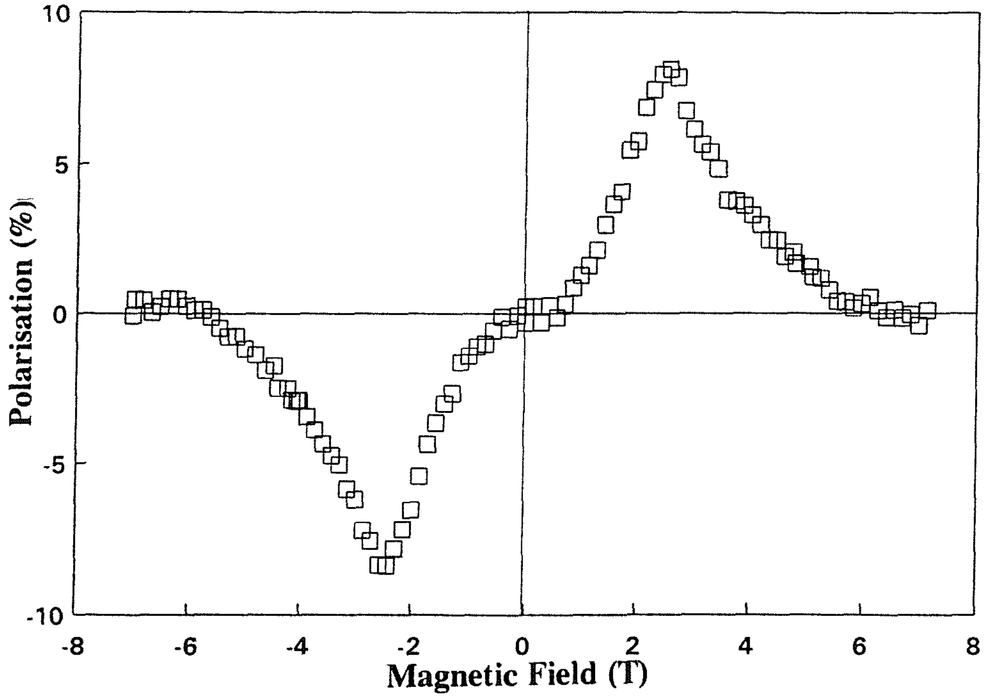

Figure 4.9 The high field peak of G167.

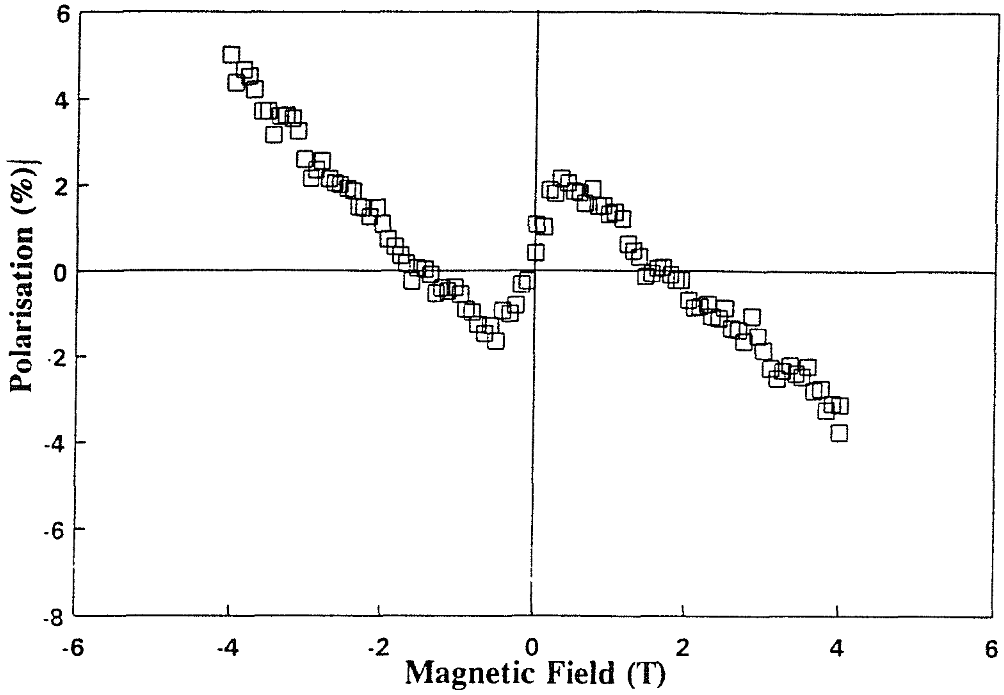

Figure 4.10 The low field peak of G171 the 65.1Å GaAs/AlAs sample.

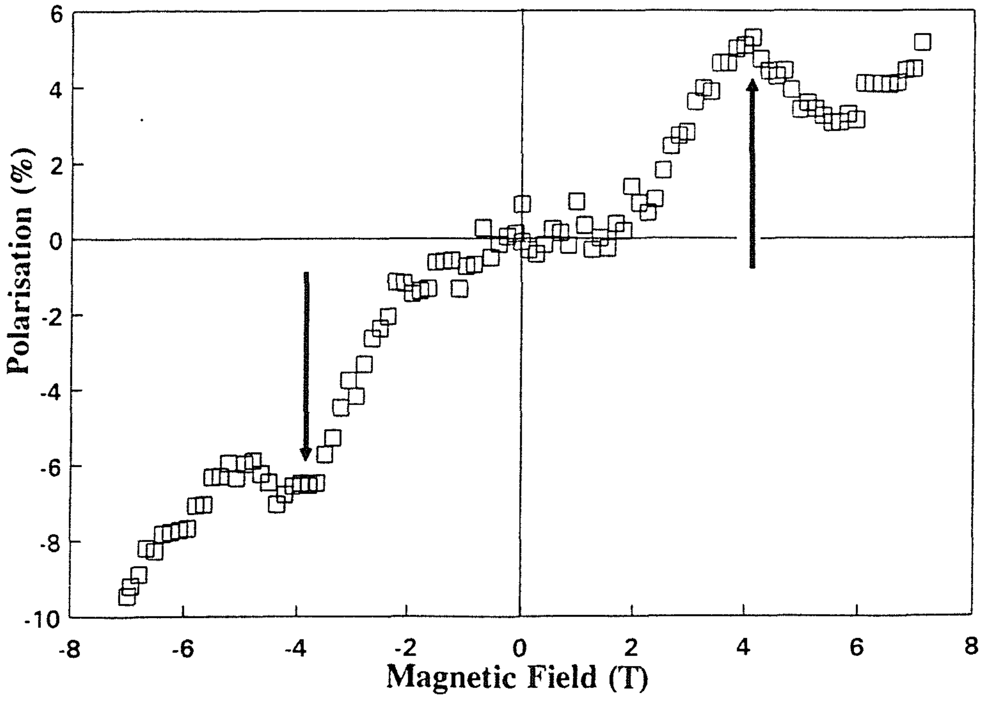

Figure 4.11 The high field peak of G171. The arrows indicate roughly the position of the peaks.

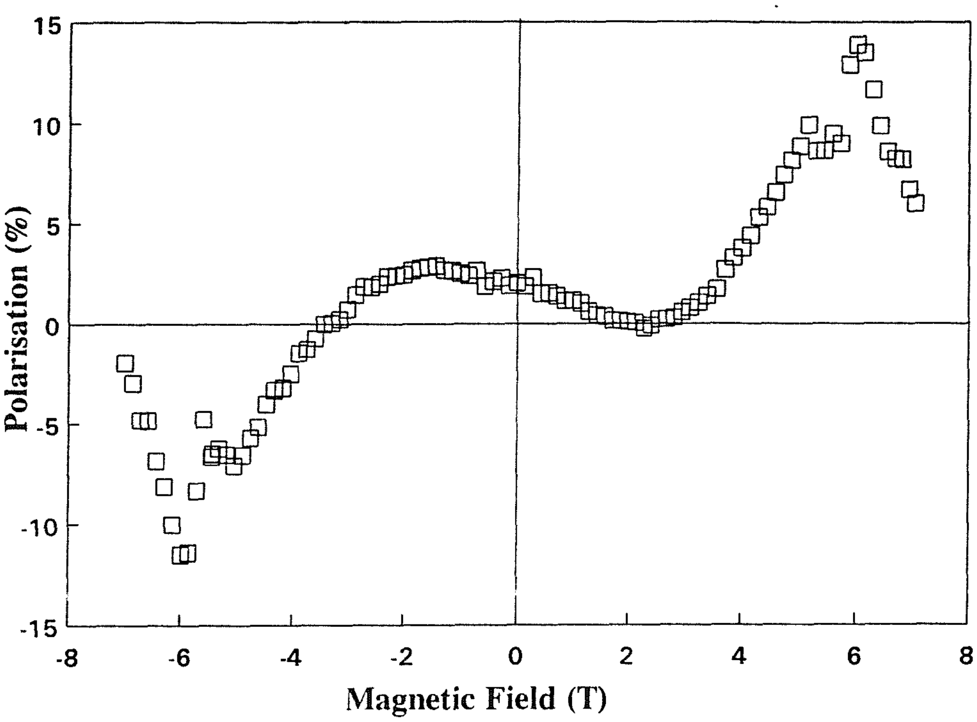

Figure 4.12 The high field magneto-polarisation peak of G127 the 82.9Å GaAs/AlAs sample.

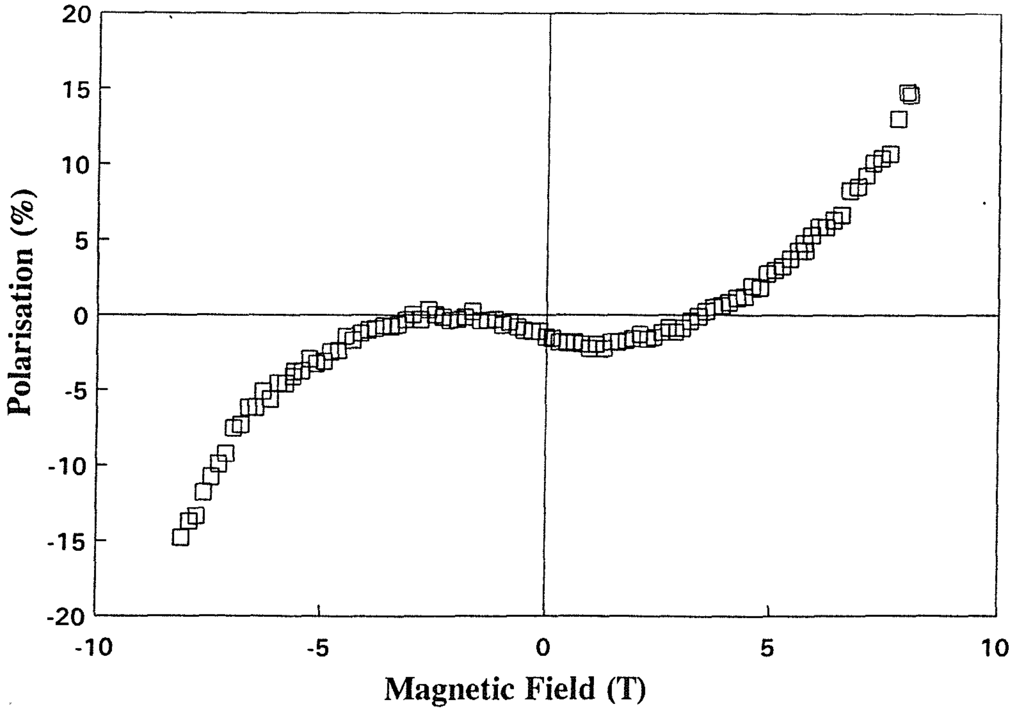

Figure 4.13 A magneto-polarisation spectra typical of the DB InGaAs/GaAs samples. This specific example is for the 30Å well in DB918.

background is caused by the difference in population of the optically allowed states, split by the field, resulting from the partial thermalisation of the excitons before recombination.

Increasing excitation to above the heavy-hole resonance, the low field peak gradually decreased in intensity and was replaced by the high field peak, the intensity of this peak increasing with increasing pump energy. Again this peak was superimposed on a linear increasing background. The prominence of the peaks decreased with increasing well width and also moved to higher fields, the high field peak moving the most rapidly.

In the case of the DB-samples (InGaAs/GaAs), no anomalies were detected in the magneto-polarisation either for excitation at the heavy-hole absorption peak or in the continuum. Figure 4.13 gives a typical example of the magneto-polarisation measured for the DB-samples pumping above the heavy-hole continuum edge. The specific case is an illustration of a typical graph obtained for the 30Å well. We can see the trend of the background polarisation does not correspond to a simple linear increase. We can see the polarisation exhibits a small decrease from its zero field value and then reaches a turning point at which the polarisation steadily increases with magnetic field strength. Referring to the Zeeman splitting of this 30Å well in figure 3.8 we can see the splitting changes sign at approx. 3T. Figure 4.13 shows the polarisation returns to its zero field value again at approx. 3T, confirming the non-linear behaviour of the Zeeman splitting with applied field shown in figure 3.8. From this alone we would have expected level crossing signals below 3T but we can only assume that our experimental technique was unable to resolve these signals. The high field magneto-polarisation of G127 exhibits similar behaviour but with the level crossing signals resolved. The appearance of these level crossing signals above the field value at which the spin-splitting changes sign renders the use of the low field g-factor in the calculation of **J** unreliable.

To obtain accurate value for the field positions B_{lfp}, B_{hfp} at which the peaks in the magneto-polarisation occurred, it was necessary to assign a field dependent trend to the background polarisation for each individual magneto-polarisation spectrum and subtract this from the total polarisation measured. As indicated above, for full thermalisation this would be determined by the Boltzmann factor and would be approximately linear in B. However, in most cases, a low order polynomial provided a good approximation to the trend of the background polarisation, indicating a field dependent and incomplete degree of thermalisation. The process is illustrated in figure 4.7 for G51 the 73.4Å GaAs/AlGaAs sample. Table 4.1 lists all the peak positions obtained in this way. We can see the necessity of background polarisation subtraction as the peaks are slightly shifted from the raw data position.

Table 4.1

Sample	**Sample Type**	**Well Width (Å)**	**B_{lfp} (T)**	**B_{hfp} (T)**
G50	GaAs/AlGaAs	24.7	0.21±0.02	1.15±0.02
G57	GaAs/AlGaAs	56	0.33±0.05	2.05±0.07
G51	GaAs/AlGaAs	73.4	0.82±0.05	3.43±0.05
G167	GaAs/AlAs	49.6	0.77±0.09	2.504±0.07
G171	GaAs/AlAs	65.1	0.9±0.09	3.65±0.06
G127	GaAs/AlAs	82.9		7±0.05

Figure 4.14 shows the trend for g^*_h in the GaAs/AlGaAs wells calculated in chapter 3 together with g^*_h for the GaAs/AlAs wells obtained form the type II measurements[6,8] and the values measured in chapter 3 for g^*_{ex} in the GaAs/AlGaAs wells. Substituting the appropriate values of g-factor in equation 4.2 and 4.3 together with the corresponding values of B_{lfp} and B_{hfp}, we have obtained the magnitudes of the exchange splittings shown in tables 4.2 and 4.3. $\mathbf{J}=1/2c_z$ represents the separation of the optically active (spin reversed) and inactive (parallel spin) states and $\delta=1/2(c_x+c_y)$ is the separation of the optically allowed states in zero field (shown in figure 4.1).

Table 4.2

Sample	**Sample Type**	**Well Width (Å)**	**Exchange Splitting J (meV)**
G50	GaAs/AlGaAs	24.7	0.14-0.06
G57	GaAs/AlGaAs	56	0.089±0.015
G51	GaAs/AlGaAs	73.4	0.04±0.01
G167	GaAs/AlAs	49.6	0.159±0.015
G171	GaAs/AlAs	65.1	0.139±0.03
G127	GaAs/AlAs	82.9	0.08±0.08

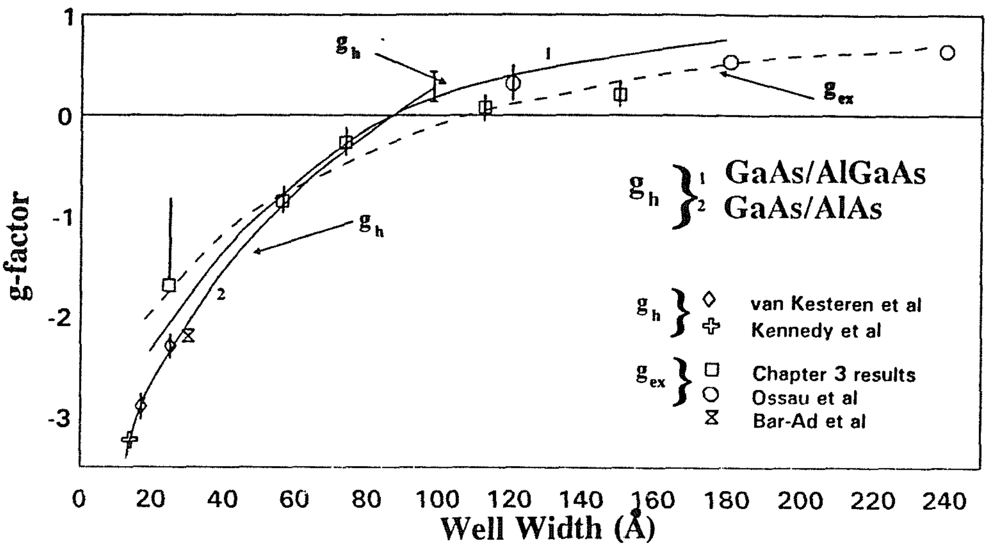

Figure 4.14 g_{ex} for GaAs/AlGaAs measured in chapter 3 together with the trend of g_h in GaAs/AlGaAs calculated in chapter 3. Line 2 is an estimate of the trend of g_h in GaAs/AlAs wells obtained from the data on g_h measured by ODMR in type II GaAs/AlAs wells

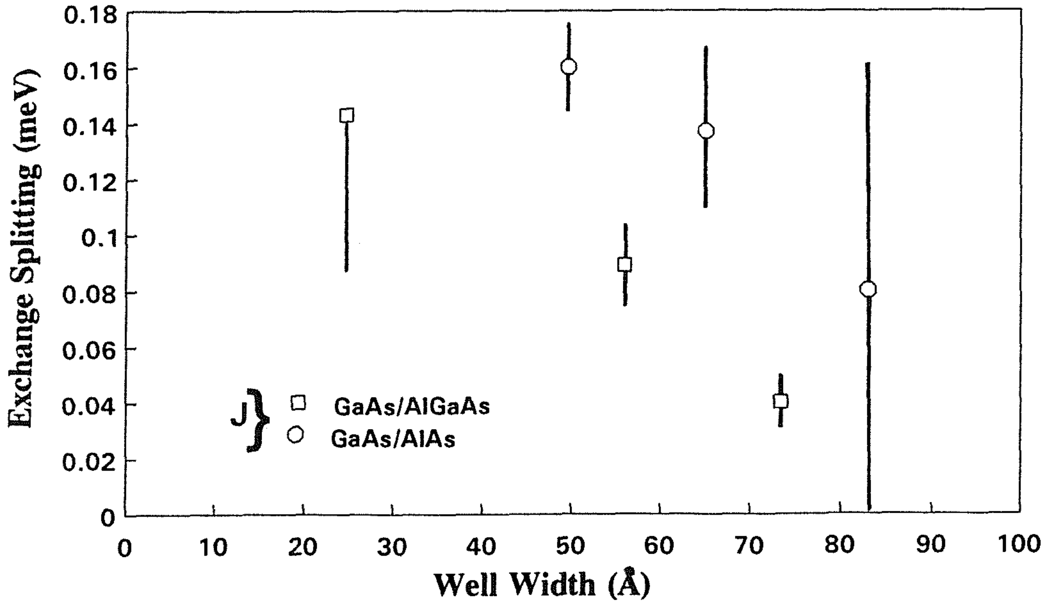

Figure 4.15 The experimental exchange splitting between the optically active and inactive states for an exciton in GaAs/AlGaAs and GaAs/AlAs.

Figure 4.15 shows that the magnitude of the exchange splitting **J** is larger in the GaAs/AlAs QWs than in the GaAs/AlGaAs QWs and that the magnitude of **J** decreases rapidly with increasing well width for both type I systems studied.

Table 4.3 gives the zero field splitting δ of the optically allowed states in the three GaAs/AlGaAs samples. The value increases slightly as the well width is reduced. The observation of a low field peak in the GaAs/AlAs (see for example figure 4.10) shows that such a splitting exists here also. We do not have direct measurements of g_{ex} in these samples but can estimate values of δ using g_{ex} measured in GaAs/AlGaAs.

The main uncertainty in all these splittings comes from the values of g-factor.

4.6 Discussion

4.6.1 High Field Splitting J

The exchange enhancement of **J** with respect to the bulk value of an exciton in a quantum well can be theoretically predicted from the overlap integral between the x, y and z part of the electron and hole wavefunctions in the exciton. Describing the exciton wavefunction in the form

$$\chi_{ex}(r)=a\chi_e(z_e)\chi_h(z_h)\phi(x,y,z) \qquad 4.4$$

where χ_e and χ_h are solutions of the finite square-well problem for the electron and hole and $\phi(x,y,z)$ represents the 2D exciton envelope function and contains the variational parameters (x,y,z are the relative electron-hole co-ordinates), then, dependent on the choice of envelope function, the form of the exchange enhancement can be obtained from

$$F_{ex} = \frac{|\phi_{QW}(0)|^2}{|\phi_{bulk}(0)|^2} \int |\chi_e(z_e)\chi_h(z_h)|^2 dz \qquad 4.5$$

Figures 4.16 and 4.17 show theoretically predicted exchange enhancements from variational calculations for an exciton in a GaAs/$Al_{0.3}Ga_{0.7}As$ quantum well by Lefebvre et al[15] and for excitons in GaAs/AlAs, GaAs/$Al_{0.3}Ga_{0.7}As$ and $In_{0.11}Ga_{0.89}As$/GaAs by S.R.Andrews[16,17]. The predictions for the GaAs/$Al_{0.3}Ga_{0.7}As$ differ due to the choice of envelope function.

Similar to the trend of the exciton binding energy, S.R.Andrews[16,17] calculations show that the exchange enhancement increases for progressively smaller well widths and then shows a sudden decrease associated with the wavefunction penetrating further into the barrier material.

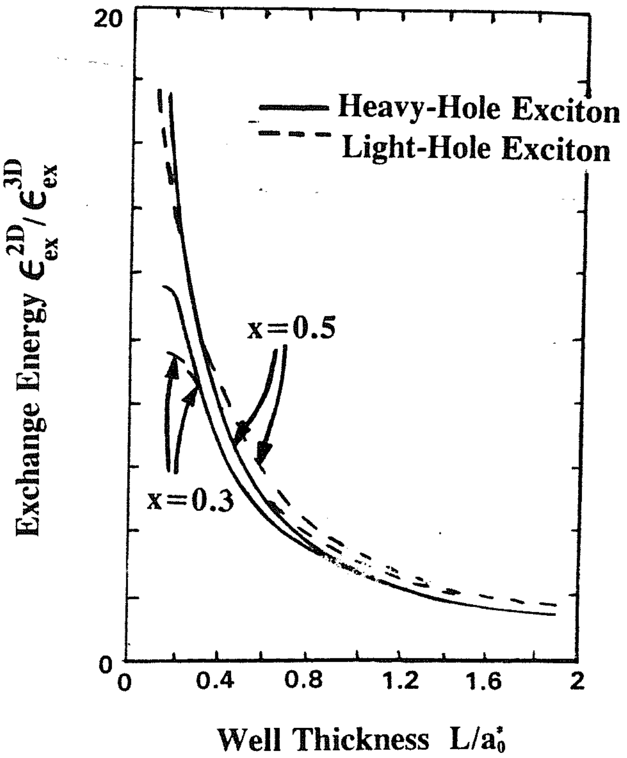

Figure 4.16 The theoretical exchange enhancement for the 2D exciton over the 3D exciton calculated by Lefebvre et al[15].

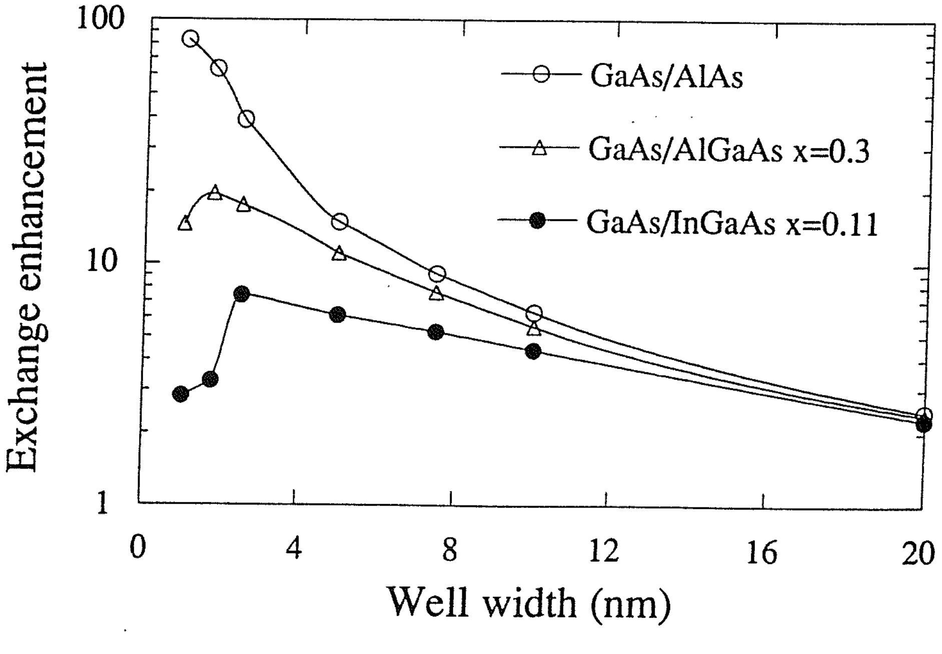

Figure 4.17 The theoretical exchange enhancement of a 2D exciton in GaAs/AlGaAs, GaAs/AlAs and InGaAs/GaAs over the corresponding bulk exciton value predicted by S.R.Andrews[16,17].

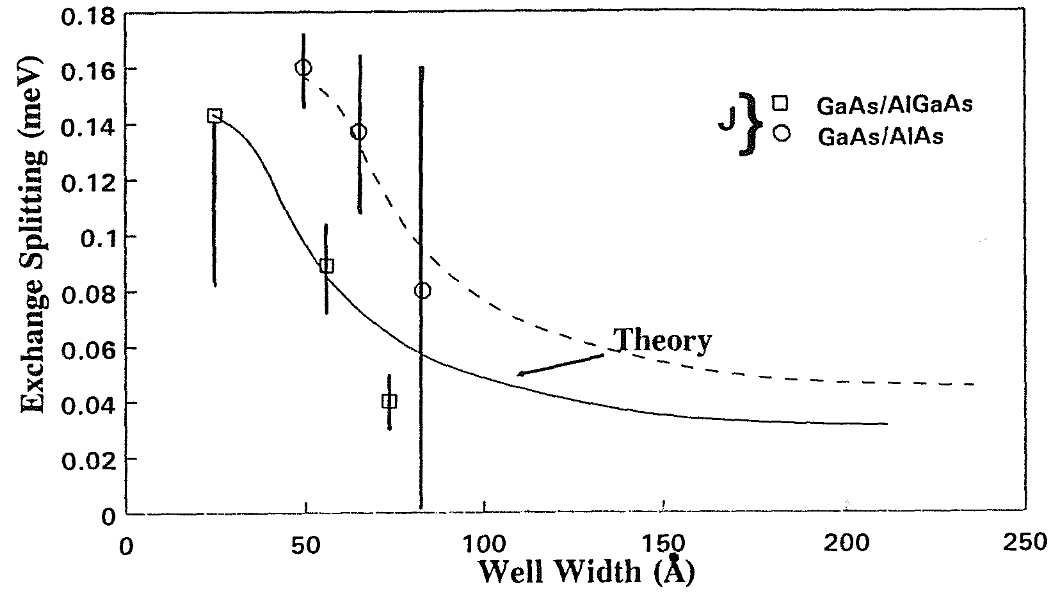

Figure 4.18 The fit of Lefebvre et al[15] theoretical exchange enhancements to our measured values of exchange splitting in GaAs/AlGaAs and GaAs/AlAs. The amplitude modification was achieved taking different values of the bulk GaAs exchange splitting.

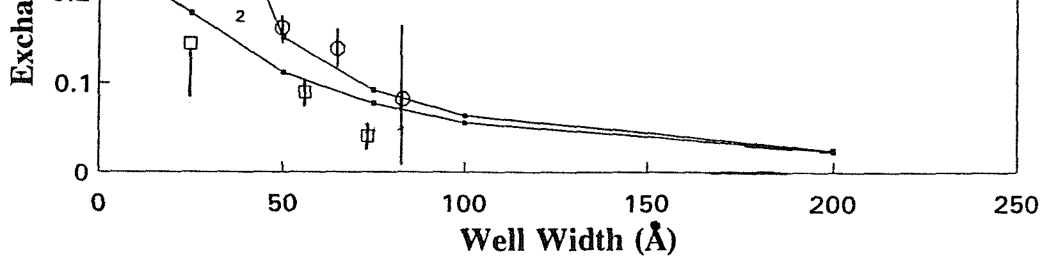

Figure 4.19 Taking a value of J_{bulk}=10μeV, the predicted exchange splittings in GaAs/AlGaAs, GaAs/AlAs and InGaAs/GaAs by S.R.Andrews[16,17] and comparison of these with our experimental exchange splittings.

Figures 4.18 and 4.19 show the corresponding fit to our measured exchange splittings for both theories. The amplitude of both theoretical fits is dependent on the value of the exchange splitting in bulk GaAs and because measurements of J_{Bulk} range from 0 to 240μeV (see references 1 to 5) for our purposes, it is instructive to use this value as an adjustable parameter, hence, scale the amplitude within this range. The fit to the GaAs/AlGaAs points shown in figure 4.18 was achieved using a value of $J_{Bulk} \approx 11.4\mu$eV. This value though, is obviously unsatisfactory for a fit to the GaAs/AlAs data points. In this case, we obtained a satisfactory fit (dashed line) by a modification of approx 50% to the fit.

Within errors, figure 4.19 shows the agreement with the theoretical predictions of S.R.Andrews[16,17] are good. Here we have assumed a value of J_{bulk} approx. 10μeV[3]. It is also instructive to note the form of the exchange splitting expected in the InGaAs/GaAs wells (see figure 4.17). This splitting is far smaller than that for the corresponding well width in both the GaAs/AlGaAs and the GaAs/AlAs QWs, this reduction in exchange splitting implying a reduction in coupling between the optically active and inactive excitonic levels. This may explain the apparent lack of level crossing signals as the exchange interaction may have been too weak to give level crossing signals, or at least a signal so weak we may have been unable to resolve it from the background polarisation.

To date, the only other measured values of the exchange splitting are in type II GaAs/AlAs QWs by Van Kesteren et al[6], Trombetta et al[8] and Gourdon et al[9].The authors in references 6, 8 and 9 observed exchange splittings approximately a factor of 10 smaller than our experimental values. The factor of 10 reduction in **J** measured for the type II wells is a consequence of the spatial separation of the electron and hole in the type II wells. The overlap integral will be greatly reduced compared to that of the electron and hole in the type I exciton. This leads to the greatly reduced magnitude of the exchange interaction in the type II wells as calculated by Bauer et al in reference 19.

4.6.2 Zero Field Splitting δ

Detailed earlier, was the description of the low field peaks by equation 4.1. This equation is obtained from a model of the low field magneto-polarisation in which the optically allowed excitonic energy levels are treated as a two level system, each level pumped at a different rate, but with relaxation between levels and recombination from each level to the ground state. Application of the Hamiltonian[6] and basis states given in chapter

3 and assuming linear polarised excitation gives the degree of circular polarisation of emission as:

$$P(x,y,\delta) = \frac{x}{\sqrt{x^2+1}}\left(\frac{y}{y+1}\frac{1}{\sqrt{x^2+1}} - \frac{1}{y+1}\tanh\left(\frac{\delta}{2kT}\sqrt{x^2+1}\right)\right) \qquad 4.6$$

with

$$x = \frac{\mu_B g^*_{ex} B}{\delta} \qquad 4.7$$

and

$$y = \frac{\tau_s}{\tau_r} \qquad 4.8$$

μ_B is the Bohr magneton, g^*_{ex} the excitonic g-factor, δ the zero field splitting, and τ_s and τ_r are the excitonic spin relaxation and recombination times respectively.

Equation 4.6 can be separated out into two terms. The first describes the effect of the continuous change in the character of excitonic states from linear to circular polarisation in a magnetic field. It is dominant if y is large (slow spin relaxation) and is the origin of the low field peak in the polarisation, having a maximum when $x=1$ ie when $B=\delta/\mu_B g_{ex}^*$ 9 (c.f. equation 4.2). The second term describes the effect of the thermally induced population difference of the levels in the polarisation. It is dominant for small y (rapid spin relaxation) and gives a smooth increasing background polarisation.

Using the values of the excitonic g-factor measured in chapter 3, in conjunction with the values of B_{lfp} listed in table 4.1 we obtain the values of δ shown in table 4.3:

Figure 4.20 shows a comparison of the magnitude of the exchange splitting between the optically active excitonic levels, δ, for the GaAs/AlGaAs and GaAs/AlAs. Again we see, as with **J**, there is a reduction in the exchange splitting, δ, for larger well widths.

The evidence of the splitting δ is in agreement with the observation in type II QW systems that the well symmetry is of the lower point group C_{2v}, rather than that of the D_{2d} point group which is associated with a degeneracy of the optically active excitonic levels in zero field. Although interesting, we believe this effect to be due to imperfections of the samples associated with growth asymmetry. It is significant, perhaps, that both our samples and the type II samples were grown by the same group at Philips, Redhill.

Table 4.3

Sample	Sample Type	Well Width (Å)	Exchange Splitting δ (meV)
G50	GaAs/AlGaAs	24.7	0.022-0.004
G57	GaAs/AlGaAs	56	0.018±0.002
G51	GaAs/AlGaAs	73.4	0.012±0.005
G167	GaAs/AlAs	49.6	0.04±0.004
G171	GaAs/AlAs	65.1	0.032±0.006

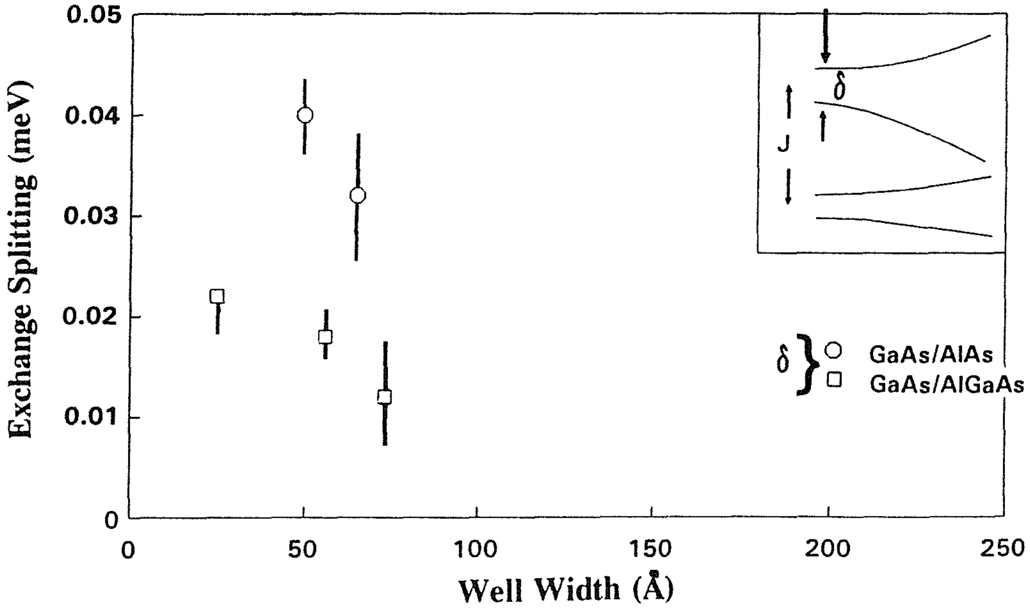

Figure 4.20 Comparison of the zero field exchange splitting δ in GaAs/AlGaAs and GaAs/AlAs

4.7 Conclusions

We have studied the exchange splitting **J** and δ of excitons in various quantum well structures. Of most significance are our measurements of **J** in the type I wells. Firstly, they show, quite convincingly, the well width dependence of the exchange splitting for type I wells, and also the effect of barrier height. Calculations of exchange enhancement with respect to the bulk material are in excellent agreement with our measurements and can be extended to give an indication of the variation of exchange between different heterostructures. In particular, much lower enhancements are expected in InGaAs/GaAs because of reduced overlap.

As discussed in chapter 5, we believe that the exchange interaction plays an important role in spin dynamics of excitons, since it inherently determines the coupling of the electron and hole forming the exciton. The large observed and calculated variations may help to explain the wide variation of spin-relaxation times which are observed.

4.7 References

1 Free Carrier and Exciton Recombination in GaAs	M.A.Gilleo, P.T.Bailey, D.E.Hill	Phys.Rev. 174(1968)898
2 Polariton Reflectance in Photoluminescence in High-Purity GaAs	D.D.Sell, S.E.Stakowski, R.Dingle. J.V.Dilorenzo	Phys.Rev.B 7(1973)4568
3 Spin Relaxation of Photoelectrons in p-type Gallium Arsenide	G.Fishman, G.Lampel	Phys.Rev.B 16(1977)820
4 Determination of the Analytical and Nonanalytical Part of the Exchange Interaction of InP and GaAs from Polariton Spectra in Intermediate Fields	W.Ekardt, K.Losch, D.Bimberg	Phys.Rev.B 20(1979)3303
5 Free-Exciton Energy Spectrum in GaAs	S.B.Nam, D.C.Reynolds, C.W.Litton, R.J.Almassy, T.C.Collins	Phys.Rev.B 13(1976)761
6 Fine Structure of Excitons in Type-II GaAs/AlAs Quantum Wells	H.W. van Kesteren, E.C. Cosman, W.A.J.A. van der Poel, C.T.Foxon	Phys.Rev.B 41(1990)5283
7 Optically Detected Magnetic Resonance Study of a Type II GaAs/AlAs Multiple Quantum Well	H.W.van Kesteren, E.C.cosman, F.J.A.M.Gredanus, P.Dawson, K.J.Moore, C.T.Foxon	Phys.Rev.Lett. 61(1988)129
8 Optically Detected Magnetic Resonance of Excitons and Shallow Donors in $(GaAs)_5/(AlAs)_5$ Superlattices.	J.M.Trombetta, T.A.Kennedy	Pre-print
9 Fine Structure of Heavy-Hole Excitons in GaAs/AlAs Superlattices	C.Gourdon, P.Lavallard	Phys.Rev.B 46(1992)4644

10 Quantum Beats in the Exciton Emission of Type-II GaAs/AlAs Quantum Wells	W.A.J. van der Poel, A.L.G.J.Severens,C.T.Foxon	Pre-print
11 Exchange Interactions in Type II Quantum Wells	B.R.Salmassi, G.E.W.Bauer	Phys.Rev.B. 39(1989)1970
12 Theory of spin orientation in "Optical Orientation"	M.I.D'yakonov, V.I.Perel	Modern Problems in Condensed Matter Sciences 8(1984)11 North Holland
13 Gallium Interstitials in GaAs/AlAs Superlattices	J.M.Trombetta, T.Kennedy, W.Tseng, D.Gammon	Phys.Rev.B 43(1991)2458
14 Order of the X-Conduction Band Valleys in Type-II GaAs/AlAs Quantum Wells	H.W. van Kesteren, E.C.Cosman, P.Dawson, K.J.Moore, C.T.Foxon	Phys.Rev.B 39(1989)13426
15 Exchange Effects on Excitons in Quantum Wells	Y.Chen, B.Gil, P.Lefebvre, H.Mathieu	Phys.Rev.B. 37(1988)6429
16 Private Communication	S.R.Andrews	1992
17 Private Communication	S.R.Andrews	1992
19 Exchange in Type II Quantum Wells	B.R.Salmassi, G.Bauer	Phys.Rev. 39(1989)1970

5 Atomic Exciton Spin Relaxation.

5.1 Summary

The spin polarised luminescence from a single GaAs/AlGaAs QW of width 57.5Å was monitored as a function of carrier concentration and of temperature from 1.8K up to ≈ 70K. The sample was electrically biased corresponding to the following three regimes for carrier populations in the wells; degenerate hole population, degenerate electron population and wells depleted sufficiently of carriers that atomic excitons are formed. Using the polarisation dependence, together with measurements of electron-hole recombination times to evaluate the temperature dependence of the spin relaxation time for a degenerate hole or electron population and for excitons in turn, we concluded that the hole spin relaxation time is wave vector dependent to a far greater extent than that of the electrons. Since the exciton wavefunction consists of a superposition of wavevectors spanning a range $2\pi/a_0$ this indicates the strong wavevector dependence of the hole relaxation time is the dominant factor in the relaxation dynamics of the atomic exciton.

5.2 Introductory Review of Spin Relaxation Mechanisms.

The following, is a review of the mechanisms which govern the spin-lattice relaxation of conduction electrons, holes and excitons, together with some of the published experimental data that exists to date.

The experimental values of spin relaxation times of photoexcited carriers in bulk GaAs, type I GaAs/AlGaAs quantum wells and in type II GaAs/AlAs quantum wells exhibit surprisingly wide variations at low temperatures. Although conduction electron spin relaxation times in bulk GaAs[1,2] and AlGaAs[3] crystals are similar to those measured in type I GaAs/AlGaAs QWs[4,5,6] and are relatively long (0.4-10ns), the hole and exciton relaxation times differ significantly in bulk and quantum well. To understand these differences in the spin relaxation times we must examine the various mechanisms producing the spin relaxation.

Chapter 1 described the wavevector dependent spin-splitting of the conduction band in III-V semiconductors that is a consequence of the crystal symmetry[7]. This spin-splitting is also present in a quantum well and in both cases is proportional to the cube of the quasimomentum. It is responsible for one of the spin relaxation mechanisms for electrons in quantum wells and bulk GaAs as it can be considered as equivalent to a magnetic field acting on the spins, whose direction and magnitude is governed by the direction of the momentum vector **k**. Without collisions, any spin orientation would precess around the vector which is defined by this internal magnetic field. The presence of collisions which change the momentum provoke random changes of the axis of precession, in turn, lead to the spin relaxation. This spin relaxation mechanism was first put forward by D'yakonov and Perel[8] (DP). The spin relaxation rate is proportional to the collision time τ_s, as $\tau_s^{-1} \propto \tau_{\text{collisions}}$, and typically, this mechanism leads to spin relaxation times of the order 1-10ns[9].

In p-type semiconductors where there is sufficient hole concentration present the exchange interaction can efficiently transfer angular momentum from the electrons to holes. Bir, Aronov and Pikus[10] (BAP) have studied the relaxation mechanism resulting from the coupling of the electron and hole spins. They found that if the hole relaxation is rapid it may limit the electron spin relaxation. This process may dominate over the DP mechanism in quasi-2D systems for $n_h \geq 1\text{x}10^{11}\text{cm}^{-2}$ resulting in shorter relaxation times than that from the DP mechanism[9]. A typical value was measured by Damen et al[4] in an 80Å, $4\text{x}10^{11}\text{cm}^{-2}$ p-type GaAs/AlGaAs MQW of 0.15ns, and they calculated that the enhancement of the spin relaxation rate in a p-type quantum well over that in p-doped bulk GaAs by the BAP[10] mechanism is roughly three times that of the enhancement of the spin relaxation rate due to exchange (DP)[9].

For free holes in bulk and in a quantum well the spin relaxation mechanisms differ due to the nature of the valence bands. In bulk, the Γ_8 valence band is four-fold degenerate and has angular momentum $J=\pm 3/2$. Any spin orientation in the valence bands is rapidly lost due to the collisions that change the hole wavevector and result in a mixing of the $m_J=\pm 3/2$ states with the $m_J=\pm 1/2$ states. This gives a short spin relaxation time, typically of the order of 1-5ps[11].

In the QW the degeneracy between the light-hole ($m_J=\pm 1/2$) and the heavy-hole bands ($m_J=\pm 3/2$) is lifted at $k=0$, m_J being a good quantum number. However away from $k=0$ the valence state is a linear combination of m_J states. At $k=0$ without any m_J mixing, the hole spin relaxation time is long and as suggested theoretically by Sham et al[12], is roughly equal to the electron relaxation time ie. of the order 1-10ns.

Due to the mixing of the valence band states away from $k=0$, m_J is no longer a good quantum number but instead, as pointed out by of Sham et al[12], we may classify the valence band states according to their parity p given by equation 5.1

$$p_m = p(-1)^{3/2-m} \qquad 5.1$$

where m(=3/2, 1/2, -1/2, -3/2) denotes the z component of the 3/2 spin, $p_m(=\pm 1)$ denotes the parity of *m*th wavefunction of the hole state with parity p. The hole relaxation takes place through the emission of acoustic phonons that can either be classed as parity-conserving or parity-flipping each with a characteristic momentum relaxation time, τ_+ and τ_- respectively, but with τ_+ quite significantly the shorter of the two. For n-doped quantum wells there is a predominance of parity-conserving scattering. While the emission of phonons provides only momentum and energy relaxation, away from $k=0$ where there are different admixtures of spin components in different hole states through the *k.p* interaction, this results in hole-spin relaxation due to the initial and final hole states differing in spin components. This also results in far shorter relaxation times than at $k=0$ which are also strongly dependent on wavevector. Bastard et al[9] confirmed this theory and calculated specific wavevector dependencies. This mechanism of spin relaxation for the holes explains[12] an anomaly in the polarised excitation spectra of n-doped quantum wells whereby the polarisation of the n=2 heavy-hole feature is negative, a phenomenon which could not be readily explained under the previously held assumption of complete hole spin relaxation prior to radiation[5,13,14]

The coupling of electron and hole forming an exciton leads to a spin relaxation mechanism that is dependent on the strength of the exchange interaction, as measured in chapter 4, between the electron and hole[15]. In the strong exchange regime the electron and hole spins relax together in a time τ_s^{ex} given by

$$\frac{1}{\tau_s^{ex}} = \frac{1}{\tau_s^{e}} + \frac{1}{\tau_s^{h}} \qquad 5.2$$

where τ_s^e and τ_s^h are the individual electron and hole relaxation times, but which are not necessarily the same as free particle values at $k=0$ as the wavefunction of the exciton is a superposition of a range of k-values. The magnitude of τ_s^e as a consequence of this should be only slightly smaller than the free electron value at $k=0$ but this wavevector superposition should result in a greatly reduced value of τ_s^h compared to that for the free hole at $k=0$. Thus the exciton spin relaxation rate should approximate to that of the hole relaxation rate

$$\frac{1}{\tau_s^{ex}} \sim \frac{1}{\tau_s^h} \qquad \text{(strong exchange)} \qquad 5.3$$

For the weak exchange regime the spins relax separately in an overall time close to the longer spin relaxation time of the two particles. The separate spin relaxation may result in a distinct two component decay of the polarisation, and indeed this has been observed in some cases using pulsed techniques[4]. It is important to realise, however, that other mechanisms can also give a two component decay, in pulsed measurements, for example a transition from a high excitation density (interacting) regime to a low density (non-interacting) regime.

The criterion governing whether the spin relaxation mechanism of a bulk exciton is in the strong or weak exchange limit was put forward by D'yakonov and Perel[15] who assumed that if the hole relaxation time was far shorter than the electron relaxation time then for strong exchange $J/\hbar \gg 1/\tau_s^h$ and for the weak exchange $J/\hbar \ll 1/\tau_s^h$. In a quantum well exciton we may assume that τ_s^h is shorter than τ_s^e and therefore that the same criterion holds as in bulk.

The magnitude of the exchange interaction between the electron and hole forming an exciton, measured in chapter 4 for the type I GaAs/AlGaAs and the GaAs/AlAs wells, was at least an order of magnitude greater than that measured in the type II GaAs/AlAs wells[16,17,19,20] and also in bulk GaAs. The reduction in the exchange interaction in the type II wells is a consequence of the spatial separation of the carriers, which results in a marked reduction in the overlap integral of the electron and hole wavefunctions. Values of the spin relaxation time for holes in bulk GaAs are ~4ps at 10K. Using our extrapolated value of J_{Bulk} from chapter 4 (10μeV) we obtain $\hbar/J \sim 60$ps which is consistent with a weak exchange regime in bulk GaAs. In type II GaAs/AlAs wells we have $\hbar/J \sim 40$ps whereas the measured spin relaxation shows a two component decay[21] with overall decay time >10ns, again indicating a weak exchange. We shall see that in type I GaAs/AlGaAs quantum wells the spin relaxation mechanism is in the strong exchange regime.

The lack of level crossing signals in the magneto-polarisation spectra of the InGaAs/GaAs wells in chapter 4 and the theoretical predictions by S.R.Andrews[22] for the magnitude of the exchange enhancement in these wells compared to bulk seem to indicate that the exchange interaction in these samples is weak. The theoretical predictions of the strength of the exchange enhancement in a stepped GaAs/AlGaAs QW nominally similar to that studied by Bar-Ad and Bar-Joseph[23] and the lack of any level crossing signals in quantum beat absorption measurements, once more seem to indicate that the strength of the exchange interaction between the electron and hole in this sample is also far weaker than that for the regular GaAs/AlGaAs and GaAs/AlAs QWs. These observation seem to indicate the spin relaxation mechanism is in the weak exchange regime in both cases.

In our measurements of spin relaxation we have attempted to confirm experimentally the picture of the spin-relaxation in excitons outlined above. In this chapter we describe measurements of spin relaxation in a single GaAs quantum well as a function of carrier concentration and of temperature. This shows a dramatic difference between spin relaxation times of free carriers and of excitons. In chapter 6 we describe measurements on n-modulation doped samples which give the first direct confirmation of the wavevector dependence of hole spin relaxation.

5.3 The Dependence of Polarisation on Carrier Concentration: Experimental Procedure and Results

The quantum well used in the measurements described in this chapter was the 57.5Å wide well of sample DB35 described fully in chapter 2. Application of a forward or reverse bias injects, to a varying degree, electrons or holes respectively. Figure 5.1 shows measurements of polarisation as a function of applied bias at 4.2K using the experimental set-up as shown in figure 5.2. As before, the excitation source was the Oxford University CR599 dye laser copy pumped with the Spectra Physics 171 Ar-ion laser but now, in comparison to the previous situations, excitation was by alternately left and right circularly polarised light produced by the PEM and only one circular polarisation of the luminescence was passed to the spectrometer to be monitored. The Stokes shifts in figure 5.1 were obtained from the wavelength position of the PL peak and the wavelength of dye laser for resonant excitation at the heavy-hole transition for an applied bias.

The Stokes shift is the energy difference between the absorption onset and the luminescence peak position in the sample. It consists of two components one due to sample imperfection which is present in the fully depleted well and an extra component due to the presence of a degenerate sea of carriers. The extra Stokes shift ΔE gives a direct measure

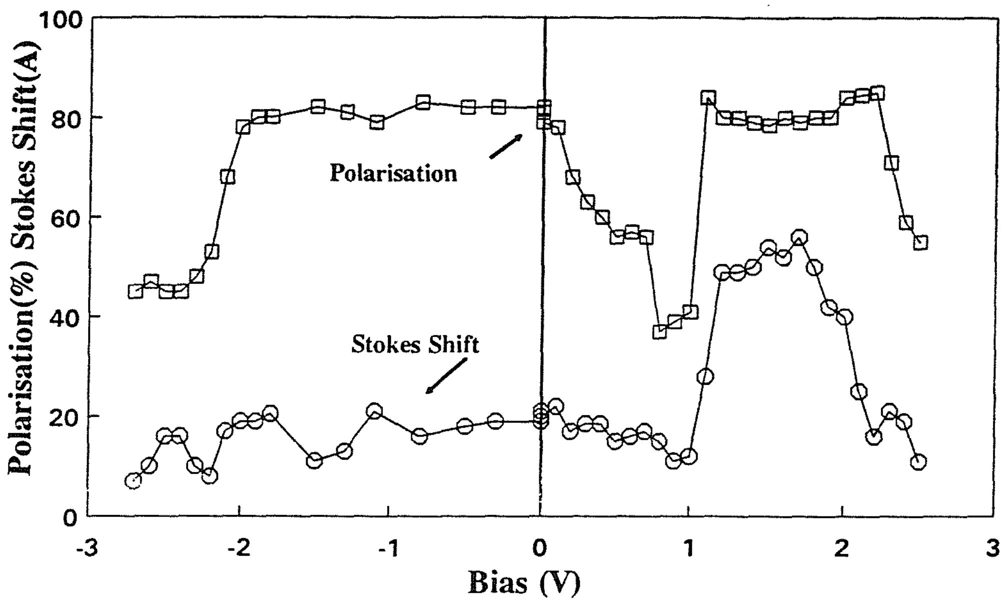

Figure 5.1 Polarisation and Stokes shift as a function of applied bias in the GaAs/AlGaAs sample DB35 at 4.2K

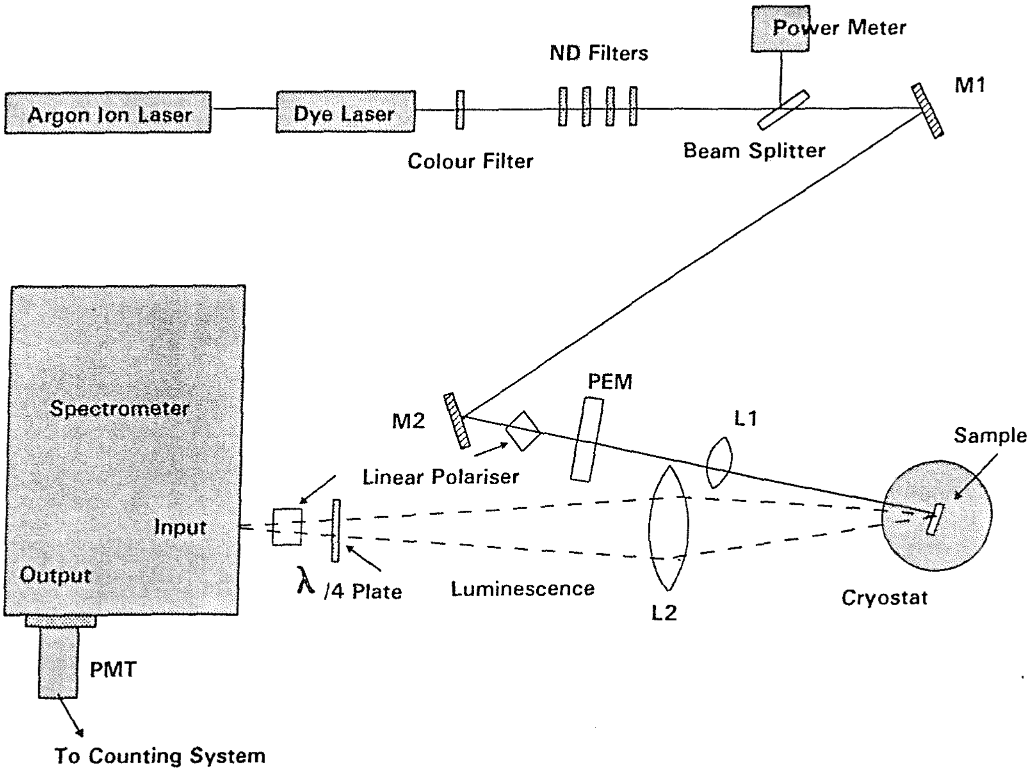

Figure 5.2 The experimental arrangement used for the polarisation measurements on DB35

of the carrier concentration ρ

$$\rho = \frac{\mu_{ex}}{\pi\hbar^2}\Delta E \qquad 5.4$$

where μ_{ex} is the reduced excitonic effective mass.

The minimum in Stokes shift in figure 5.1 at +0.9V occurs at the flat band region where the wells are totally depleted of carriers and gives a measure of the component due to imperfection. The polarisation is correspondingly low here. As soon though, as there is an appreciable carrier concentration, the polarisation rises sharply to a high value.

Figure 5.3 shows the polarisation as a function of the carrier concentration calculated using equation 5.4. The measurements were taken at both 1.8K and 4.2K. Also shown is the Fermi energy of the electron and hole populations and the binding energy of atomic excitons as a function of carrier concentration[24,25].

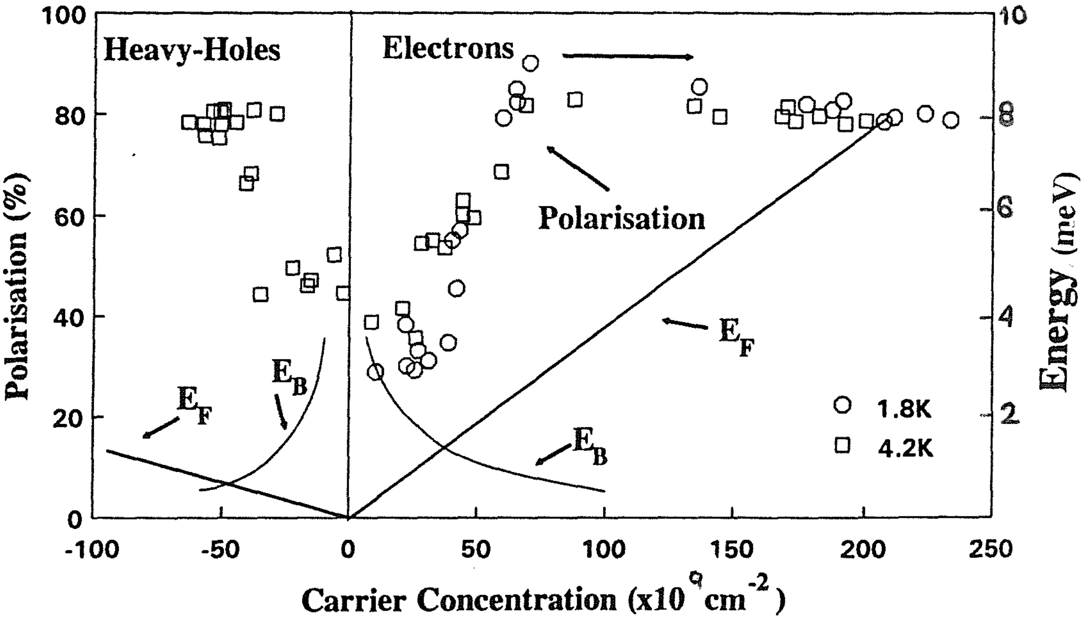

Figure 5.3 Polarisation as a function of carrier concentration in the 57.5Å well of sample DB35. The lines indicate Fermi energy E_F and exciton binding energy E_B from references 24 and 25.

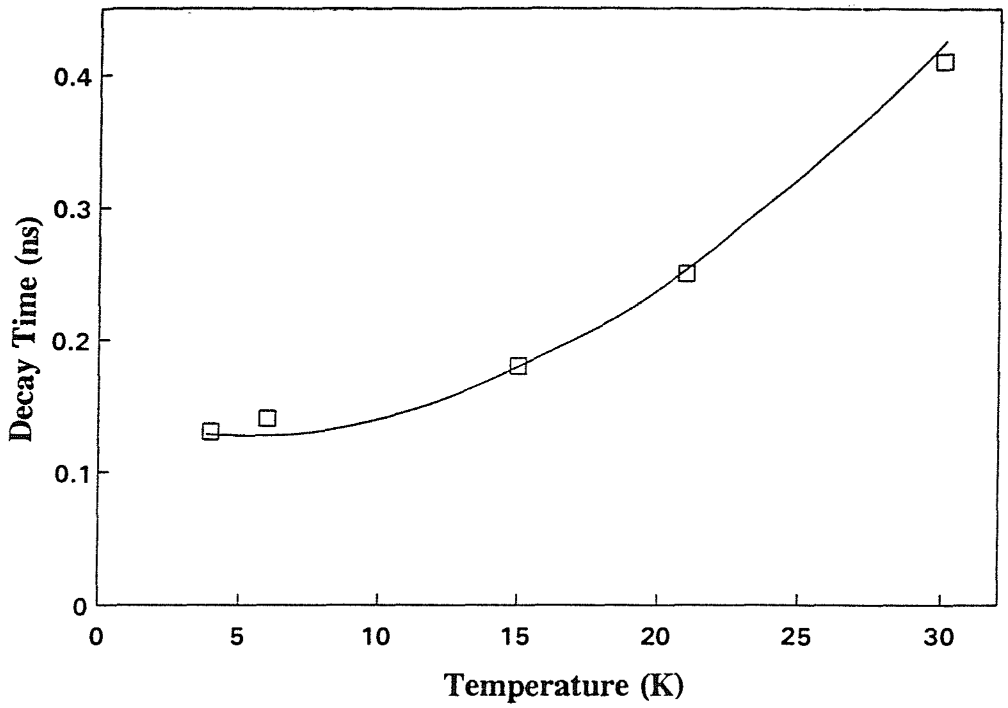

Figure 5.4 Luminescence decay time at flat band with increasing temperature.

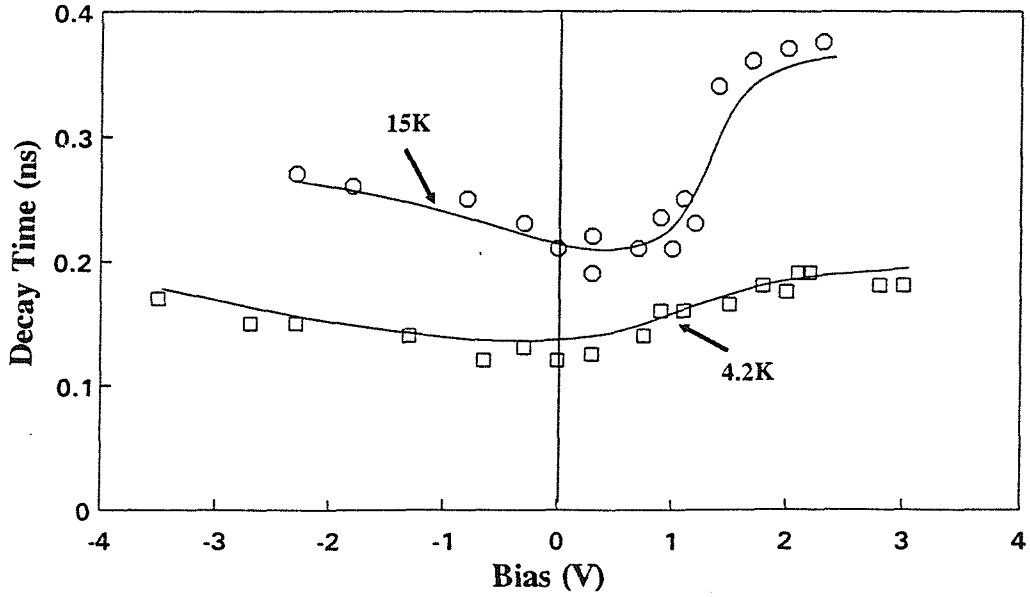

Figure 5.5 Luminescence decay time as a function of bias at 4.2K and 15K.

5.4 Spin Relaxation Time as a Function of Carrier Concentration.

The luminescence polarisation is given by

$$P = \frac{\tau_s}{\tau_s+\tau_r} \qquad 5.5$$

where τ_s is the spin relaxation time and τ_r is the luminescence decay time. In order to extract values of τ_s, measurements of τ_r for this sample were made by Eccleston et al[26] using picosecond excitation and Streak Camera detection. Values as a function of bias and of temperature are shown in figures 5.4 and 5.5.

We have interpolated between the curves in figure 5.4 and 5.5 in order to obtain values of τ_r to provide estimates of τ_s from our measurements of P. Figure 5.6 shows the spin relaxation time as a function of carrier concentration obtained in this way.

5.4.1 Interpretation

On the basis of the introductory review we interpret the form of figure 5.6 as follows:- For concentrations above the sharp increase in the spin relaxation time, the binding energy E_B is less than the Fermi energy E_F, so recombination involves approximately free minority carriers with a sea of majority carriers. The long relaxation times we measure apply to the minority carriers. For concentrations below this increase the binding energy exceeds the Fermi energy and so recombination is of excitons. The fact that the spin relaxation here is lower than for the free minority carriers indicates that we must be in the strong exchange regime with $\tau_s^{ex} \sim \tau_s^h$ and τ_s^h determined by the superposition of a range of *k* states. As the binding energy decreases and the atomic excitons unbind to form loosely bound Mahan excitons and ultimately free carriers the spin relaxation time increases to a higher value.

For a 57.5Å wide quantum well the data of chapter 4 gives $\hbar/J=10$ps which is much less than the measured value of $\tau_s^{ex}=100$ps as required for the strong exchange regime.

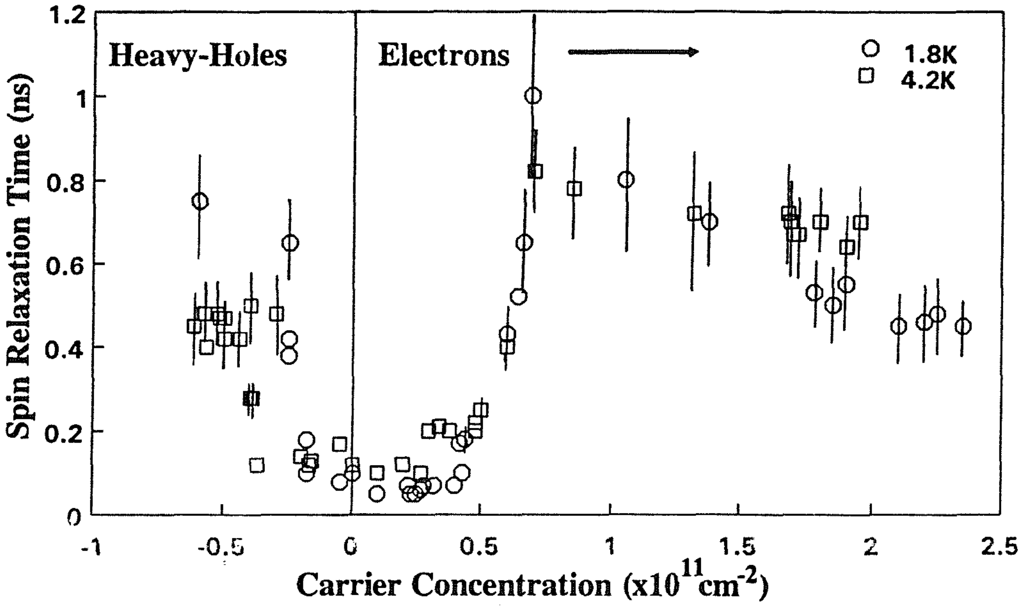

Figure 5.6 The spin relaxation time as a function of carrier concentration in the 57.5Å well of sample DB35.

5.5 Temperature Dependence of Polarisation: Experimental Procedure and Results

From figure 5.1, we have chosen three different biases at which to determine the polarisation temperature dependence. They are as follows:

1: a reverse bias of -0.8V for which there is a degenerate hole population in the well,

2: a forward bias of 2V when a degenerate electron population is present,

3: a forward bias of 0.9V when the small number of carriers in the well allows the formation of atomic excitons.

For each of the three biases given above, the procedure described in section 5.3 was repeated to obtain values of polarisation but this time for a variation in temperature instead of bias. Figure 5.7 shows the results. The experimental set-up was again that shown in figure 5.3 using the continuous flow cryostat for the measurements at 4.2K and above. We can see the initial polarisation for both electrons and heavy-holes is high, almost double the value for atomic excitons, and virtually identical up to temperatures of $\leq$4.2K. As the temperature increases further, all three carrier types show a drop in the magnitude of the polarisation the most significant drop being observed for recombination

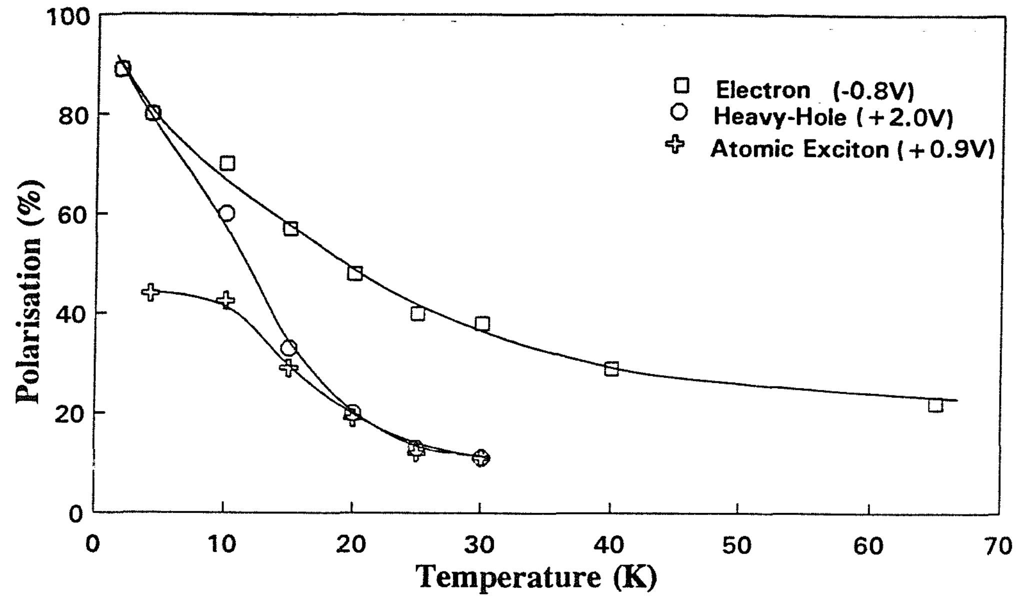

Figure 5.7 Temperature dependence of the luminescent polarisation for exciton, heavy-hole and electron recombination.

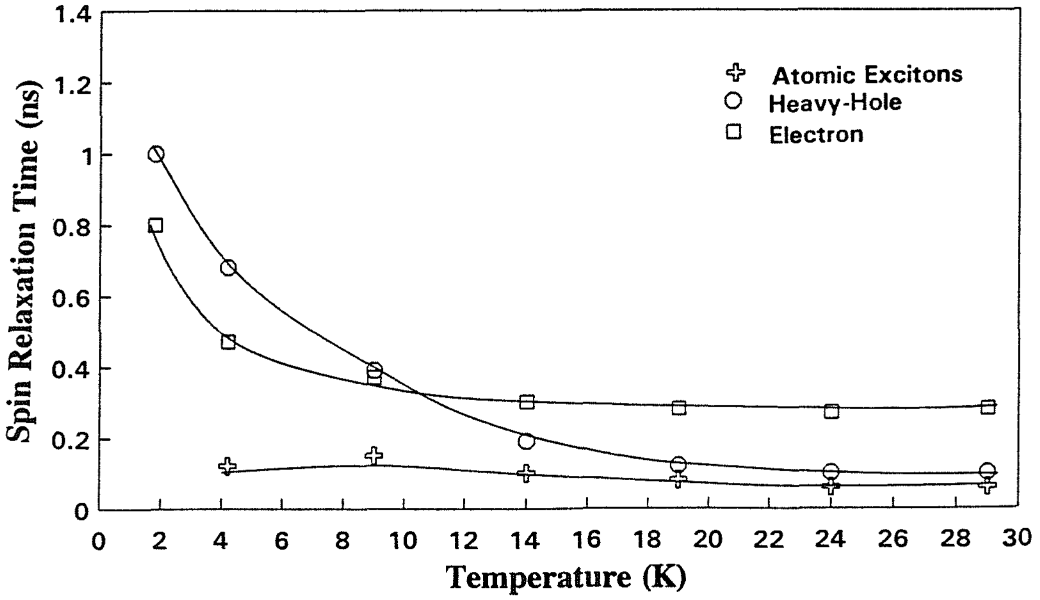

Figure 5.8 Estimated spin relaxation time of excitons, heavy-holes and electrons as a function of temperature.

governed by the minority photoexcited heavy-hole relaxation. We can see for temperatures in excess of 20K the polarisation for the heavy-hole extrapolates to the value of polarisation for atomic exciton recombination.

Using equation 5.5 and the interpolated values of τ_r obtained from figures 5.4 and 5.5 we obtain the trend of the spin relaxation as a function of temperature for excitons, heavy-holes and electrons shown in figure 5.8. There are considerable uncertainties in these estimates because of the interpolation of τ_r. We can see that the atomic exciton relaxation time is approximately constant at 100ps for the entire range of temperatures. For the electron and heavy-hole though, the separate relaxation times are both much longer ($\approx$1ns) at low temperatures and both show quite marked temperature dependence. The heavy-hole relaxation time although slightly longer than that of the electrons at temperature $\leq$10K, shows the greatest variation in relaxation time with temperature and drops to less than half the steady state value reached by that of the electron at the high temperatures. The heavy-hole spin relaxation time clearly extrapolates to that observed for the atomic exciton within the range of temperatures we have studied while that for the electron reaches a much higher steady state value.

We may give the following qualitative interpretation of the temperature dependence of relaxation times shown in figure 5.8. As the temperature is increased and the particles acquire thermal energy they will sample an increasing region of wavevector space. Their relaxation times will therefore reflect the wavevector dependence of the relaxation rate. The variation for the exciton is already a superposition of a range of *k*-values. The relaxation time for the holes falls rapidly with T approaching that for the exciton. This is consistent with the expectations that the hole spin relaxation is in the strong exchange regime. The temperature at which excitonic and hole spin relaxation times become equal represents the point at which the thermal and excitonic wavevector spreads become equal. At a similar temperature the electronic spin relaxation time has not been reduced so significantly, consistent with a much less strongly wavevector dependent rate.

5.6 Conclusions

From all the above we can conclude that the hole is the faster relaxing particle when bound in an atomic exciton and that the hole relaxation time is distinctly wavevector dependent. The similarity of the hole and exciton spin relaxation time as a function of wavevector seem to indicate that the hole governs the exciton spin relaxation dynamics. This is to be expected from the limits of the strength of the exchange interaction detailed in the introduction which indicates the exchange interaction in type I GaAs/AlGaAs quantum wells is in the strong exchange regime and so the atomic exciton spin relaxation time would be governed by the faster relaxing particle. Our experimental results seem to indicate that it is the hole that controls the spin relaxation and recombination phenomenon as a whole in the atomic exciton.

5.7 References

1 Optical Orientation of Carriers in Interband Transitions in Semiconductors	A.I.Ekimov, V.I.Safarov	ZhETF Pis.Red. 12(1970)293
2 Spin Relaxation of Photoelectrons in p-type Gallium Arsenide	G.Fishman, G.Lampel	Phys.Rev.B 16(1977)820
3 Spin Relaxation of Conduction Electrons in $Al_xGa_{1-x}As$	A.H.Clark, R.D Burnham, D.J.Chadi, R.M.White	Phys.Rev.B 12(1975)5758
4 Subpicosecond Spin Relaxation Dynamics of Excitons and Free Carriers in GaAs Quantum Wells	T.C.Damen, L.Vina, J.E.Cunningham, J.Shah	Phys.Rev.Lett. 67(1991)3432
5 Luminescence Studies of Optically Pumped Quantum Wells in GaAs/$Al_xGa_{1-x}As$ Multilayers in Quantum Wells	R.C.Miller, D.A.Kleinmann, W.A.Nordland, A.C.Gossard	Phys.Rev.B. 22(1980)863
6 Optical Orientation in Quantum Wells	M.J.Snelling	Thesis Southampton University (1991)
7 Semiconductors and Semimetals	E.O.Kane	vol.1. Academic Press, NY (1987)
8 Spin Orientation of Electrons Associated with the Interband Absorption of Light in Semiconductors	M.I.D'yakonov, V.I.Perel	Sov.Phys.-JETP 33(1971)1053
9 Spin-Flip Scattering Times in Semiconductor Quantum Wells	G.Bastard, R.Ferreira	To appear in Surface Science
10 Spin Relaxation of Electrons due to Scattering by Holes	G.L.Bir, A.G.Aronov, G.E.Pikus	Sov.Phys.-JETP,42(1976)705

11 Optical Orientation of Holes in GaAs	A.N.Titkov, V.I.Safarov, G.Lampel	Proceedings of the 14th International Conference on the Physics of Semiconductors, Edinburgh, 103 (1979)
12 Hole Relaxation and Luminescence Polarisation in Doped and Undoped Quantum Wells	T.Uennoyama, L.J.Sham	Phys.Rev.Lett. 64(1990)3070
13 Variational Calculation of Polarisation of Quantum Well Photoluminescence	A.Twardowski, C.Hermann	Phys.Rev.B. 35(1987)8144
14 Infrared and Polarisation Anomalies in the Optical Spectra of Modulation Doped Semiconductor Quantum-Well Structures	A.E.Ruckenstein, S.Schmitt-Rink, R.C.Miller	Phys.Rev.Lett. 56(1986)504
15 Theory of spin orientation in "Optical Orientation"	M.I.D'yakonov, V.I.Perel	Elsevier Science Publishers (1984)
16 Fine Structure of Excitons in Type-II GaAs/AlAs Quantum Wells	H.W.van Kesteren, E.C.Cosman, W.A.J.A.van der Poel, C.T.Foxon	Phys.Rev.B 41(1990)5283
17 Optically Detected Magnetic Resonance Study of a Type II GaAs/AlAs Multiple Quantum Well	H.W.van Kesteren, E.C.Cosman, F.J.A.M.Gredanus, P.Dawson, K.J.Moore, C.T.Foxon	Phys.Rev.Lett. 61(1988)129
18 Optically Detected Magnetic Resonance of Excitons and Shallow Donors in $(GaAs)/_5(AlAs)_5$ Superlattices	J.M.Trombetta, T.A.Kennedy	Pre-print
19 Fine Structure of Heavy-Hole Excitons in GaAs/AlAs Superlattices	C.Gourdon, P.Lavallard	Phys.Rev.B 46(19992)4644
20 Quantum Beats in the Exciton Emission of Type-II GaAs/AlAs Quantum Wells	W.A.J.A van der Poel, A.L.G.J. Severens, C.T.Foxon	Pre-print
21 Spin Relaxation in Type I and Type II GaAs/AlGaAs Quantum Wells	W.A.J.A. van der Poel, A.L.G.J.Severens, H.W.van Kesteren, C.T.Foxon	Superlattices and Microstructures 5(1989)115
22 Private Communication	S.R.Andrews	1992
23 Exciton Spin Dynamics in GaAs Heterostructures	S.Bar-Ad, I.Bar-Joseph	Phys.Rev.Lett 68(1992)349

24 Theory of excitons in Semiconductors Quantum Wells Containing Degenerate Electrons or Holes	D.A.Kleinman	Phys.Rev.B 32(1985)3756
25 Observation of Decoupled Heavy and Light Holes an GaAs/$Ga_{1-x}As_xAs$ Quantum Wells	A.S.Plaut, J.Singleton, R.J.Nicholas, R.T.Harley, S.R.Andrews, C.T.B.Foxon	Phys.Rev.B 38(1988)1323
26 Time Resolved Photoluminescence Studies of GaAs/AlGaAs Quantum Well Structures	R.Eccleston	Thesis Imperial College (1989)

6 Wavevector Dependence of the Hole Spin-Lattice Relaxation Time

6.1 Summary

This chapter outlines some of the initial findings of cw photoluminescence studies of the spin-lattice relaxation time of holes in n-doped type I GaAs/$Al_{0.33}Ga_{0.67}As$ quantum wells. We have observed a decreasing spin-lattice relaxation time with increasing well width. Quite the opposite is observed for excitons in pure undoped type I GaAs/$Al_{0.36}Ga_{0.64}As$ QWs where instead the spin lattice relaxation time increases with well width[1,2]. The different behaviour of the free hole from the exciton may be qualitatively explained as a consequence of the k-space dependence of the hole spin relaxation time directly confirming theoretical predictions.

6.2 Introduction

Chapter 5 dealt with exciton spin-lattice relaxation phenomena in type I GaAs/$Al_{0.36}Ga_{0.64}As$ QW. We showed, given the values of exchange measured in chapter 4, that for type I wells was in the strong exchange regime, and therefore the more rapidly relaxing particle controlled the spin relaxation time of the exciton. From temperature dependent polarisation measurements we showed that when confined in an exciton, the hole, and not the electron, has the faster relaxation rate and so the hole governs the excitonic spin relaxation rate. The consideration of exchange not only explains the anomalously short relaxation times recorded for type I excitons in narrow wells (10ps to 100ps)[3-8] but also those in bulk GaAs or in the type II wells[6] (> 1ns) which are in the weak exchange limit. In these cases it appears that the slower relaxing particle governs the exciton relaxation.

Given that free holes and electrons have τ_s > 1ns in QWs at low temperature it is apparent there must be a strong wave vector dependence for the hole spin-lattice relaxation time. Sham et al[9] first predicted such a wave vector dependence based on the mixing of the light and heavy hole bands. In bulk GaAs the light and heavy hole bands are degenerate giving almost instantaneous spin relaxation (4ps)[10], but in a quantum well, the bands are decoupled at $k=0$ giving long relaxation times. Away from $k=0$ there is an increasing admixture of the valence bands and the spin relaxation is much more rapid. Bastard et al[11] have carried out numerical calculations of the wavevector dependence, confirming the work of Sham et al[9]. The significance of this in the case of the exciton is that the particle wavefunctions is made up of a superposition of plane-wave states spanning a range of wavevectors $\approx 1/2a_0$ where a_0 is the exciton radius. In wells narrower than 200Å this range is roughly equivalent to $1/L_z$ where L_z is the well width. The spin relaxation time of the hole within an exciton is therefore expected to be much shorter than for a free hole.

The well width dependence of the excitonic spin-lattice relaxation time was studied by co-workers[1,2] from a combination of polarisation measurements across the luminescence line and time resolved luminescence decay time measurements[12]. The variation in the spin-lattice relaxation time across the luminescence line was also calculated. The results showed the relaxation time was a minimum around the high energy half intensity point of the PL and increased to both the low and high energy side of this. An average of the spin relaxation time in the extended states (between the PL peak and the high energy half intensity point) for each well width studied showed a linear increase in spin relaxation time with well width. Under the qualitative model of exciton relaxation dominated by hole relaxation in a strong exchange regime, this behaviour must represent the net effect of variations of hole confinement and wavevector dependence with well width on the hole spin relaxation.

In this chapter we describe similar measurements for free holes in a degenerate electron Fermi sea for a three well widths. The variation of relaxation time with energy and well width is very different from the excitonic case and gives a direct measure of the wavevector dependence of the hole spin relaxation time.

6.3 Experiment

The aim of the experiment was to excite at the heavy-hole absorption peak with circularly polarised light (σ^+) and measure the depolarisation of the luminescence across the PL linewidth. From the trend of the polarisation we could extrapolate energetically back to the excitation energy and obtain the polarisation at the instant of excitation. It was crucial though, to ensure that only pure luminescent polarisation was measured and this turned out to be the major experimental difficulty.

6.3.1 Experimental Procedure

The experimental set-up was that shown in figure 6.1 and spectra were measured for the three modulation doped n-type samples NU590, NU535 and NU211 described in chapter 2. The excitation source was the Coherent CR599 dye laser copy, with Pyridine 2 dye as the lasing medium, pumped by the Spectra Physics Ar^+ ion laser. The linear polariser followed by the quarter wave plate ensured excitation was of circularly polarised light and the detection was of the intensity and the circular polarisation of the emission. The sample temperature was 1.8K.

For each well in turn, pumping at the heavy-hole, the spectrometer was scanned over a sufficiently large energy range to take in not only the luminescence peak but also the sharp peak from the elastically scattered laser light on the high energy side of the PL peak. For each position of the spectrometer the counts were averaged over 100sec to ensure a reasonable signal to noise.

Figures 6.2, 6.3 and 6.4 show the luminescence and luminescence excitation spectra of the three samples. From the Stokes shift between the emission and excitation peaks we obtain electron concentrations, under the conditions of excitation as shown in **Table 1**

Sample	**Well Width (Å)**	**Electron Concentration**	**$P(E_F)$**	**$\tau_r(E_F)$ (ps)**	**$\tau_s(E_F)$ (ps)**
NU590	51Å	$2.7x10^{11}cm^{-2}$	0.5	240	240
NU535	68Å	$2.3x10^{11}cm^{-2}$	0.45	220	180
NU211	102Å	$3.3x10^{11}cm^{-2}$	0.07	280	21

The elastically scattered laser light was very highly polarised compared to the luminescence. This produced a very highly polarised background and so it was necessary to reduce this component as far as possible and to know accurately the magnitude of the laser polarisation and intensity to subtract as background. Steps were taken to optimise the contrast of the spectrometer by masking the output slits to remove stray reflections that existed as a result of the mirror inside the spectrometer. The correction was measured by

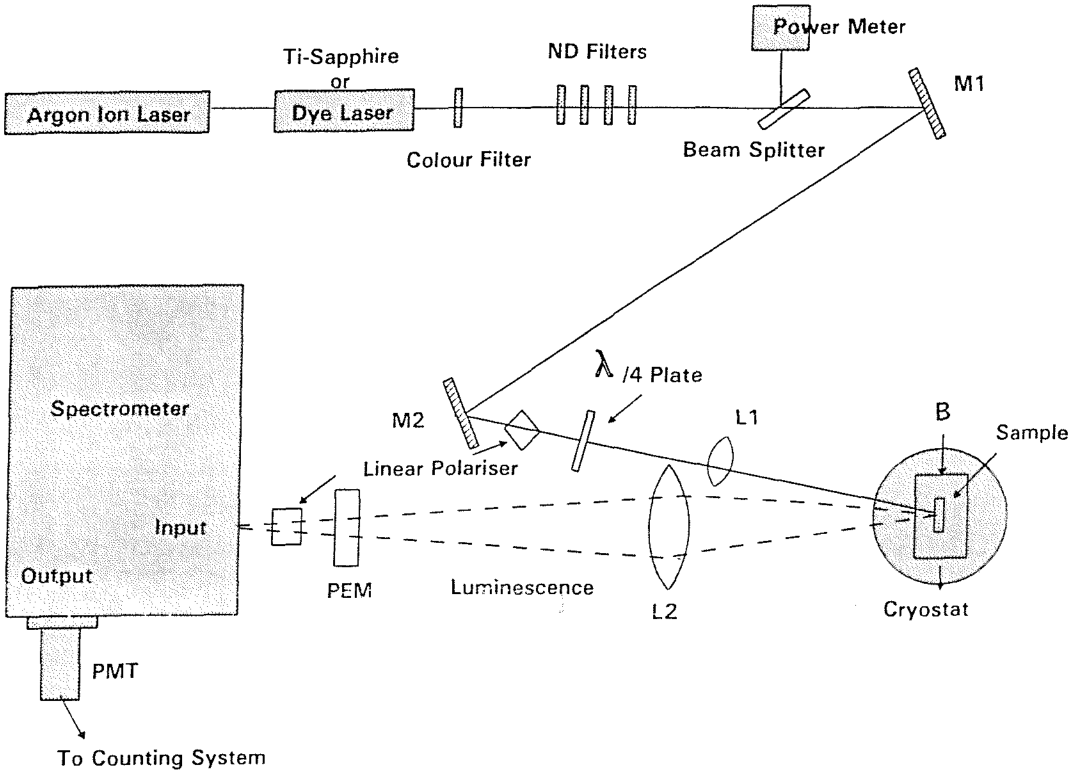

Figure 6.1 Experimental set-up for the spin-polarised luminescence measurements.

recording spectra consisting only of the elastically scattered laser light obtained for excitation with the laser tuned into the band gap. The polarisation spectra could then be corrected for this background laser light using the average value of polarisation from these spectra.

The lifetime measurements were made by Dr.P.Dawson at UMIST using a mode-locked argon laser for excitation and correlated photon counting detection[12]. These measurements were made at a number of energies across the luminescence linewidth and are shown in figures 6.2b, 6.3b and 6.4b.

6.3.2 Results

The solid lines in figures 6.2a, 6.3a and 6.4a are the PL spectra for the three NU GaAs/AlGaAs samples. The solid squares are the values of polarisation measured below the excitation energy. The large peak in the luminescence to the high energy side is the elastically scattered laser light at this excitation energy. We can see that the polarisation is virtually constant well below the excitation energy in all three cases but rises sharply in the laser wings. This increase is especially noticeable in the case of NU211 which exhibits a very large and sudden increase in polarisation despite a small and nearly

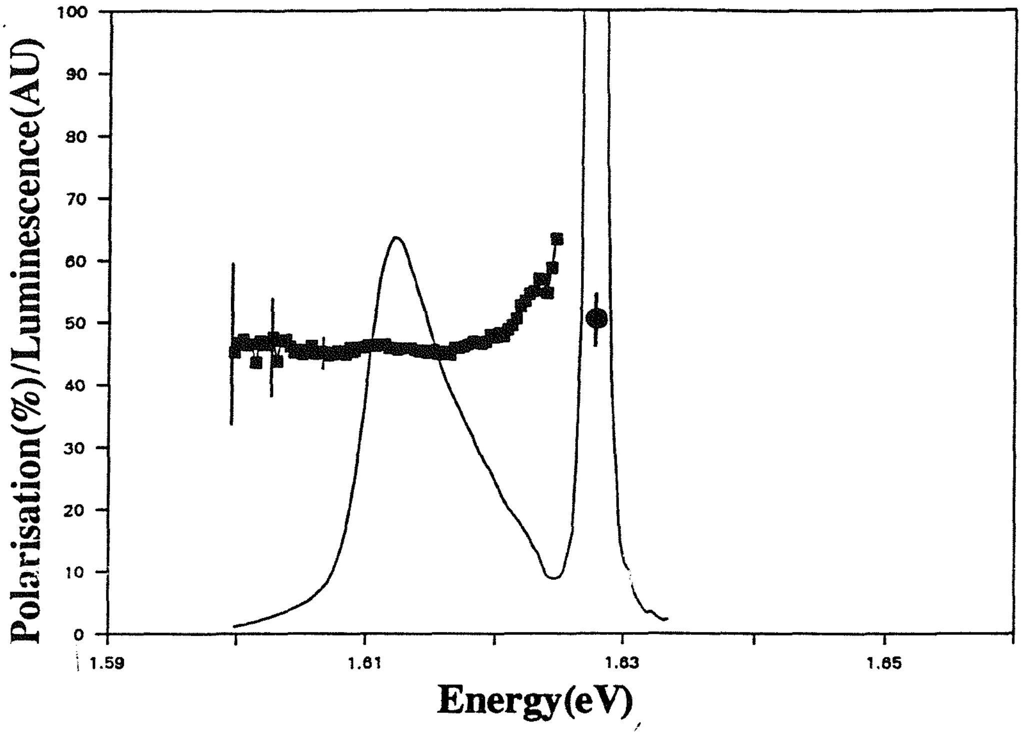

Figure 6.2a Luminescence and the measured luminescence polarisation for NU590, the 51Å GaAs/AlGaAs sample.

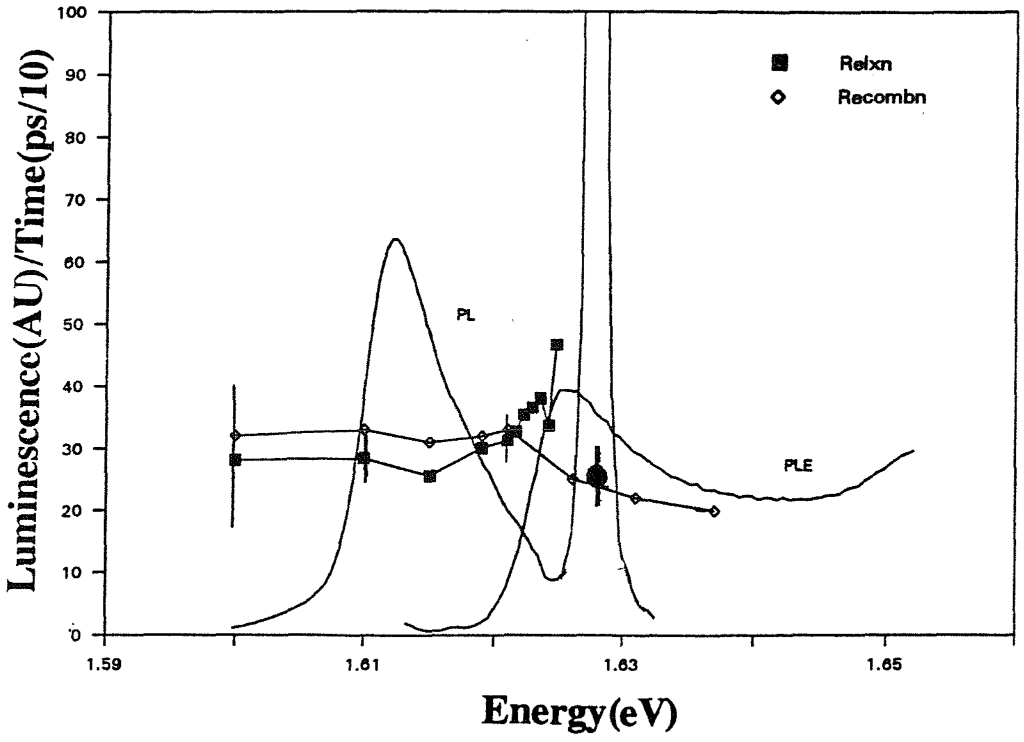

Figure 6.2b Recombination time (after P.Dawson[12]) and the calculated spin-lattice relaxation time for NU590 the 51Å GaAs/AlGaAs sample.

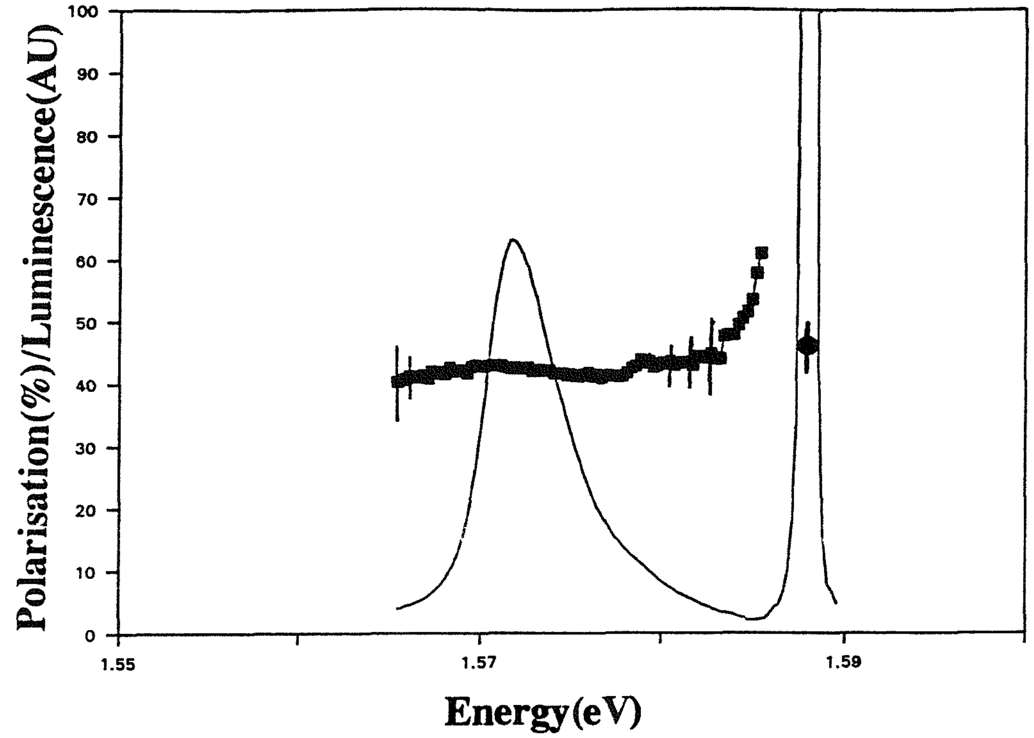

Figure 6.3a Luminescence and measured luminescence polarisation for NU535, the 68Å well.

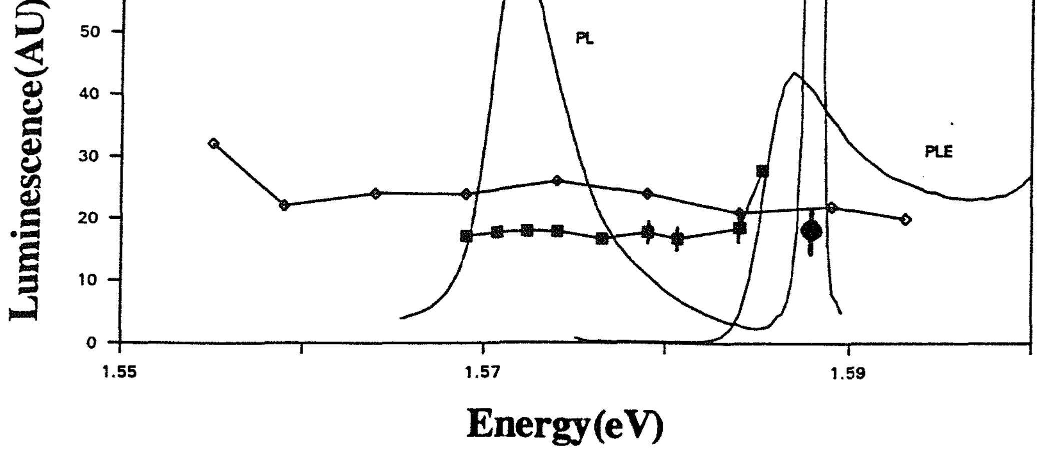

Figure 6.3b Recombination time and calculated spin-lattice relaxation time for NU535.

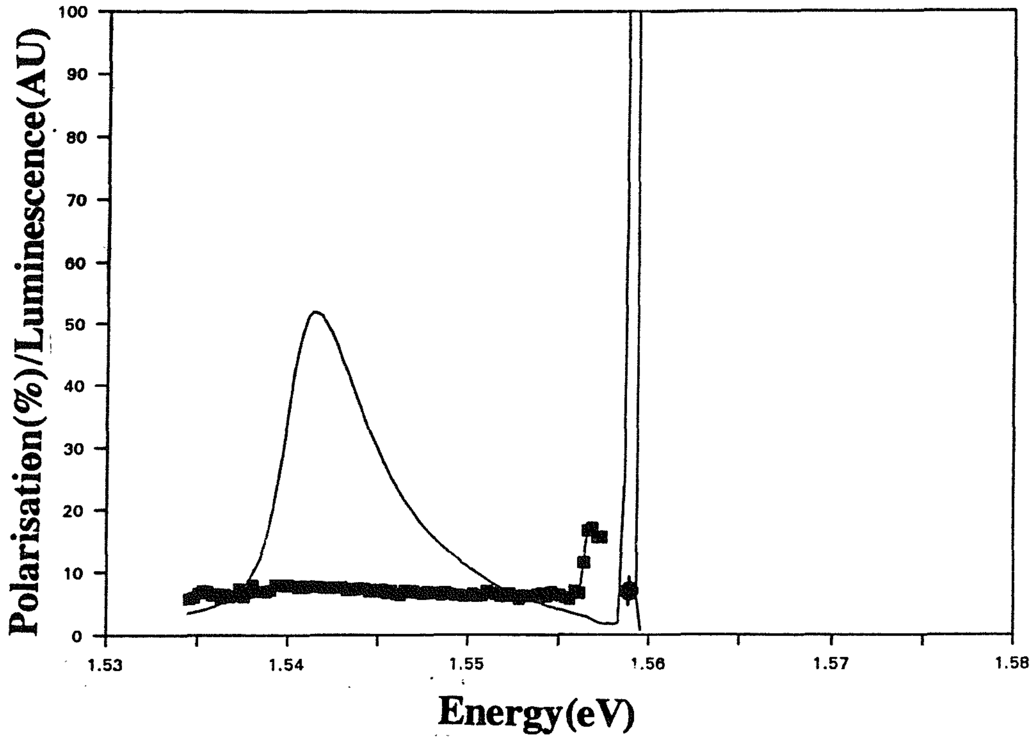

Figure 6.4a Luminescence and luminescent polarisation for NU211 the 102Å GaAs/AlGaAs sample.

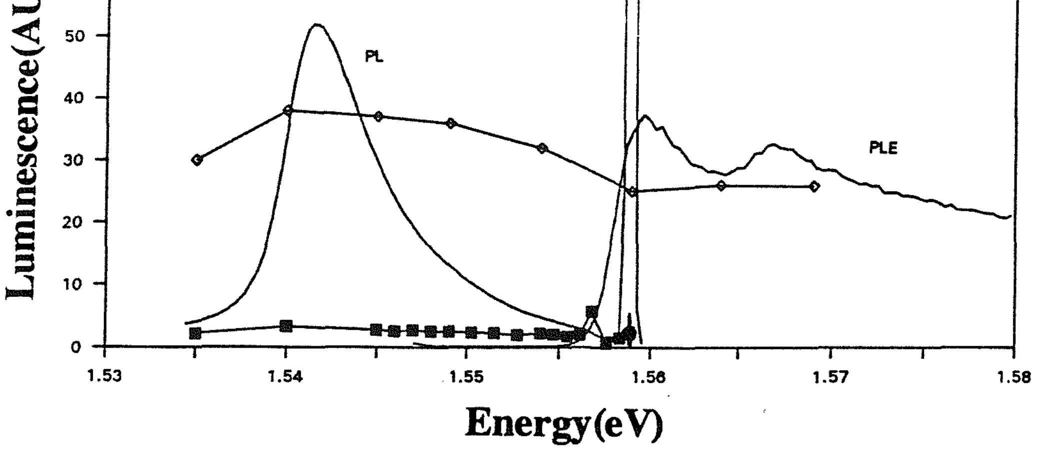

Figure 6.4b Recombination and relaxation times for NU211.

constant polarisation across the largest portion of the luminescence linewidth. One important factor in the extrapolation is the extent to which the polarisation in the wings is affected by the background laser polarisation. Although corrections have been made to the polarisation spectra to take into account the laser background, we cannot be sure that the rapid increase in polarisation in the wing of the laser is not at least partly due to inadequacy of the correction where the elastic intensity is comparable to the luminescence. This would lead to an exaggerated value for the extrapolated polarisation. To obtain the polarisation at the excitation energy we have therefore extrapolated the polarisation back to the excitation energy using the trend across the largest portion of the luminescence linewidth and discounted the increase in polarisation in the laser wings, the solid circle in each graph at the excitation energy denotes the extrapolated polarisation value. The size of the error in the wings is an indication only of the higher statistical error associated with the reduction in luminescent intensity. The error at the excitation energy consists mainly of the error involved in the extrapolation.

Figures 6.2b, 6.3b and 6.4b show the recombination times (diamonds) measured over the luminescence linewidth together with the luminescence peak and the Stokes shifted HH (and sometimes LH) absorption peaks. Using the relation

$$P = \frac{\tau_s}{\tau_r + \tau_s} \qquad 6.1$$

where P is the extrapolated polarisation at the excitation energy, τ_s is the spin-lattice relaxation time of a particle at that energy and τ_r is the lifetime of the particle again at that energy, we can calculate the spin-lattice relaxation time of the hole at the excitation energy as given in table 1, pg. 103.

In figure 6.2b-6.4b we have used this formula also to calculate the spin relaxation across the PL line. This is not strictly valid because equation 6.1 assumes that the initial polarisation of the carriers at a particular energy is unity whereas at energies below the excitation energy the carriers must be less than fully polarised after thermalisation from the higher energy. However since the observed polarisation and the luminescence lifetime are effectively independent of energy, it seems reasonable to assume that this gives a reliable indication of the spin-relaxation time at lower energies.

The recombination times must be regarded at this stage as a first estimate to the behaviour of the photoexcited carriers at low density in these wells, as a comparison of our PL lineshapes with those of P.Dawson[12] under his experimental conditions show them to be quite different. We have measured asymmetrical PL lineshapes whereas those of reference 12 are symmetrical in shape. The resolution used for the lifetime measurements was much lower than in our case, but even so, the lack of asymmetry seems to indicate a significant difference. As detailed previously in chapter 2, these GaAs/AlGaAs samples were modulation doped but nonetheless the carrier concentration is somewhat dependent on the illumination intensity on the sample. The excitation conditions under which our polarisation measurements were obtained and those for which the recombination times were obtained were different and so, given the lineshape difference, we could be dealing with different concentrations of injected carriers in the two cases.

6.3.3 Analysis

In the case of *n*-doped quantum wells, due to the presence of the 2D electron gas, assuming that the optical processes conserve wavevector the minimum in-plane wave vector at which holes can be photocreated is $k_{\parallel}=k_F$ where k_F is the Fermi wave vector. Exciting at the e_1h_1 transition, as we have, heavy-holes are created at $k_{\parallel}=k_F$ without superimposed excitation of light holes.

Of greatest interest to us is the effect of the mixing of the valence bands on the hole relaxation time. In order to make comparisons between samples of different well width we need to take account of the different wavevector dependence of this mixing for different wells. We therefore need to calculate a normalised wavevector k_F/k_x where k_x is the wavevector at which the light and heavy-hole bands cross.

A simple effective mass calculation can be performed to give the value of k_F. Using the expression for the two dimensional density of states

$$\rho_{2D} = \frac{m^*}{\pi\hbar^2} \qquad 6.2$$

where m^* is the reduced mass and $\hbar$ is Plank's constant divided by 2π then if the Fermi energy is denoted by

$$E_F = \frac{\hbar^2 k^2_F}{2m^*} \qquad 6.3$$

then the Fermi wave vector k_F can be expressed as

$$k_F = \sqrt{2N_e\pi} \qquad 6.4$$

where N_e is the relevant carrier concentration. Given the electron concentrations shown in table 1, the Fermi wave vector can be calculated for each sample. Using the Luttinger effective mass approximation for the valence bands, the wavevector at which the light and heavy-hole bands cross is given approximately by

$$k_x \sim \sqrt{2}\left(\frac{\pi}{L_z}\right) \qquad 6.5$$

Figure 6.5 shows the hole relaxation time plotted against the reduced wavevector k_F/k_x. As expected there is a sharp fall off of relaxation time with wavevector. For both the 51Å and 68Å well (the first two points in the graph) the relaxation time are roughly similar but for the 102Å well the relaxation time has dropped quite significantly.

A possible criticism of the experimental method used here is that since the excitation occurs at a finite wavevector, the initial spin polarisation of the photoexcited holes will be less than unity, due to the valence band admixture. However calculations by Rhoussignol et al[13] and in a similar vain by Twardowski et al[14] of this effect show that the reduction of initial polarisation is only of the order of 10% for the wavevector range used here. Since we measure polarisations at recombination of the order of 50% or less it is clear that the major contribution to depolarisation is from spin-relaxation after excitation. We are therefore justified, given other uncertainties in the measurements, in neglecting this effect.

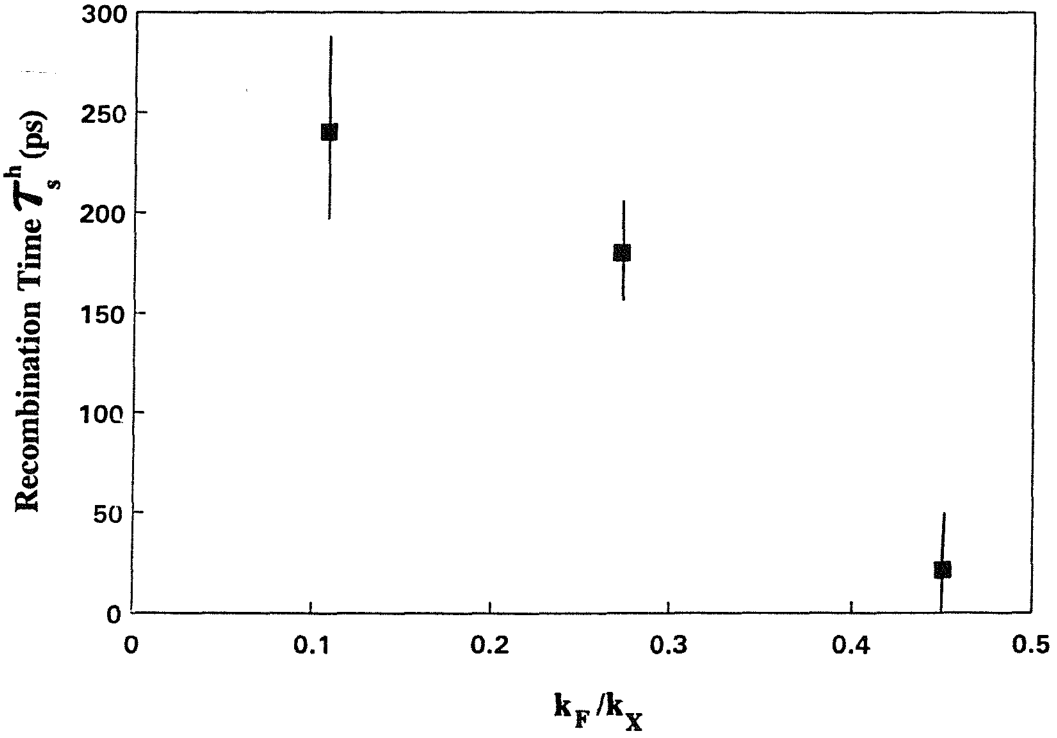

Figure 6.5 The hole spin relaxation time as a function of the position of the Fermi wavevector from the wavevector of the valence band cross-over.

6.4 Conclusions

We have successfully measured the spin-lattice relaxation times of free holes in n-doped type I quantum wells and revealed a well width dependence of the relaxation time. This gives a direct measurement of the wave vector dependence of the hole spin relaxation time and confirms the theoretical predictions.

The constancy of both τ_s and τ_r across the PL linewidth is unexpected. We would have expected to see both these quantities decrease in magnitude across the linewidth. The fact that they are observed to be constant, does not affect the values of polarisation at the excitation energy that were obtained from the extrapolation of P nor the values of $\tau_s(E_F)$ in table 1. as the trend towards the high energy side of the luminescence line inherently determines the extrapolation of P. Nonetheless the constancy of these quantities appears to indicate that the thermalisation and recombination processes for holes are not fully understood.

6.5 References

1 Optical Orientation in Quantum Wells	Michael Snelling	Thesis Southampton University (1991)
2 Spin-lattice Relaxation and Exchange Interaction of Excitons in Type I GaAs/AlGaAs Quantum Wells	M.J.Snelling, E.Blackwood, R.T.Harley, P.Dawson, C.T.B.Foxon	Submitted to Phys.Rev.Lett.
3 Spin Relaxation in Optically Excited Quantum Wells	M.J.Snelling, A.S.Plaut, G.P.Flinn, A.C.Tropper, R.T.Harley, T.M.Kerr	J.of Lumin. 45(1990)208
4 Exciton Spin Dynamics in GaAs Heterostructures	S.Bar-Ad, I.Bar-Joseph	Phys.Rev.Lett. 68(1992)349
5 Subpicosecond Spin Relaxation Dynamics of Excitons and Free Carriers in GaAs Quantum Wells	T.C.Damen, L.Vina, J.E.Cunningham, J.Shah	Phys.Rev.Lett 67(1991)3432
6 Spin Relaxation in Type I and Type II GaAS/AlGaAs Quantum Wells	W.A.J.A.van der Poel, A.L.G.J.Severens, H.W.van Kesteren, C.T.Foxon	Superlattices and Microstructures 5(1989)115
7 Direct Observation of Picosecond Spin Relaxation of Excitons in GaAs/AlGaAs Quantum Wells using Spin-dependent Optical Nonlinearity	A.Tackeuchi, S.Muto, T.Inata, T.Fijii	Appl.Phys.Lett 56(1990)2213

8 Spin Relaxation and Thermalization of Excitons in GaAs Quantum Wells	T.C.Damen, K.L.Jagdeep, J.E.Cunningham	Appl.Phys.Lett.58(1991)1902
9 Hole Relaxation and Luminescence Polarisation in Doped and Undoped Quantum Wells	T.Uennoyama, L.J.Sham	Phys.Rev.Letts.64(1990)3070
10 Optical Orientation of holes in GaAs	A.N.Titkov, V.I.Safarov, G.Lampel	Proc.14th Int.Conf. on Physics of Se/c,Ser.no.43, ed.B.L.H.Wilson, 1978
11 Spin-Flip Scattering Times in Semiconductor Quantum Wells	G.Bastard, R.Ferreira	To appear in Surface Science
12 Private Communication	P.Dawson	1992
13 Hole Polarization and Slow Hole-Spin Relaxation in an n-doped Quantum-well Structure	Ph.Roussignol, P.Rolland, R.Ferreia, C.Delalande, G.Bastard	Phys.Rev.B. 46(1992)7292
14 Variational Calculation of Polarization of Quantum-well Photoluminescence	A.Twardowski,C.Hermann	Phys.Rev.B. 35(1987)8144

7 Summary and Conclusions

The ability to preferentially spin-polarise a photoexcited carrier population in a quantum well by optical pumping methods[1] has enabled us to study the fine structure and some of the parameters governing the spin relaxation dynamics of excitons, heavy-holes and electrons in a quantum well.

In chapter 3, from the magnetic field dependence of the Zeeman splitting in both type I GaAs/$Al_{0.36}Ga_{0.64}As$ and $In_{0.11}Ga_{0.89}As$/GaAs quantum wells we measured the magnetic exciton g-factor as a function of well width. In GaAs/$Al_{0.36}Ga_{0.64}As$ we observed a change of sign for L_z between 73.4Å and 112Å, with the tendency of g_{ex}^* to a positive constant value for well widths greater than 250Å. From knowledge of the electron g-factor in type I GaAs/AlGaAs wells from Hanle measurements[2,3,4], together with the measured exciton g-factors in GaAs/AlGaAs we were able to estimate the magnitude of the heavy-hole g-factor in these GaAs/AlGaAs systems. The magnitude of the heavy-hole g-factor in these type I GaAs/AlGaAs wells was in good agreement with previously measured values of g^*_h[5,6].

For the $In_{0.11}Ga_{0.89}As$/GaAs wells, g^*_{ex} increased from small positive values in narrow wells up to well widths roughly 40Å in width, at which point, it exhibited a steady decrease in magnitude for increasing well widths. A theoretically predicted trend for the electron g-factor[7] that took into account the strain induced splitting, previously unaccounted for in 3-band *k.p* perturbation theory[8,9] used to calculate the effective mass and effective g-factor in quantum wells systems, was used, in conjunction with the measured exciton g-factors in these wells, to predict the well width dependence of the heavy-hole g-factor. The well width dependence of g^*_h is similar to that observed for g^*_{ex} in this system, exhibiting an increase in magnitude up to well widths in the region of 40Å and then decreasing in magnitude as the well width increases.

The magnetic g-factors are important parameters in the dynamical processes of the spin system of electrons, heavy-holes and excitons in a magnetic field. They govern many of the processes in quantum confined structures such as electron-nuclear spin coupling, magneto-optical polarisation effects and the Zeeman splitting of electrons, holes and excitons. All these properties are possible considerations in the design and operation of many "quantum effect" devices.

The excitonic magneto-polarisation spectra studied in Chapter 4 revealed the presence of exchange interactions between the exciton energy levels in both GaAs/$Al_{0.36}Ga_{0.64}As$ and GaAs/AlAs. We successfully measured the electron-hole exchange interaction in both systems as a function of well width, together with a zero field exchange splitting associated with the optically active exciton levels. The presence of this exchange splitting indicated a departure of the quantum well symmetry from the ideal D_{2d}. We suggested this may have been as a result of defects in the growth interface. The measured exchange interactions in the GaAs/AlAs quantum wells were larger than at an identical well width in GaAs/AlGaAs but the calculated value of J in both these quantum well systems gave good agreement with theoretical predictions of electron-hole overlap[10,11,12] and extrapolated towards the measured value for the exchange in bulk. The magnitude of these exchange interactions were significantly larger than the exchange interactions measured in type II GaAs quantum wells[5,6,13,15,16].

Luminescent polarisation measurements from the recombination of either electron, hole or atomic exciton populations were monitored as a function of temperature in a doped GaAs/$Al_{0.3}Ga_{0.7}As$ quantum well. This revealed that the spin-lattice relaxation time of minority electrons or holes in a quantum well were long ~ 1ns, at low temperatures (1.8K) but that both decreased with increasing temperature. The decrease in magnitude of the hole relaxation time (τ_s^h) was far more rapid than that for the electron relaxation time (τ_s^e) and approached the value of the exciton spin relaxation time (τ_s^{ex}) at temperatures of ~30K. The temperature dependence indicated that the hole spin relaxation time was wavevector dependent to a far greater extent. Our results confirm the predictions of Sham et al[17] of a hole spin relaxation time dependent on wave vector due to the increased mixing of the light and heavy-hole bands away from $k=0$ in a quantum well. We also measured an extremely short spin-lattice relaxation time for the exciton, ~100ps, in the same sample. The tendency of the hole relaxation time to that of the exciton at higher temperatures indicated that the exciton spin dynamics were governed by the strong exchange interaction between the electron and hole which coupled their spin systems and resulted in the hole, that possessed the shorter relaxation time, controlling the exciton spin relaxation. The anomalously short spin relaxation time measured for the exciton was therefore interpreted as a result of the exciton wave function consisting of a superposition of plane wave states over a region roughly equal to π/L_z for well widths less than 200Å. The hole relaxation time was governed by the mixing of the valence bands states away from $k=0$ which resulted in a greatly reduced hole, hence exciton spin relaxation time.

In the final chapter, we showed the reduction in the hole spin-lattice relaxation time with increasing well width in n-modulation doped GaAs/AlGaAs quantum wells of roughly equal electron content. We showed that this is a consequence of a wavevector dependence of the hole spin relaxation time and obtained a plot of relaxation time versus a reduced wavevector. This contrasted with the previously observed increase in relaxation time of excitons in GaAs/AlGaAs quantum wells[2,18] with increasing well width.

We were unsuccessful in measuring either the excitonic g-factor in GaAs/AlAs or the exchange interactions in the $In_{0.11}Ga_{0.89}As/GaAs$ quantum wells. It seems probable that these quantities may be obtained using other techniques such as quantum beat[19] absorption or non degenerate four wave mixing[20].

The measurements of the minority hole spin-lattice relaxation times in the type I GaAs/AlGaAs wells in chapter 6 are the first of many possible investigations into type I spin dynamics. The area of spin-lattice relaxation dynamics in these type I quantum wells is still far behind that of the type II system, simply as a result of the order of magnitude decrease in the relaxation times in these type I systems which renders many optical detection techniques inapplicable. An extensive study of hole spin dynamics in type I quantum wells is necessary before we can gain real insight into the full effect of valence band mixing on quantum well systems.

Of interest also, would be the measurements of chapter 6 but in p-doped samples to confirm that the electron spin relaxation time is not so strongly wavevector dependent as the hole relaxation time. Polarisation decay measurements in samples with identical well widths but with different carrier concentrations would give a direct measure of the wavevector dependence of the hole or electron relaxation time rather than the normalised wavevector dependence we have measured.

In development is a system to study sub-picosecond pump/probe spectroscopy in type I quantum wells. This technique offers the possibility to study the strong/weak exchange interaction and from this, measure the excitonic decay times. The aim is to also use this set-up to measure quantum beats.

7.1 References

1 Theory of spin orientation in "Optical Orientation"	M.I.D'yakonov, V.I.Perel	Modern Problems in Condensed Matter Sciences 8(1984)11 North Holland
2 Optical Orientation in Quantum Wells	M.J.Snelling	Thesis Southampton University 1991
3 Optical Pumping and Optically Detected Nuclear Resonance	G.P.Flinn	Thesis Southampton University 1991
4 The Electronic g-factor in GaAs/AlGaAs Quantum Wells	M.J.Snelling, G.P.Flinn, A.S.Plaut, R.T.Harley, A.C.Tropper, R.Eccleston, C.C.Philips	IQEC'90 Digest Paper QPD14-1(pg367)
5 Fine Structure of Excitons in Type II GaAs/AlAs Quantum Wells	H.W.van Kesteren, E.C.Cosman, F.J.A.M.Greidanus, P.Dawson, K.J.Moore, C.T.Foxon	Phys.Rev.B 41(1990)5283
6 Optically Detected Magnetic Resonance of Excitons and Shallow Donors in $(GaAs)_5/(AlAs)_5$ Superlattices	J.M.Trombetta, T.Kennedy, W.Tseg, D.Gammon	Pre-print
7 g-factor and Effective Mass Anisotropies in Pseudomorphic Strained Layers	G.Hendorfer, J.Schneider	Semicond.Sci.Technol. 6(1991)595
8 Infrared Cyclotron Resonance in InSb	E.D.Palik, G.S.Picus, S.Teitler, R.F.Wallis	Phys.Rev. 122(1961)475
9 Tunnelling Cyclotron Resonance and the Renormalized Effective Mass in Semiconductor Barriers	G.Brozak, E.A.de Andrada e Silva, L.J.Sham, F.Derosa, P.Micelli, S.A.Schwarz, J.P.Harbison, L.T.Florez, S.J.Allen,Jr.	Phys.Rev.Lett. 64(1990)471
10 Exchange Effects on Excitons in Quantum Wells	Y.Chen, B.Gil, P.Lefebvre, H.Mathieu	Phys.Rev.B 37(1988)6429
11 Private Communication	S.R.Andrews	1992
12 Private Communication	S.R.Andrews	1992
13 Optically Detected Magnetic Resonance Study of a Type II GaAs/AlAs Multiple Quantum Well	H.W.van Kesteren, E.C.Cosman, F.J.A.M.Greidanus, P.Dawson, K.J.Moore, C.T.Foxon	Phys.Rev.Lett. 61(1988)129
14 Order of the X-Conduction Band Valleys in Type II GaAs/AlAs Quantum Wells	H.W.van Kesteren, E.C.Cosman, P.Dawson, K.J.Moore, C.T.Foxon	Phys.Rev.B 39(1989)13426

15 Exchange Interaction in Type II Quantum Wells	B.R.Salmassi, G.E.W.Bauer	Phys.Rev.B 39(1989)1970
16 Quantum Beats in the Exciton Emission of Type-II GaAs/AlAs Quantum Wells	W.A.J.A.van der Poel, A.L.G.J.Severens,C.T.Foxon	Pre-print
17 Hole Relaxation and Luminescence Polarisation in Doped and Undoped Quantum Wells	T.Uennoyama, L.J.Sham	Phys.Rev.Lett. 64(1990)3070
18 Time-Resolved Spin-Polarisation Spectroscopy in GaAs/AlGaAs Quantum Wells	Ph.Roussignol, P.Rolland, R.Ferreira, C.Delande, G.Bastard, A.Vinattieri, L.Carraresi, M.Colocci, B.Etienne	To appear in Surface Science
19 Absorption Quantum Beats of Magnetoexcitons in GaAs Heterostructures	S.Bar-Ad, I.Bar-Joseph	Phys.Rev.Lett. 66 (1991)2491
20 Spin-Flip-Induced Hole Burning in GaAs Quantum Wells: Determination of the Exciton Zeeman Splitting	H.Wang, M.Jiang, R.Merlin, D.G.Steel	Phys.Rev.Lett. 69(1992)804

Publications

Exciton, Heavy-Hole and Electron g-factor in Type I GaAS/AlGaAs Quantum Wells, Phys.Rev.B (Rapid Communication) 45(1992)3922

Spin-lattice Relaxation and Exchange Interaction of Excitons in Type I GaAs/AlGaAS Quantum Wells, In Press.